Politecnico di Torino

Master's Degree Programme Energy and Nuclear Engineering

Master Thesis

Comparative analysis and validation of satellite databases for the planning of photovoltaic and wind power plants in Morocco

Supervisors:

Prof. Filippo Spertino
Prof. Alessandro Ciocia
Prof. Reda Rabeh

Candidate:

Leda Legrottaglie

March 2026

Academic Year 2025/2026

Ringrazio i professori Filippo Spertino, Alessandro Ciocia e Reda Rabeh per il supporto tecnico ed i preziosi consigli.

Dedico questa tesi alla mia amata famiglia.

Abstract

The current global energy transition imposes a rapid evolution towards sustainable supply sources, reducing dependence on fossil fuels and mitigating the effects of climate change. In this macroeconomic and geopolitical scenario, Morocco emerges as a strategic actor of crucial importance for the MENA (Middle East and North Africa) region. However, despite the abundance of natural resources, the full exploitation of this potential still faces structural barriers, such as limited grid infrastructure and an incentive framework that is still being consolidated.

Before proceeding to the experimental analysis, it is fundamental to consolidate the technical foundations upon which the study rests. To this end, Chapter 1 exposes the physical and aerodynamic principles governing photovoltaic and wind conversion, respectively. I-V characteristics, power curves, and dependencies on environmental variables such as irradiance, temperature and wind speed are discussed here, providing the necessary theoretical tools to interpret the energy production metrics discussed later in the treatise.

To fully understand the scenario in which this research is situated, Chapter 2 of this thesis analyses the Moroccan energy context in detail. This section provides a complete mapping of renewable resources and existing infrastructures, examining the historical evolution and future perspectives of national energy policies to highlight the existing gap between the enormous theoretical potential and the current state of plant design.

The primary objective of the thesis arises from the practical need to identify reliable data to bridge the infrastructure gap. The goal is to critically analyse the various meteorological databases available today to find a unique, accurate, and homogeneous source capable of supporting the integrated planning of both wind farms (WT) and photovoltaic plants (PV).

The methodology adopted to achieve this objective is detailed in Chapter 3, which describes the process of selection and comparison of satellite databases.

Through the implementation of specific codes in the MATLAB environment, raw datasets were processed to visualize graphical trends and, most importantly, in Chapter 4 are presented the error metrics such as MAE, RMSE and standard deviation, thereby evaluating the numerical consistency among different data sources for energy planning.

To validate the theoretical analyses in a real operational context, the work subsequently focuses on a specific practical application. Chapter 5 introduces the case study of the International University of Rabat (UIR), describing the technical specifications of the residential pilot PV generator and the battery storage system present on campus. In this phase, the methodology shifts to a direct comparison between real data acquired from the university weather station and satellite datasets, quantifying the actual deviation between remote estimation and ground production through statistical indicators such as MBE and the R^2 coefficient.

In conclusion, the work demonstrates that, although satellite planning tools have reached a high degree of maturity, integration with in-situ experimental validations remains indispensable for managing uncertainties due to climate variability, thus providing solid guidelines for the future development of renewables in Morocco.

Contents

List of Figures

List of Tables

Chapter 1

1 General aspects of PV and WT technologies

This Chapter outlines the energy conversion principles of photovoltaic and wind technologies, respectively in Section 1.1 and Section 1.2.

The explanations focus on the dependence of energy production on environmental variables such as irradiance, temperature, and wind speed rather than on construction details.

The analysis centres on the physical relationships necessary to understand how fluctuations in these parameters affect power output estimation.

This theoretical framework is preparatory to the subsequent chapters, providing the key to evaluating the impact of satellite database errors on plant planning.

1.1 Physical principles of photovoltaic conversion

Photovoltaic (PV) conversion is the physical process by which solar radiation energy is converted directly into electrical energy.

This phenomenon relies on the ability of specific semiconductor materials to absorb photons and release electrons, thereby generating an electric current when integrated into a closed circuit [1], [2].

1.1.1 Photovoltaic effect and p-n junction

The fundamental element of PV technology is the solar cell, primarily composed of silicon (Si). Solar cells electrically interconnected and encapsulated together form a photovoltaic module, hereafter also referred to as a photovoltaic panel as a synonymous term.

Photovoltaic cells operating principle lies in the electronic band structure of the semiconductor material: the valence band occupied by bonding electrons and the conduction band where electrons are free to move.

An energy gap E_g exists between these two bands. For silicon, this gap is approximately 1.12 eV at room temperature.

For the photovoltaic effect to occur, an incident photon must possess an energy E_{ph} greater than E_g. The photon energy is described by Planck's Law:

$$E_{ph} = \frac{h \cdot c}{\lambda} \quad 1.1$$

where:

- h = Planck's constant, 6.626×10^{-34} J·s
- c = speed of light in vacuum, 3.00×10^{8}m/s
- $\boldsymbol{\lambda}$ = wavelength of the photon.

If $E_{ph} \geq E_g$, the photon is absorbed, and an electron is excited from the valence band to the conduction band, creating an electron-hole pair.

However, the mere generation of charge carriers is insufficient; a separating force is required.

This is provided by the p-n junction, created by doping silicon with trivalent atoms, for example boron that is a p-layer and pentavalent atoms, for example phosphorus that is an n-layer.

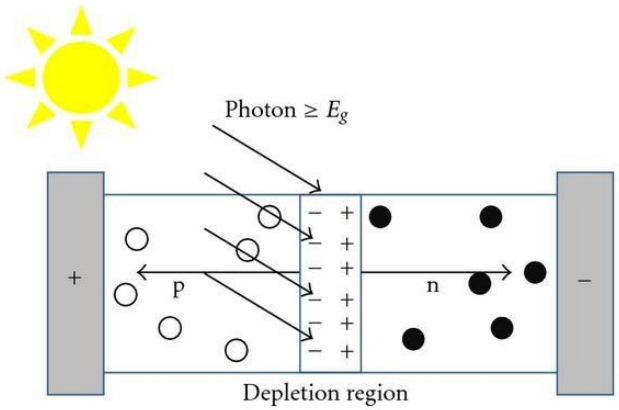

Figure 1.1 - Basic p-n junction solar cell [3].

At the interface of these layers, an internal electric field is established, called depletion zone, which drives electrons toward the n-region and holes toward the p-region, generating a drift current that opposes the natural diffusion current.

1.1.2 I-V characteristics and power curves

The electrical behaviour of a PV cell can be described using a single-diode equivalent circuit, consisting of an ideal current source in parallel with a diode and two parasitic resistances: series resistance R_s and shunt resistance R_{sh}.

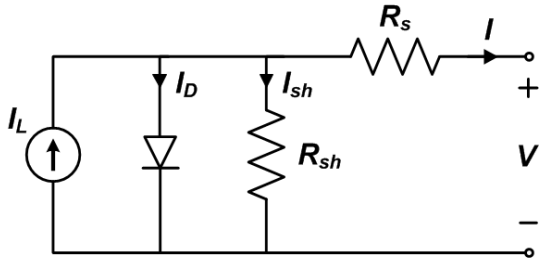

Figure 1.2 - Single diode equivalent circuit [4].

The fundamental equation describing the current-voltage I-V characteristic is:

$$I = I_{ph} - I_0 \left[exp\left(\frac{q(V+IR_S)}{nkT}\right) - 1 \right] - \frac{V+IR_S}{R_{sh}} \qquad 1.2$$

where:

- I_{ph} = photocurrent, directly proportional to irradiance
- I_0 = diode reverse saturation current
- n = diode ideality factor

- k = Boltzmann constant
- T= absolute temperature.

From the I-V curve, three key points fundamental to module characterization are identified:

- Short Circuit Current I_{sc}.: the maximum current generated when V = 0.
- Open Circuit Voltage V_{oc}.: the maximum voltage across the terminals when I = 0.
- Maximum Power Point, MPP: the point on the curve where the product $P_{max} = V \cdot I$ is maximized.

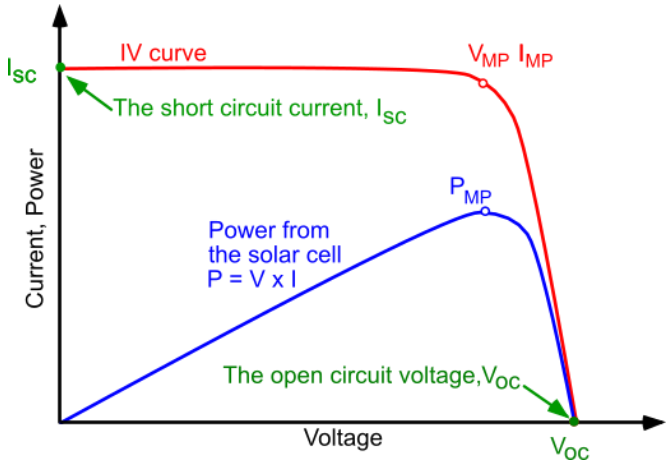

Figure 1.3 - Characteristic curve (red) and power curve (blue) [5].

1.1.3 Dependence of the I-V curve on irradiance and temperature

The performance of a photovoltaic system is not static; it is intrinsically linked to the environmental conditions of the installation site.

For the purposes of this thesis, understanding how a solar cell reacts to fluctuations in climate variables is essential, as these relationships define how errors in a meteorological dataset propagate through the final energy yield estimates.

The relationship between incident solar irradiance G and the generated current is characterized by a high degree of linearity.

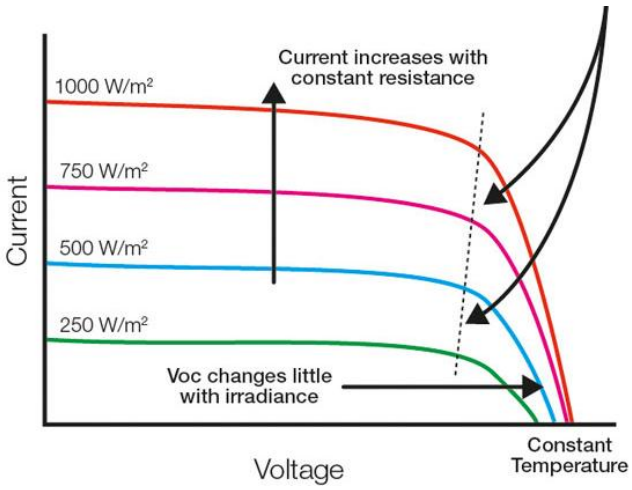

Figure 1.4 - Dependence of the I-V curve on irradiance [6].

While solar irradiance is the "fuel" of the system, temperature acts as a degrading factor. As the cell temperature T_c rises, due to both ambient heat and the thermalization of absorbed photons, the semiconductor's band gap narrows.

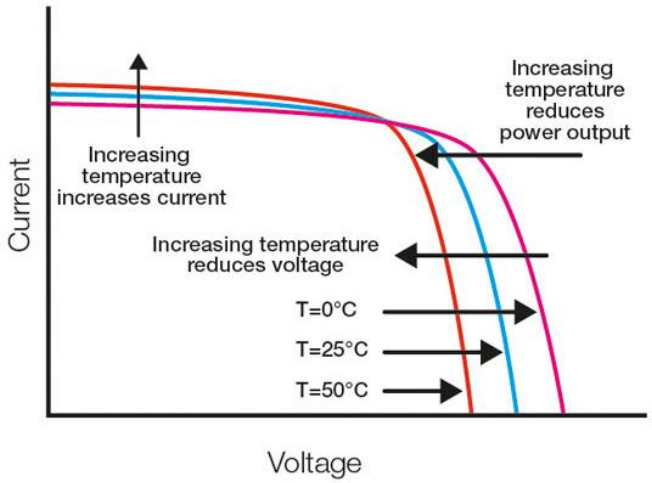

Figure 1.5 - Dependence of the I-V curve on irradiance [7].

Solar irradiance slightly facilitates the excitation of electrons, leading to a marginal increase in I_{sc}, it significantly increases the dark saturation current of the diode.

Physically, an increase in the flux of photons hitting the cell surface results in a proportional increase in the generation rate of electron-hole pairs. Consequently, the short-circuit current I_{sc} follows the equation:

$$I_{sc}(G, T_c) = I_{sc}^{STC} \cdot \frac{G}{G_{STC}} \cdot (1 + \alpha \cdot \Delta T_c) \quad 1.3$$

where:

- $I_{sc}(G, T_c)$ = short-circuit current under operating conditions
- I_{sc}^{STC} = nominal short-circuit current at standard test conditions (STC)
- G = incident solar irradiance on the module plane
- G_{STC} = reference irradiance, 1000 W/m^2
- α = temperature coefficient of the short-circuit current
- ΔT_c = deviation between the operating cell temperature and the reference temperature, $T_c - 25°C$.

On the other hand, the open-circuit voltage V_{oc} exhibits a logarithmic dependence on solar irradiance; it rises sharply at low light levels and quickly reaches a plateau. The most prominent effect of temperature phenomenon, instead, is a sharp drop in the open-circuit voltage V_{oc}, which for standard crystalline silicon modules typically decreases at a rate of -0.3% to -0.4% for every degree Celsius above the standard 25°C.

Since the reduction in voltage far outweighs the minor gain in current, the overall efficiency of the module degrades as it heats up and V_{oc} follows the equation:

$$V_{oc}(G, T_c) = V_{oc}^{STC} \cdot (1 + \beta \cdot \Delta T_c) + V_t \cdot \ln\left(\frac{G}{G_{STC}}\right) \quad 1.4$$

where:

- $V_{oc}(G, T_c)$ = open-circuit voltage under operating conditions
- V_{oc}^{STC} = nominal open-circuit voltage at standard test conditions (STC)
- β = temperature coefficient of the voltage
- ΔT_c = deviation between the operating cell temperature and the reference temperature
- G = incident solar irradiance on the module plane
- G_{STC} = reference irradiance, 1000 W/m^2

In practical applications, the cell temperature is rarely measured directly; it is instead derived from ambient temperature T_a and irradiance through empirical models such as the Nominal Operating Cell Temperature formula:

$$T_c = T_a + (NOCT - 20) \cdot \frac{G}{800} \quad 1.5$$

where:

- T_c = operating cell temperature
- T_a= ambient air temperature
- NOCT = nominal operating cell temperature, manufacturer parameter
- G = incident solar irradiance on the module plane
- 800 = reference irradiance for NOCT definition
- 20 = reference ambient temperature for NOCT definition.

This equation highlights a complex interaction for our error analysis: an inaccuracy in the ambient temperature data or a bias in the irradiance values will skew the calculation of the operating temperature, ultimately leading to a distorted estimation of the conversion efficiency. Understanding these dependencies is therefore paramount to quantifying the uncertainty of the entire energy model.

1.1.4 Energy production from PV systems

The estimation of energy production E_{pv} for a PV system can be expressed, as a first approximation, as:

$$E_{pv} = G_{total} \cdot \mathrm{A} \cdot \eta_{nom} \cdot \mathrm{PR} \qquad 1.6$$

where:

- G_{total} = global solar irradiation on the module plane, i.e. time integral of G
- A = active area of the PV generator
- η_{nom} = module efficiency under STC (1000 W/m², 25 °C)
- PR = performance ratio, a dimensionless quality factor accounting for all system losses excluding nominal efficiency.

The accuracy of the E_{pv} estimate depends linearly on the accuracy of the G data. Therefore, the quality of the solar irradiance database is the most determining factor in reducing uncertainty regarding yield.

1.2 Aerodynamic principles of wind energy conversion

Wind Turbines (WT) convert the kinetic energy of a moving air mass into mechanical energy at the rotor shaft, and subsequently into electrical energy.

Unlike PV systems, which are static, wind energy involves moving mechanical parts and complex fluid dynamics [8], [9].

1.2.1 Wind kinetic energy and extractable power

The instantaneous power available in the wind passing through an area A, which is the rotor swept area, is equal to the time derivative of its kinetic energy:

$$P_{wind} = \frac{1}{2} \cdot \rho \cdot A \cdot v^3 \quad 1.7$$

where:

- ρ = air density
- A = rotor area
- v = wind speed.

It is fundamental to note that wind speed is not constant with height due to surface friction, i.e. roughness.

To correct speed data from datasets, often provided at 10m or 100m, to the turbine hub height, the Wind Shear law is used, typically approximated by the logarithmic law or the Hellmann's power law:

$$v(h) = v_{ref} \cdot \left(\frac{h}{h_{ref}}\right)^{\alpha} \quad 1.8$$

where:

- v(h) = wind speed at the target height h
- v_{ref} = known wind speed at the reference height
- h = target height, e.g. turbine hub height
- h_{ref} = reference measurement height
- α = wind shear exponent (Hellmann coefficient), characterizing surface roughness.

In the data analysis, the shear coefficient α introduces an additional uncertainty variable.

1.2.2 Beltz limit and power curve

Not all wind kinetic energy can be converted into mechanical energy, as the air must retain some residual velocity to exit the rotor and allow new air mass to enter.

Betz's Law establishes the maximum physical limit extractable by an ideal turbine:

$$P_{ext} = C_p \cdot P_{wind} \quad 1.9$$

where:

- P_{ext} = mechanical power extracted by the rotor
- P_{wind} = available kinetic power in the wind stream.

The power coefficient C_p represents the aerodynamic efficiency of the rotor. The maximum value of C_p corresponds to $\frac{16}{27} \approx 0.593$ but in real turbines, due to aerodynamic drag and mechanical losses, the maximum C_p typically ranges between 0.40 and 0.50.

The relationship between extracted power and wind speed is described by the power curve, divided into four operating regions.

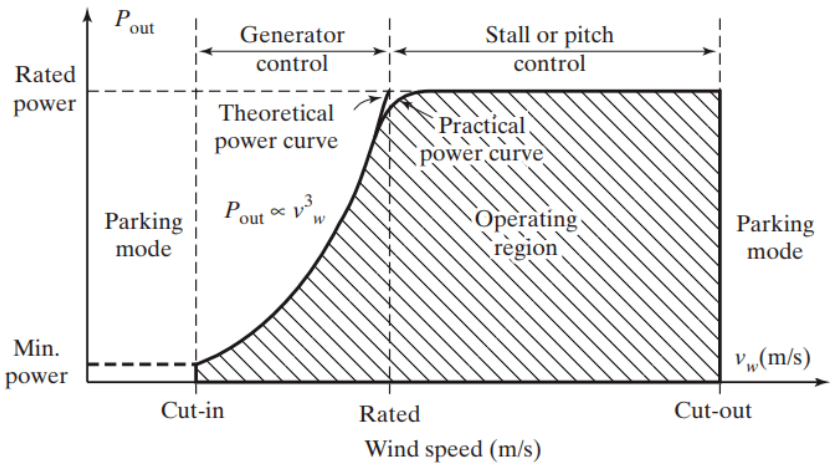

Figure 1.6 - Wind turbine power curve [10].

1. Below cut-in speed: the wind is too weak to overcome friction; the turbine remains stationary $P = 0$.
2. Ramp between cut-in and rated speed: power increases cubically with wind speed. In this area, efficiency C_p is maximized.
3. Rated power, plateau: once nominal power is reached, the control system limits energy absorption to prevent generator damage. Power remains constant despite increasing wind speeds.
4. Above cut-out speed: The wind is too strong; the turbine is braked for safety $P = 0$.

1.2.3 Dependence of the WT power on wind speed

The cubic dependence of power on wind speed showed with Eq. 1.7 makes wind resource estimation extremely sensitive to data errors.

Mathematically, if we consider a relative error in speed δv, the error in power P will be approximately:

$$\delta P \approx 3\, \delta v \tag{1.10}$$

A small 10% error in wind speed estimation, for example a dataset indicating 9 m/s instead of 10 m/s, results in an error of 27 - 30% in estimated available power.

Furthermore, air density ρ enters the equation linearly. Since ρ varies inversely with temperature T, errors in the temperature dataset also affect wind yield, albeit to a lesser extent than wind speed.

1.2.4 Energy production from WT systems

The Annual Energy Production is not calculated based on average speed but by integrating the turbine power curve $P(v)$ with the wind probability distribution at the specific site:

$$AEP = 8760 \int_{Vcut-in}^{Vcut-out} P(v)\, f(v) dv \tag{1.11}$$

where:

- AEP = annual energy production
- 8760 = number of hours in a standard year
- v_{cut-in} = minimum operational wind speed, start
- $v_{cut-out}$ = maximum operational wind speed, safety stop
- P(v) = turbine power output as a function of wind speed
- f(v) = probability density function of wind speed.

This calculation highlights how the production error depends on the overlap between the wind frequency curve and the turbine power curve.

Speed estimation errors in the steep section of the power curve carry much more weight than errors in the plateau or cut-off zones.

Chapter 2

2 Energy context in Morocco

This Chapter presents the general context of Morocco and examines how the renewable energy sector is situated within it.

Section 2.1 is focusing on its geographical characteristics, resource distribution, mapping of the existing renewable power plants and transmission grids.

Section 2.2 provides a legislative framework, historical energy background and an analysis of national energy policies. This results useful to offer a comprehensive picture of the country under study and of how energy production, management, and commercialization are addressed.

In this context, it is important to note that the Moroccan energy sector is regulated at the national level and does not rely on supranational organizations such as the European Union.

2.1 Distribution of energy sources in Morocco

In Section 2.1.1, maps illustrating the spatial distribution of energy resources are provided; in particular, solar and wind resources are analysed in detail.

In Sections 2.1.2 existing renewable energy power plants on the territory are presented.

In Section 2.1.3 electrical transmission network in Morocco is shown, which plays a crucial role in identifying areas of greater interest for the development of photovoltaic and wind power plants.

2.1.1 Mapping of territories and energy sources

Morocco is a North African country strategically positioned between the Atlantic Ocean and the Mediterranean Sea. Its geographic location has historically established it as a nexus connecting Africa, Europe, and the Middle East, thereby facilitating cultural, commercial, and political exchanges. Following its independence from France and Spain in 1956, the Kingdom of Morocco consolidated its territorial and political identity under a constitutional monarchy. The administrative capital is Rabat.

The national territory is organized into 12 administrative regions, exhibiting substantial landscape diversity: from the coastal plains bordering both seas, to the Atlas mountain ranges, and extending into the desert areas of Western Sahara. This strategic location has had a profound impact on economic development, positioning Morocco as a key hub for maritime trade and a country with significant potential across multiple sectors [11].

Figure 2.1 - Geographical position of Morocco [12].

The distribution of global horizontal irradiance (GHI) in Morocco exhibits a clear geographic gradient, with values increasing from north to south, i.e., from the coastal areas toward the interior.

In the northern belt, including locations such as Tangier, the influence of the Mediterranean climate and Atlantic currents results in the lowest irradiance levels

in the country, with daily totals ranging from 4.8 to 5.0 kWh/m² and annual totals between 1753 and 1826 kWh/m².

In the central regions, encompassing Casablanca, Kenitra, Fes, and Meknes, irradiance gradually increases, reaching daily totals of 5.2-5.6 kWh/m² and annual totals of 1899-2045 kWh/m², corresponding to areas characterized by a drier climate and reduced cloud cover.

The inland and southwestern zones, such as Marrakesh, Agadir, and Guelmim, register daily totals between 5.8 and 6.0 kWh/m² and annual totals of 2118-2191 kWh/m², due to higher aridity and greater atmospheric stability.

Maximum values are observed in the pre-desert and Saharan regions of the southeast, particularly in the areas of Errachidia and Ouarzazate, where irradiance exceeds 6.2 kWh/m² per day, reaching annual peaks of approximately 2264 kWh/m². These characteristics position southern and Saharan Morocco among the most promising regions in North Africa for the deployment of photovoltaic and concentrated solar power plants, highlighting how geographic factors constitute a decisive element in the planning of renewable energy infrastructure [13].

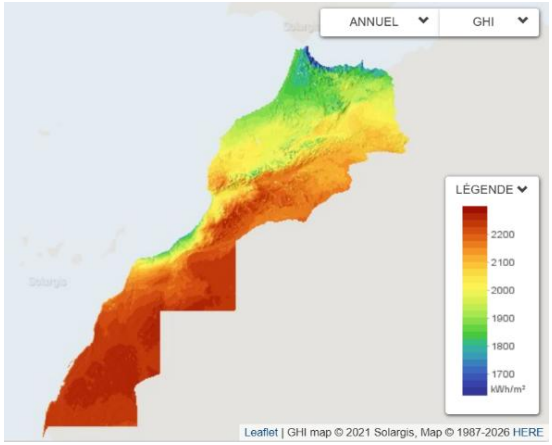

Figure 2.2 - Mapping of GHI in the different areas of Morocco [14].

The combination of geographic location, climatic conditions, and terrain morphology makes Morocco one of the countries with the highest wind energy potential in the North African region, with areas particularly suitable for the development of large-scale energy infrastructure.

Morocco possesses a wind potential characterized by a pronounced gradient between the Atlantic coastal belts and the inland regions [15]. At the national scale, at a height of 50 meters, average wind speeds generally range between 4 and 6 m/s,

with intensifications along coastal areas and zones exposed to westerly winds. At 150 meters, due to the vertical wind profile, these values increase significantly, reaching 7-9 m/s in the areas with the highest potential. This configuration confirms the country's strong wind energy vocation, particularly along the Atlantic coast and in regions where local morphology promotes wind channelling.

Within this overall framework, certain areas are strategically significant for the development of wind farms. The Rabat area, located on the central Atlantic coast, exhibits wind speeds at 50 meters generally between 4 and 5 m/s, increasing to approximately 6-7 m/s at 150 meters, making the area suitable for modern-generation turbines. Further south, the Tarfaya region represents one of Morocco's primary wind energy hubs: here, wind speeds frequently exceed 6-7 m/s at 50 meters and reach 8-9 m/s at 150 meters, due to direct exposure to Atlantic currents and minimal orographic obstacles. Finally, the Tangier area, influenced by wind channelling through the Strait of Gibraltar, shows speeds around 6 m/s at 50 meters and 7-8 m/s at 150 meters, establishing it as an additional key node for wind energy production [16].

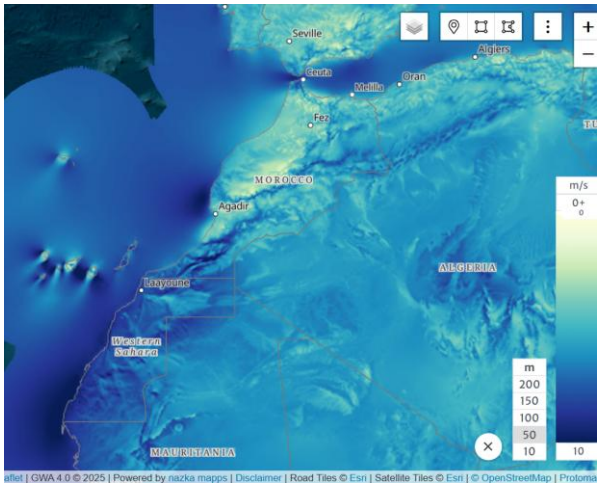

Figure 2.3 - - Mapping of wind speed at 50 meters height in the different areas of Morocco [16].

Finally, certain areas exhibit a significant simultaneity of solar and wind resources, making them particularly suitable for hybrid systems. Among these, Dakhla and Laayoune on the southwestern Atlantic coast experience consistent winds and high

solar irradiance and are frequently included in studies on the complementarity of renewable sources.

Tarfaya also demonstrates steady winds combined with high solar potential, as highlighted in analyses of capacity factors and hybrid systems. In the northwest, Tetouan combines seasonal wind resources with adequate solar irradiance, which is useful for studies of seasonal complementarity.

The Guelmim-Oued Noun region, the site of the Xlinks Morocco–UK Power Project, represents a real-world case of large-scale integration of solar fields and wind farms with storage [17]. These sites are often analysed using temporal complementarity indices based on historical wind and solar irradiance series, providing methodological and practical data for the design of hybrid systems in Morocco [18].

2.1.2 Mapping of existing PV and WT power plants

From the perspective of infrastructure and energy facilities, Morocco has been actively engaged in planning and construction activities, particularly over the last decade. Different data collection sources provide differing results regarding the number of wind and solar power plants operating within the country; however, this discrepancy depends on the selection criteria adopted by each source.

Open Infrastructure Map provides a map identifying a total of 82 plants, including both wind (WT) and photovoltaic (PV) facilities, divided into 16 wind plants with a maximum installed capacity of 1,177 MW and 66 solar plants with a maximum installed capacity of 1,135 MW [19]. It is shown a graphical representation of the position of the different plants filtered with the ≥ 1 MW capacity and the operational condition rather than the planned one.

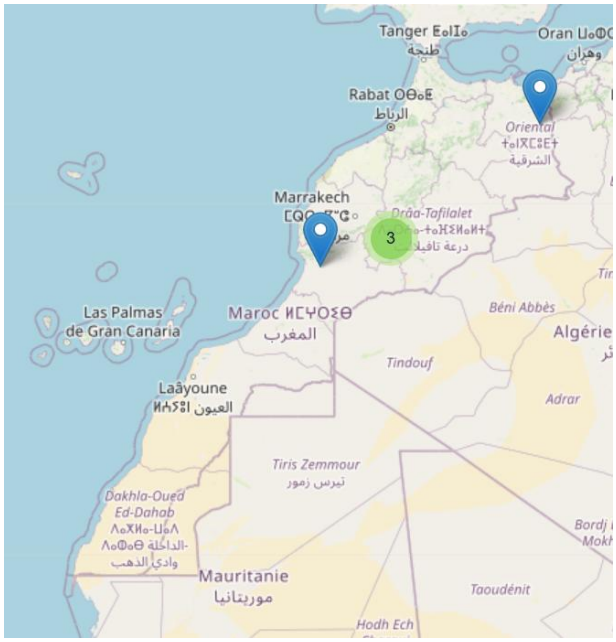

Figure 2.4 – Map of the existing PV plants in Morocco [20].

Figure 2.5 – Map of the existing WT plants in Morocco [21].

For several photovoltaic and wind plants, names and capacities are not publicly available; this is related to the size threshold of the plant considered prior to publication. Open Infrastructure Map, in fact, counts each individual entity, including small power plants and sub-units.

The second database, the Global Power Plant Database [22], considers 11 wind plants and 5 solar plants. These are utility-scale facilities with capacities ≥ 1 MW; the database often aggregates multiple units connected to the same power station into a single record. This criterion is more stringent and therefore results in a lower number of plants compared to the previous source, but it is consistent with the analysis of electrical power systems.

The third and final database considered is provided by RePP Africa [23]. In this case, all African power plants are listed, including those already in operation, under construction, or planned. To obtain a filtered output from RePP Africa, it is necessary to download the Excel file containing data for all African countries and then select Morocco. The resulting dataset includes 22 wind plants and 24 solar plants.

The solar plants identified by RePP Africa are now analysed in detail; their specifications and names are reported in the table below, where in the column "Operational status" is indicated as O = Operating, U = Under construction and P = Planned.

Table 2.1 - List of PV plants in Morocco [24].

Solar Power Plant Name	**Operational Status**	**Capacity (MW)**	**Plant Type**	**Year of Start**
Noor Tafilalt - Noor Missour	O	40,0	PV	2019
Noor Tafilalt - Noor Erfoud	O	40,0	PV	2019
Noor Tafilalt - Noor Zagora	O	40,0	PV	2019
Aïn Beni Mathar	O	20,0	CSP	2011
Maghreb Industries	O	1,3	PV	2017
Aït Bahar	O	2,0	CSP	2013
Ouarzazate Noor 3	O	150,0	CSP	2016
Ouarzazate Noor 2	O	200,0	CSP	2018
Ouarzazate Noor 1	O	160,0	CSP	2018
Ouarzazate Noor 4	O	72,0	PV	2017

Noor Atlas Tan-Tan	P	36,0	PV	
Noor Atlas Tata	P	36,0	PV	
Taroudant	P	36,0	PV	
Sidi Bennour	P	40,0	PV	
Bejaâd	P	40,0	PV	
Nexans Maroc Factory	P	2,5	PV	
El Hajeb	P	36,0	PV	
Noor Midelt 2	P	230,0	CSP	
Noor Midelt1	P	800,0	CSP	2022
Noor Atlas Boudnib	P	36,0	PV	
Outat el Haj	P	36,0	PV	
Noor Atlas Enjil	P	36,0	PV	
Noor 2 Aïn Beni Mathar	P	184,0	PV	
Noor Atlas Aïn Beni Mathar	P	36,0	PV	

The results are updated to 2022 and are considered current and reliable. In this case as well, only 10 of these plants are operational and most of them are concentrated in the Ouarzazate solar complex.

As for wind power plants, RePP Africa also provides an overview of existing facilities in Morocco, reporting a total of 22 plants, of which 19 are operational, as reported in the table below.

Table 2.2 - List of WT plants in Morocco [25].

Wind Power Plant	**Operational Status**	**Capacity (MW)**	**Year of Start**
Tarfaya	O	300,00	2014
Akhfennir	O	101,87	2013

Akhfennir2	O	100,00	2016
Tarfayer	O	60,35	2007
Oualidia 2	O	3,60	2021
Oualidia 1	O	33,00	2021
Midelt	O	180,00	2021
Taza	U	150,00	2022
Tetouan 1 (Lafarge)	O	10,00	2009
Tetouan 2	O	10,20	2005
Tetouan 3	O	12,00	2009
Khalladi	O	120,00	2017
Tanger 1	O	107,10	2010
Tanger 2	O	33,15	2010
Al Kouida Al Baida 1	O	50,40	2000
Al Kouida Al Baida 2	O	3,50	2001
Haouma	O	50,60	2013
Airport Mohammed V Industrial	O	10,00	2014
Al Koudia Al Baida 2	P	200,00	2024
Amougdoul	O	60,00	2012
Jbel Lahdid	P	270,00	2023
Essaouira	O	60,35	2007

2.1.3 Mapping of transmissions grids

In this section, the Moroccan electricity transmission network is analysed using the maps provided by the Open Infrastructure Map platform [26]. From these data, the network appears as a clearly hierarchical system, strongly shaped by the spatial distribution of electrical loads and by the geographic concentration of the country's economic and industrial activities.

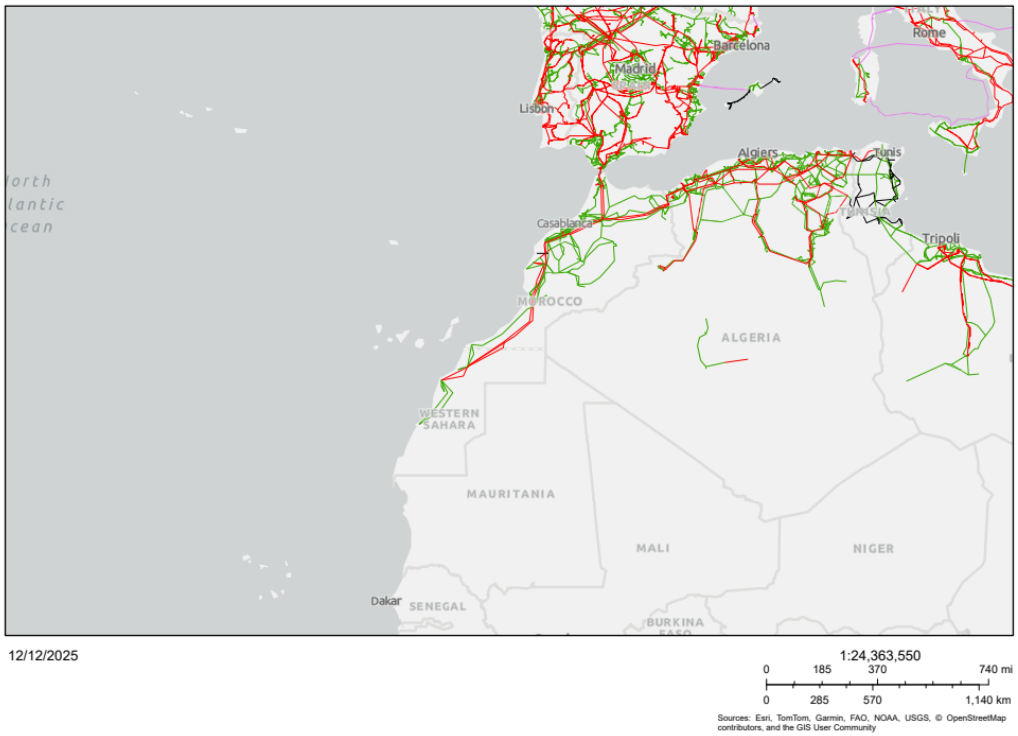

Figure 2.6 - Map of the exiting transmission grid in Morocco.

The 400 kV level, shown in red in the previous figure, forms the structural backbone of the system and develops along predominantly north–south corridors, linking the main demand centres in the northern regions and along the Atlantic coastal belt with the central and southern parts of the country, extending as far as Western Sahara.

These lines, which are relatively weakly meshed and characterized by long, continuous alignments, are designed to carry large power flows over long distances, ensuring the interconnection between major generation hubs and load centres and enabling the integration of the Moroccan power system into the wider Mediterranean regional context through international interconnections.

Superimposed on this backbone is the 225 kV network, represented in green, which is significantly more extensive and highly meshed, particularly along the Atlantic coast and in northern Morocco, where infrastructure density mirrors the concentration of urban and industrial activities.

This voltage level fulfils a critical intermediate function by distributing power from the 400 kV backbone, enhancing system redundancy and operational flexibility, and improving security of supply through the availability of alternative transmission paths.

The 50–90 kV network, shown in purple, is instead characterized by a fragmented and spatially localized structure, mainly concentrated around urban areas and local load centers, and primarily serves as a sub-regional supply and support layer rather than as a long-distance transmission system.

When the analysis focuses in greater detail on the main nodal points of the system, it emerges that the thermal power plants of Jorf Lasfar, Mohammedia and Kénitra supply the coastal region between Casablanca and Rabat, where the bulk of industrial and urban electricity demand is concentrated.

These generation sites are interconnected through a dense network of transmission lines that radiate inland, ensuring both high transfer capacity and adequate supply to the hinterland.

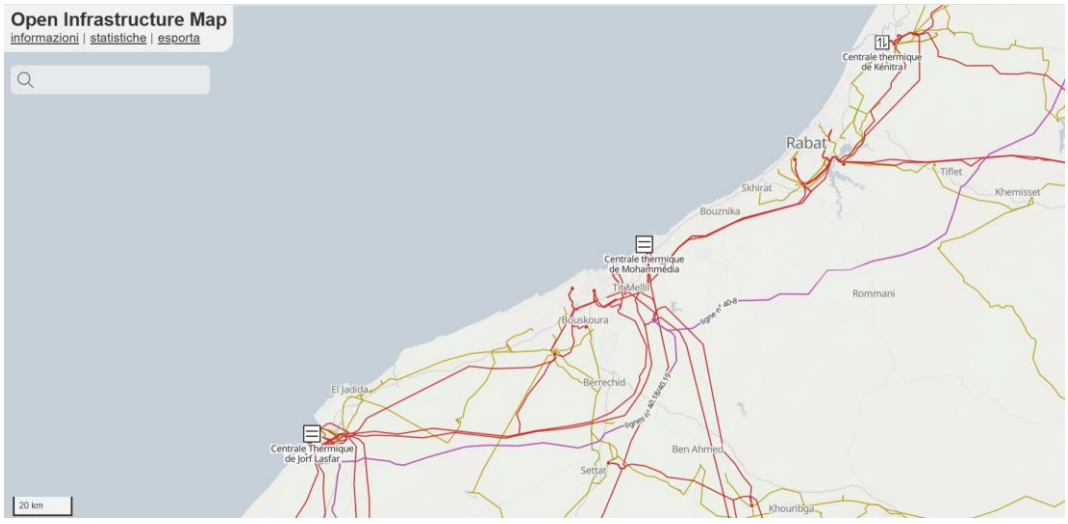

Figure 2.7 - Map of the transmission grids in the oceanic part of Morocco [26].

In the north of the country, the Tahaddart combined-cycle power plant near Tangier represents a strategic node, as it constitutes the Moroccan terminal of the 400 kV submarine interconnection with Spain across the Strait of Gibraltar, enabling bidirectional electricity exchanges with the European power system.

From this node, transmission lines extend towards Tétouan, Chefchaouen and Larache, forming an energy corridor that integrates local generation with the national grid.

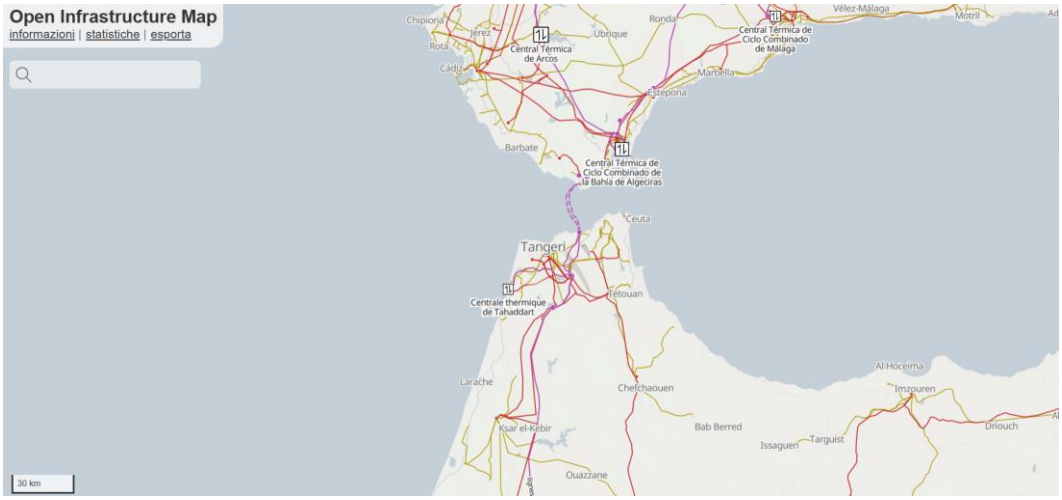

Figure 2.8 - Map of the transmission grids in the northern part of Morocco [26].

In the southern regions, large-scale wind farms such as Tarfaya and Akhfenir are connected to the transmission system through 400 kV lines extending towards Laâyoune, thereby supporting the integration of renewable energy sources into the Moroccan power system.

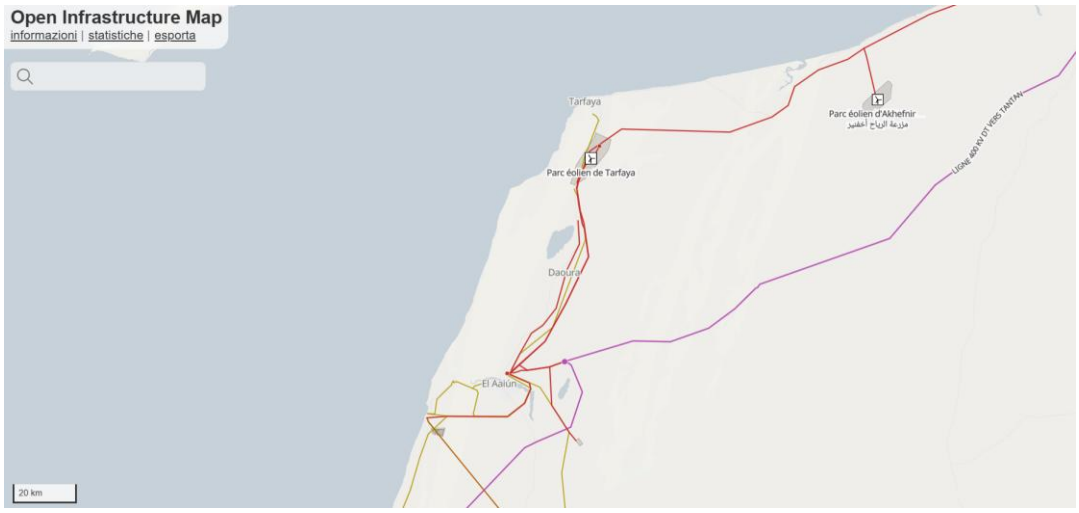

Figure 2.9 - Map of the transmission grids in the southern part of Morocco [26].

Overall, the network exhibits a progressive decrease in meshing density towards the inland and southern regions of the country, where the transmission structure becomes simpler and the role of the extra-high-voltage backbone becomes dominant, delineating a system designed to accommodate large-scale energy transfers along a limited number of strategic corridors while simultaneously providing dense and reliable coverage to the most economically dynamic areas. Furthermore, Morocco is planning a future electrical interconnection with Mauritania, which is expected to further strengthen its strategic role as an energy bridge between Europe and Africa.

2.2 State of the art of PV and WT technologies in Morocco

The energy transition currently represents one of the primary global priorities, aimed at reducing dependence on fossil fuels in favour of renewable sources such as solar and wind energy.

Within this global context, Morocco has traditionally exhibited a high dependence on fossil fuel imports, resulting in a corresponding vulnerability to their price fluctuations.

At present, the country has initiated a profound transformation process that has positioned it as one of the leading nations in Africa in terms of installed renewable capacity and international energy cooperation. Indeed, Morocco possesses significant potential in renewable energy sources, as discussed in the preceding Sections.

2.2.1 Historical evolution of the renewable energy sector

This section presents a chronological reconstruction of the evolution of Morocco's energy sector from 1990 to the present, highlighting the main reforms, strategies, and initiatives that have facilitated the growing integration of renewable energy sources. It provides an overview of the institutional, infrastructural, and technological milestones that have transformed the country into a key actor in the regional energy transition [27], [28].

During the 1990s, the national energy system was almost entirely based on imported fossil fuels, particularly oil and coal. Electricity demand was growing at rates exceeding 5% per year, while dependence on foreign sources surpassed 90%, with significant repercussions on the trade balance and vulnerability to international price fluctuations. Furthermore, the electrical infrastructure remained underdeveloped in rural areas, and generation capacity was primarily based on small- to medium-scale coal and diesel power plants.

The establishment of ONE (Office National de l'Électricité) in 1997 marked a first institutional turning point: the organization assumed the role of sole grid operator and promoter of national electrification. Through the Programme d'Électrification Rurale Globale, the country achieved one of the fastest rural electrification pathways in North Africa, raising the access rate from less than 20% to over 95% within approximately a decade. This infrastructural expansion laid the foundation for the integration of future renewable energy capacities.

Between 2006 and 2009, regulatory and economic reforms were introduced that laid the foundation for the subsequent transformation of the energy sector. The partial liberalization of the sector enabled independent power generation (IPP) and the entry of private capital through long-term contracts. Concurrently, the sharp increase in global oil prices (2007–2008) reinforced the need for diversification.

A decisive step was the adoption of the 2009 National Energy Strategy, a document that remains central to energy planning. Its main objectives are to reduce dependence on imports, develop significant renewable capacity (42% by 2020), and exploit Morocco's solar and wind potential, which ranks among the most competitive internationally.

After a prolonged period of reliance on fossil fuel imports, the 2009 strategy introduced a top-down approach focused on large-scale renewable projects, particularly in solar energy. While effective, this strategy entailed high costs and a highly centralized governance structure dominated by the state apparatus. The recent decline in solar costs has facilitated the emergence of decentralized renewable initiatives, such as the MG-Farm pilot projects, which require enabling institutional measures, including grid access for distributed producers.

In 2009, MASEN (Moroccan Agency for Sustainable Energy) was established as the agency responsible for developing large-scale solar projects. Its creation introduced an innovative governance model based on centralized planning, international tenders, public-private partnerships, and multilateral financing. Within this framework, the Moroccan Solar Plan was launched, aiming to install 2,000 MW of solar capacity by 2020.

The flagship project is the Noor Ouarzazate complex, intended to become one of the largest solar infrastructures worldwide.

Between 2012 and 2014, construction began on the various phases of the Noor complex (CSP and PV), consolidating Morocco's role as an international reference for concentrated solar power technologies. Simultaneously, the wind energy sector expanded, with large-scale projects in the coastal and southern regions. During this period, wind farms such as Tarfaya and Akhfenir were developed, supported by favorable wind conditions and competitive financial models.

Morocco has established itself as one of the most dynamic middle-income countries in promoting energy and climate policies, in line with the National Energy Strategy, which has profoundly reshaped the national energy landscape. The strategy, launched in 2009 and updated in 2015, defines clear targets for sustainability and reducing dependence on fossil fuels, aiming for 42% installed renewable capacity by 2020 and 52% by 2030.

The 2016 COP22 in Marrakech further enhanced the international visibility of Morocco's strategy and accelerated investments. Between 2015 and 2018, Noor I, Noor II, and Noor III were commissioned, completing one of the world's most advanced CSP complexes.

Since 2018, the country has implemented PPA-based tenders and strengthened interconnections with Spain, laying the groundwork for future export flows. Renewables have become a structural component of the energy mix, alongside intensified programs for grid modernization and efficiency improvements.

Morocco's commitment to the objectives of the Marrakech and Paris Agreements also entails initiatives for nearly zero-energy buildings (NZEBs), aimed at reducing energy consumption and emissions in the building sector. The MENA region is currently undergoing a transition toward more sustainable energy systems, consistent with a shift toward more participatory governance models. This transition represents a strategic opportunity to reduce dependence on imported fossil fuels in favor of local renewable resources, particularly solar and wind energy.

Over the past two decades, Morocco has made significant progress in the development of renewable energy, especially wind and solar. The share of renewables, including hydropower, has increased, and the country has been recognized as a pioneer of the energy transition in Africa, accounting for 11% of the total energy supply. Additionally, Morocco has made notable strides toward the 42% renewable capacity target by 2020 (ISPI 2022), reaching an estimated installed capacity of 38% in 2022.

The most recent phase, from 2020 to 2025, is characterized by the emergence of green hydrogen as a core element of the national strategy. The National Hydrogen Commission was established, and sectoral roadmaps were published, envisioning the use of the country's vast renewable potential for industrial applications and export to Europe.

Flagship projects such as Xlinks (a submarine interconnection between Morocco and the United Kingdom) mark the country's entry into large-scale international renewable energy markets. In 2025, the government announced the gradual phase-out of coal by 2040, accelerating the development of photovoltaic systems and energy storage to ensure security and flexibility.

The result is an energy system undergoing advanced transformation, based on solid institutions, long-term investments, and a coherent strategic vision. Today, Morocco is positioned as a potential regional hub for renewable energy production, energy storage solutions, and low-emission energy carriers.

2.2.2 Current energy policies in Morocco

The regulatory framework for renewable energy in Morocco originated with the National Energy Strategy of 2009, which marked the transition from a system heavily dependent on imported fossil fuels to a model oriented toward decarbonization, energy security, and the attraction of private investment.

The regulatory system is based on a set of key laws (in particular Laws 13–09, 57–09, 37–16, and 48–15) governing electricity generation from renewable sources, grid access, the distinction between stand-alone and grid-connected systems, and the roles of public institutions and private operators [27], [28], [29], [30], [31]. The framework has progressively evolved from a centralized, state-led model toward one more open to market mechanisms, while maintaining strong public control over critical infrastructure.

The Moroccan electricity sector is characterized by a highly centralized institutional structure, with a clear separation of roles. The main institutions managing the sector are the following:

- ONEE (Office National de l'Électricité et de l'Eau Potable) It is the historical operator and monopolist of electricity transmission and distribution. It retains exclusive control over the national high-voltage grid.

- MASEN (Moroccan Agency for Sustainable Energy) Public agency responsible for the development of large-scale renewable energy projects (solar, wind, and hydropower), mainly through Public–Private Partnership (PPP) models.

- ANRE (Autorité Nationale de Régulation de l'Électricité) Regulatory authority established to ensure transparency, fairness in grid access, and arbitration among operators. However, literature highlights that its powers remain limited, thereby reducing the effectiveness of independent regulation.

About legislation, several fundamental laws are listed below, representing the pillars of the current policies regulating Morocco.

Concerning power generation, Law 13–09 allows private renewable electricity production, sale to final customers or to ONEE, and the export of electricity (subject to authorization). Nevertheless, the framework remains complex and administratively burdensome, especially for small- and medium-scale projects.

Electricity transmission and distribution, by contrast, remain a public monopoly of ONEE. The main regulatory elements include guaranteed grid access for renewable producers, the requirement for technical and financial agreements with ONEE for connection, and connection costs that are often high and negotiated on a case-by-case basis.

Additional legislation also applies to stand-alone, i.e., off-grid, renewable energy systems. These are managed in a relatively simple manner and are particularly relevant for rural areas, agriculture (solar irrigation), and decentralized electrification.

The regulatory framework allows the installation and use of stand-alone systems without an obligation to connect to the grid, with reduced authorization requirements and indirect incentives through rural development programs. However, a clear system of dedicated economic incentives, uniform technical standards, and mechanisms for future integration with the grid is still lacking.

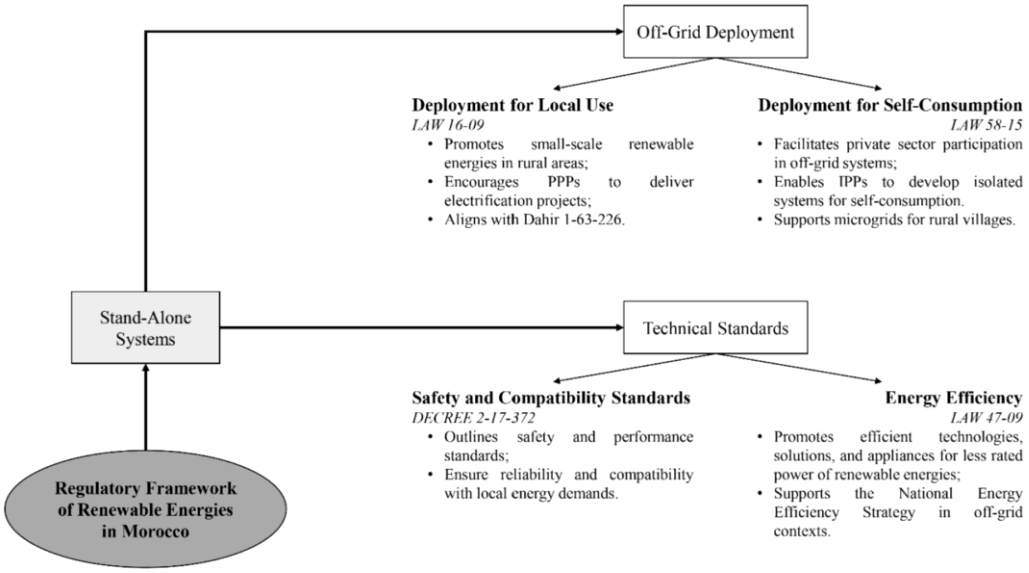

Figure 2.10 - Regulatory framework for Stand-Alone renewable energies [32].

Finally, grid-connected systems are analyzed, representing the core of Morocco's renewable energy strategy. The regulatory framework connection to the low-, medium-, and high-voltage grid depending on plant size, multi-level authorizations (ministerial, ONEE, local authorities), and tariffs and access conditions that are not fully standardized.

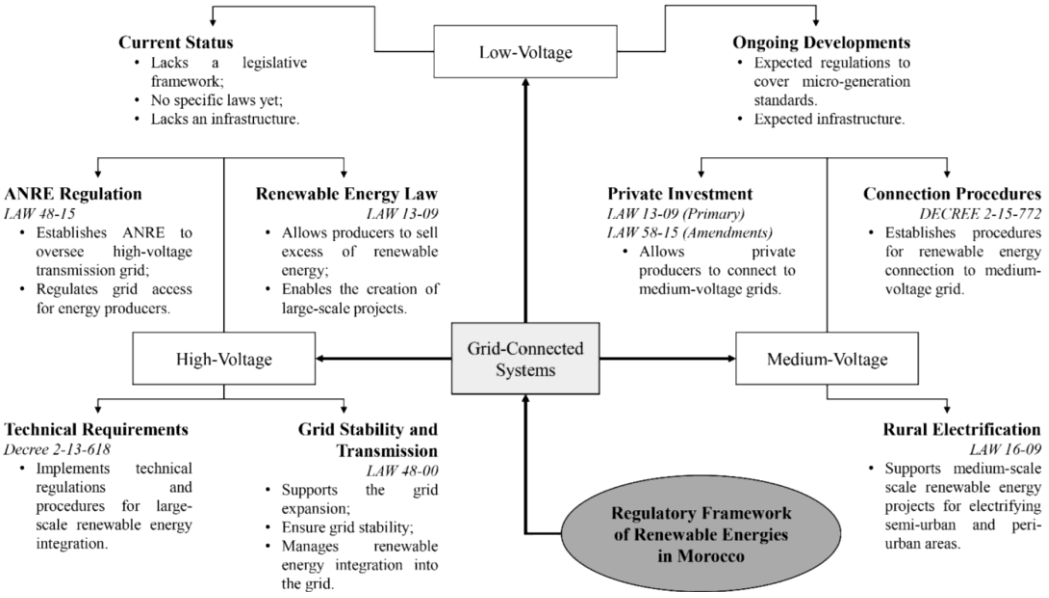

Figure 2.11 - Regulatory framework for Grid-Connected renewable energies [32].

Large-scale projects are generally developed by MASEN through competitive auctions, while private projects still face regulatory uncertainty, lengthy approval processes, and contractual dependence on ONEE. Although Morocco is an advanced country compared to other nations in the region, the system requires structural reforms to foster widespread private investment and decentralized generation.

2.2.3 Future prospectives for renewable energy development

Morocco has defined a long-term climate strategy strongly oriented toward decarbonization, consistent with the Paris Agreement and the Sustainable Development Goals [30], [33], [34].

Low-carbon strategies are structured along the 2030 and 2050 time horizons and articulated through three scenarios:

- Business-as-Usual (BAU): continuation of current policies, with high dependence on fossil fuels.
- Increased Ambition (IA): acceleration of renewable energy deployment and energy efficiency.
- Green Development (GD): structural transformation of the energy system with deep decarbonization.

The 2030 strategies are formalized in the Nationally Determined Contributions (NDCs) and envisage achieving 52% of installed renewable capacity; a balanced development of solar (20%), wind (20%), and hydropower (12%), as well as the integration of energy storage systems.

By 2050, Morocco instead aims to produce 150 TWh/year from renewable sources, install more than 30 GW of renewable capacity, and integrate renewables with Power-to-X technologies, green hydrogen, and biomass.

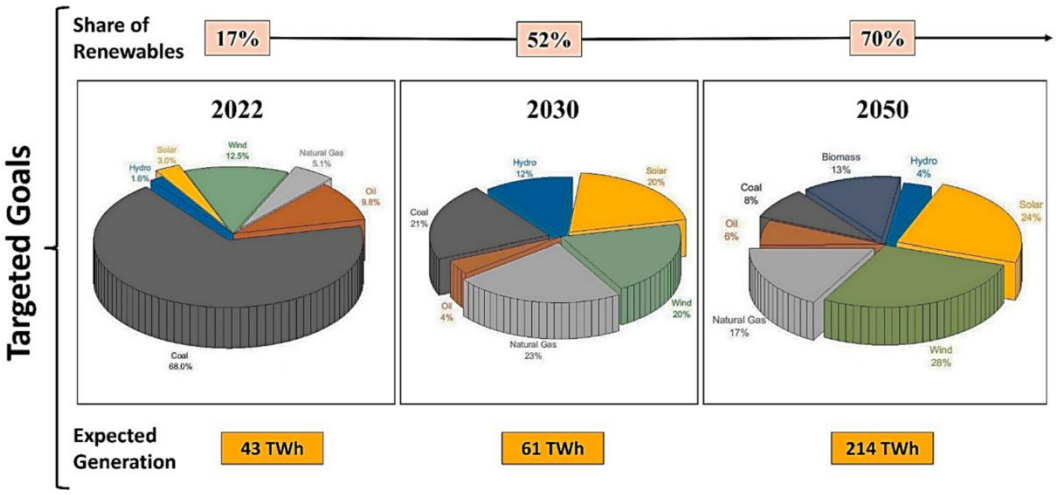

Figure 2.12 - Targeted goals of electricity production mix in Morocco.

The power sector represents the main area for renewable energy development, with projects primarily implemented through MASEN and Public–Private Partnership (PPP) models, with strong involvement of international investors.

Future projects aim to expand renewable capacity beyond 2030, integrate generation, storage, and flexibility, and place particular emphasis on hybrid plants (PV + CSP), next-generation wind farms, and green hydrogen infrastructure.

In recent years, reforms have also concerned policy frameworks, focusing on strengthening the powers of ANRE as an independent regulator, simplifying authorization procedures, increasing transparency in grid access, and providing regulatory support for decentralized generation.

The strengthening of institutions such as IRESEN (Institut de Recherche en Énergie Solaire et Énergies Nouvelles) and MASCIR (Moroccan Foundation for Advanced Science, Innovation and Research) is considered essential to support national innovation and reduce dependence on foreign technologies; therefore, the objective is to translate these strategies into operational market reforms to enable Morocco's emancipation in the coming years.

2.3 Significance of this thesis study

This thesis assumes a central relevance in the context of Morocco's energy transition, a country that in recent years has intensified investments in solar and wind infrastructures to reduce energy dependence and increase the security of the national electricity system.

The quality of the design, economic evaluation, and grid integration of renewable plants critically depends on the accuracy of the meteorological data used, in particular solar irradiance and wind speed. However, the available databases present significant differences in terms of resolution, methodology, and performance compared to on-site measured data [35], [36], [37]. These discrepancies can substantially influence the estimation of energy potential: in the case of wind power, for example, even small errors in wind speed translate into large differences in the estimated power due to its cubic dependence.

The importance of this research lies precisely in the need to systematically assess which database offers the most reliable estimates in the different climatic regions of Morocco (desert areas, coastal areas, continental regions, and mountainous areas) and which represents the best alternative in cases where real data are not available or are limited. Recent studies have shown that the performance of a database is not uniform across the territory and that local biases can compromise the validity of energy simulations [38].

For this reason, a comparative analysis based on robust statistical metrics such as bias, RMSE, correlation, and distributions constitutes an essential tool to reduce uncertainty in design and improve the reliability of forecasts.

The proposed work therefore does not limit itself to a descriptive comparison between meteorological databases but contributes to the definition of a replicable methodology useful for designers, researchers, and policymakers. The identification of the most suitable database for the different climatic zones of Morocco and of the necessary corrections represents a fundamental step to support more efficient, reliable, and sustainable energy planning, especially in contexts where the absence of measured data still constitutes a relevant criticality.

Chapter 3

3 Analysis of different databases input for solar PV and WT

This Chapter presents a quantitative analysis of solar and wind resources. For each technology, a set of representative parameters is selected and analysed to derive meaningful conclusions, with particular emphasis on the consistency among the different databases employed by the various software tools.

Section 3.1 introduces this analysis from a literature-based perspective.

Sections 3.2 and 3.3 then present the results from a graphical standpoint, comparing the outputs of the different databases through daily, weekly and annual plots. For photovoltaic resources, the analysis focuses on the cities of Rabat and Ouarzazate, while for wind technology it considers Rabat, Tangier, and Tarfaya.

Section 3.4 provides an error analysis conducted at an inter-comparative level among the selected databases, without yet performing a validation against measured or real-world data.

3.1 Selection of the databases to compare

The objective of this Chapter is to compare different databases obtained from different software in order to select the best one for further comparisons. Meteorological databases include the parameters necessary for the subsequent analysis of electric power generation planification: solar irradiance and air temperature for photovoltaic production; wind speed for wind production, as illustrated in the following scheme.

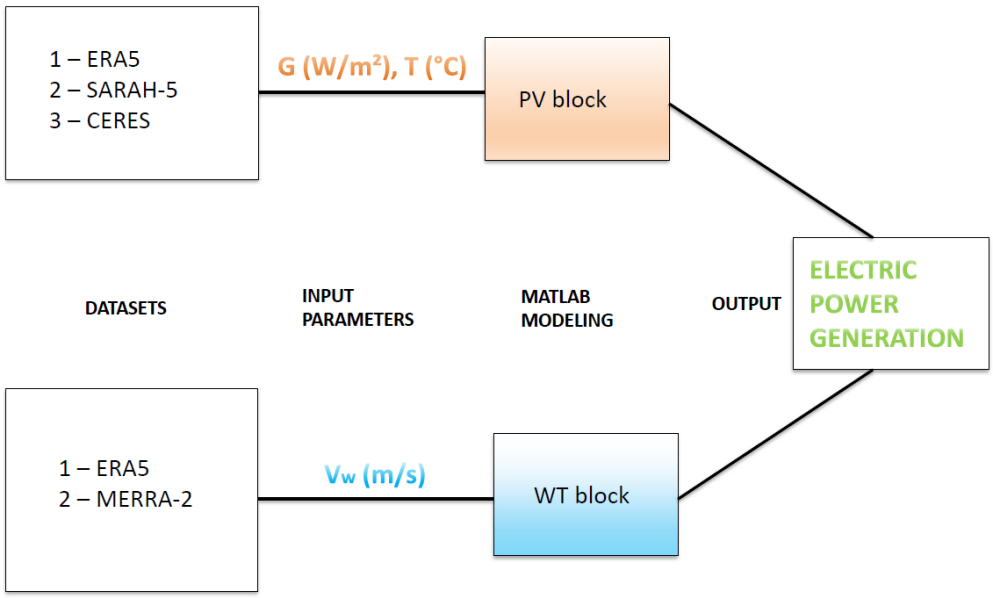

Figure 3.1 – Scheme of databases and parameters for PV and WT power production.

The datasets initially considered were 12, some based on satellite acquisitions, others on real measurements from surface meteorological stations, and others derived from reanalysis or computational and empirical models. The models used are summarized in the following table; however, it is useful to describe the main differences between the most widely used databases globally and those most frequently cited in scientific literature.

Table 3.1 - List of the available databases with their source type and origin.

Database	Primary Data Source Type	Method / Data Origin
ERA-5 (ECMWF)	Modelled (Reanalysis)	Assimilation of satellite and surface measurement in ECMWF model
SARAH-3 (EUMETSAT)	Satellite-based	SEVIRI (Meteosat) satellite data processed to derive solar irradiance
CERES-SYN1deg (NASA)	Satellite-based	CERES (Terra, Aqua, NPP) data combined with clouds and radiative models
MERRA-2 (NASA)	Modelled (Reanalysis)	Assimilation of satellite and surface observations in GEOS-5 model
CFSR / CFSv2 (NOAA)	Modelled (Reanalysis)	Assimilation of observational and satellite data in NCEP model
NEWA (New European Wind Atlas)	Modelled (Mesoscale)	High-resolution WRF simulations validated with ground stations
COSMO-REA6 (DWD)	Modelled (Regional Reanalysis)	Assimilation of observational data in the COSMO regional model (DWD)
Meteonorm	Hybrid (Stations + Empirical Model)	Interpolation of meteorological stations and empirical irradiance models
HelioClim (HC-3, HC-5)	Satellite-based	Meteosat data processed using Heliosat algorithms to estimate solar irradiance
Solargis	Hybrid (Satellite + Model)	Geostationary satellite data with atmospheric and radiative model corrections
SoDa	Data Portal / Aggregator	Integration of multiple datasets (HelioClim, SARAH, ERA5, etc.)
Copernicus (CDS / CAMS)	Modelled + Satellite Assimilation	ECMWF and CAMS services combining modelled and satellite-derived data

Platforms such as ECMWF (European Centre for Medium-Range Weather Forecasts), Copernicus Climate Data Store, and PVGIS (Photovoltaic Geographical Information System) use parameters derived from the ERA-5 database.

ERA-5 is mainly used for energy analyses in the solar field and provides data such as global horizontal irradiance (GHI), direct normal irradiance (DNI), diffuse horizontal irradiance (DHI), air temperature, and air humidity [39]. This database has global geographic coverage with a spatial resolution of about 0.25° (31 km) and temporal coverage from 1950 to today with hourly resolution; moreover, it is an open-access database. The data are obtained by combining satellite measurements

with surface acquisitions through a reanalysis model of spatial data. This makes it particularly suitable for research activities and for the modelling of medium- or large-scale photovoltaic or hybrid plants, while it is less suitable for micro-siting due to the limited spatial resolution.

Another database widely cited in literature is SARAH, currently available up to version SARAH-5 [39]. This dataset covers Europe, Africa, and the Middle East and has a significantly higher spatial resolution than the previous one, about 0.05° (5 km). The temporal resolution is also hourly. The parameters provided include all components of solar irradiance, albedo, daylight duration, air temperature, and humidity. The database is based solely on satellite data from the SEVIRI sensor of Meteosat and, thanks to the high accuracy of the resolution, it is particularly suitable for mapping and providing input for photovoltaic yield calculations.

A third solar dataset, used by NASA POWER, is the CERES-SYN satellite model, which combines information related to terrestrial solar irradiance with the contribution of clouds, when such an option is selected [40]. This dataset has global geographic coverage, with a spatial resolution of 0.5° (55 km), and temporal coverage from 1981 to today, with resolution ranging from daily to hourly.

Considering the advantages associated with these three databases, together with their open-access availability, they were selected as input for the photovoltaic simulation model developed in MATLAB.

Table 3.2 - Suitable databases for PV based on their characteristics and limitations.

PV DATASET					
Dataset	Coverage	Resolution	Time step	Forecast capability	Limitations
ERA5	Global	0.25° (30 km)	Hourly	No - Reanalysis	
SARAH-5	Europe/ Africa	5 km	Hourly	No - Satellite climatology	
CERES SYN1	Global	0.5° (50 km)	Hourly/daily	No - Observational dataset	
Meteonorm	Global	1 - 10 km	Hourly	No - Synthetic data	Not open access

HelioClim	Global	1 - 3 km	15 - 60 min	No - Satellite climatology	Not open access
Solargis	Global	1 km	15 min	No - Satellite + reanalysis	Not open access

For wind parameters to be inserted into the wind turbine (WT) model, in particular for wind speed parameter, two distinct datasets were analysed and described below.

The first is again ERA-5, obtained through the PVGIS portal [39]. The available variables include air density, temperature, and pressure, as well as wind speed and direction at two different heights: 10 m and 100 m. In this case, data assimilation occurs through satellite acquisitions for wind speed, temperature, and humidity above the ocean surface, while for pressure, temperature, wind speed, and vertical profiles in the remaining geographic areas, the data derive from in situ observations carried out by terrestrial meteorological stations.

The second database used as input for the wind model in MATLAB is MERRA-2, provided by NASA POWER [40]. It has global geographic coverage with a spatial resolution of about 0.5° (55 km) and provides hourly data, including wind speed at different heights defined by the user, from 10 m up to 100 m, with default values of 10 m and 50 m.

Table 3.3 - Suitable databases for WT based on their characteristics and limitations.

WIND DATASET					
Dataset	Coverage	Resolution	Time step	Forecast capability	Limitations
ERA-5	Global	0.25° (30 km)	Hourly	No - Reanalysis	
MERRA-2	Global	0.5° (50 km)	Hourly	No - Reanalysis	
CFSR/CFS v2	Global	0.5° (50 km)	6-hour	Yes - Trend forecasting	Time resolution
NEWA	Europe	3 km	Hourly	No - Downscaled reanalysis	Only European data
COSMO-REA6	Europe	6 km	Hourly	No - Regional reanalysis	Only European data

3.2 Graphical comparison of PV parameters from different databases

For the download of the three databases containing solar parameters, the year 2023 was selected, as it represents the latest complete year available on the PVGIS website, from which the ERA-5 and SARAH-3 datasets were obtained. The CERES-SYN data, instead, was downloaded through the NASA POWER portal.

The sites of interest chosen for the comparison of the solar resource in Morocco are the city of Rabat and the city of Ouarzazate: Technopolis area for the former and the Industrial area for the latter. The time interval was defined between January 1, 2023, and December 31, 2023, with hourly resolution, thus obtaining a total of 8760 values.

The analysis was conducted using MATLAB software for panels with different inclinations: horizontal (slope = 0°), optimal (slope = 33° for Rabat and slope = 32° for Ouarzazate), and vertical (slope = 90°). This approach makes it possible to highlight differences both in trends and in peak values. The azimuth considered for the positioning of the solar panel is also optimal, derived from the analysed sites, equal to 5° for Rabat and 10° for Ouarzazate, adopting the convention according to which the south azimuth corresponds to 0°.

For each city, daily and weekly graphs were produced, as to analyse in detail the trend of global irradiance; subsequently annual trend graphs were developed in order to evaluate the similarity of the overall curves derived from the different datasets.

The methodology foresees as a first phase the download of the datasets in csv format. In the case of ERA-5 and SARAH-3 datasets, for each hour of the year the following were selected: direct solar irradiance on the inclined plane expressed as DNI (Direct Normal Irradiance), diffuse irradiance on the horizontal plane expressed as DHI (Diffuse Horizontal Irradiance), the reflected component, solar altitude expressed in degrees, and air temperature at 2 meters height.

For the CERES-SYN1 dataset, instead, for each hour of the year the parameters selected were: All Sky Surface Shortwave Downward Irradiance, Clear Sky Surface Shortwave Downward Irradiance, All Sky Surface Shortwave Downward Direct Normal Irradiance (DNI), All Sky Surface Shortwave Diffuse Irradiance (DHI), surface albedo, solar zenith angle, and air temperature at 2 meters.

A relevant difference between the databases concerns the fact that from the NASA POWER website it is not possible to download data referring to a specific panel angle: they are in fact provided exclusively for a horizontal panel. Consequently, the outputs related to the panel with optimal inclination and to the vertical one do not derive directly from the satellite but are obtained through equations implemented in MATLAB.

The program proceeds by importing the .csv files into a MATLAB table and saving them locally. Subsequently, the columns of the parameters described above are extracted, assigning them their specific names, thus obtaining vectors of dimensions 1×8760. In the following sections, the equations adopted for the different analysed cases are presented together with the respective graphs obtained.

3.2.1 Plot of auxiliary parameters

In this Section are presented the graphical plots of some meteorological parameters in the cities of Rabat and Ouarzazate. These parameters are not directly involved in the study of photovoltaic and wind power plants, however, they are used indirectly or through data manipulation, to calculate the power output generated by these systems.

It is therefore considered essential to present their trends over two days of the year: 21 June 2023 and 21 December 2023, summer and winter solstices respectively. It was decided to plot only the daily profiles, rather than those over longer time horizons such as weekly periods, since the trends appear regular and are almost identically repeated for each day within the corresponding week.

Moreover, given the relatively small discrepancies among the considered datasets ERA-5, SARAH-3 and NASA, they are more clearly identifiable in the hourly-resolved daily profiles**,** where even limited deviations become more evident.

The parameters considered and reported here are temperature, solar zenith angle and solar altitude.

RABAT

TEMPERATURE

A focus on air temperature was chosen for the study of the operation of photovoltaic panels, because this parameter is closely correlated with panel efficiency and with the amount of energy absorbed by them. The temperature of photovoltaic cells is one of the most critical parameters, as it directly influences the current-voltage characteristic curve of the device.

The cell temperature is, in turn, correlated with the air temperature T_a and with the energy balance of the module through the thermal equilibrium model:

$$T_c = T_a + \frac{G}{U}(1-\eta) \qquad 3.1$$

with:

- T_c: photovoltaic cell temperature
- T_a: air temperature
- G: incident global irradiance
- U: overall convective-radiative heat transfer coefficient
- η: electrical efficiency of the module

In this study, the temporal trend of the air temperature is obtained at a height of 2 m from the three databases ERA-5, SARAH-3, and NASA. In particular, this Section presents the results for the summer and winter solstices in the city of Rabat.

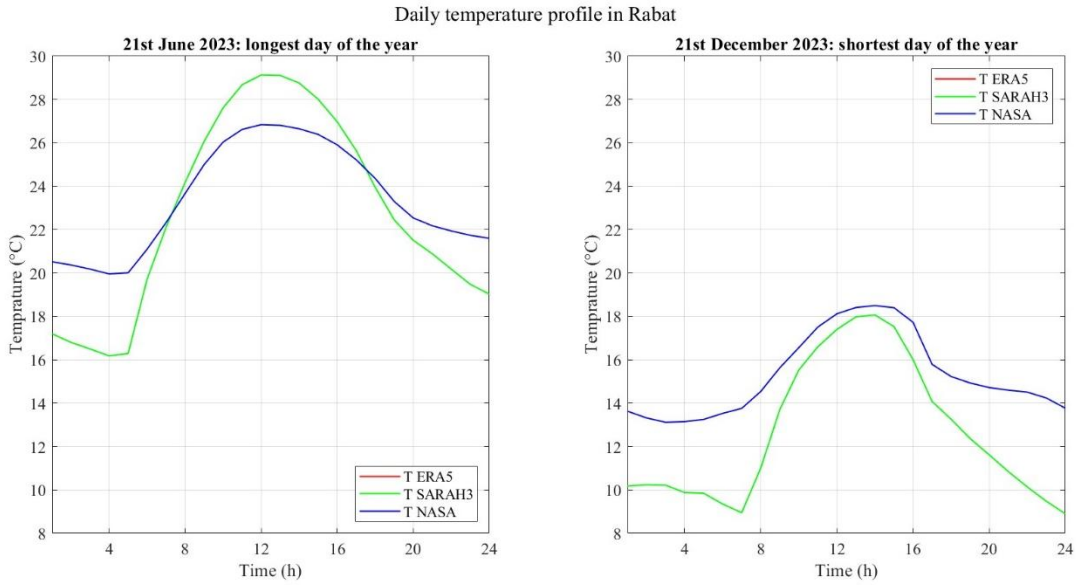

Figure 3.2 - Graphical plot of daily temperature profile in Rabat.

It is evident that, for the two databases provided by the PVGIS platform, ERA-5 and SARAH-3, the temperature curves are perfectly overlapping. This can be attributed to their common dependence on ECMWF reanalysis. ERA-5 is in fact a global reanalysis produced by ECMWF through the Integrated Forecasting System (IFS) data assimilation system, which combines observations from ground stations, radiosondes, satellites, and physically consistent models [41]. SARAH-3, on the other hand, uses auxiliary meteorological fields derived from ECMWF reanalysis, in particular air temperature, pressure, and atmospheric profiles [42].

Given that SARAH-3 is a radiative dataset rather than thermodynamic, air temperature in this case is not a primary variable of the dataset, but rather an auxiliary parameter and it retains a temporal structure and amplitude remarkably similar to those of ERA-5, without the application of substantial post-processing. The resulting differences are smaller than the typical uncertainty associated with reanalysis data.

The NASA database, instead, exhibits a trend that deviates from those of the other two datasets, as it relies on a different assimilation system (GEOS), different surface schemes and parameterizations, and a coarser spatial resolution, as highlighted in Section 3.1.

Focusing on the profiles for 21 June 2023, ERA-5 and SARAH-3 start at 00:00 until 04:00 with a minimum temperature of 16.1 °C, then rapidly increase their slope in the following hours, reaching a peak of 29 °C at 13:00. From 14:00 until midnight, the temperature begins to decrease, reaching a minimum value of 19.2 °C. For these databases, the trend clearly exhibits a bell-shaped profile, similar to that of global solar irradiance, and is therefore consistent with daylight hours.

For the NASA database, the trend is not perfectly bell-shaped but rather more irregular. It begins in the early morning hours with a higher temperature than the other two curves, equal to 20 °C, then increases its slope without reaching a peak comparable to those of the previous databases, stopping at 26.8 °C and decreasing immediately thereafter.

The trend of the curve for 21 December 2023 highlights the reduced daylight hours compared to the summer solstice, resulting in a much narrower bell-shaped curve. The minimum temperature of the ERA-5 and SARAH-3 curves corresponds to 10.1 °C, while that of the NASA curve corresponds to 13.6 °C; subsequently, both curves increase to respective peaks of 18.0 °C and 18.2 °C. In this case, there are no intersections between the curves, and the NASA curve remains higher for all values throughout the day.

SOLAR ZENITH ANGLE

The solar zenith angle is defined as the angle between the solar beam and the normal to the Earth's surface. The analysis of solar zenith angle graphs was chosen because it is considered a fundamental parameter, correlated with the irradiance incident on an inclined panel through its cosine and the cosine of the angle of incidence.

The following formulas are defined:

$$G_t = G_b \cos(\theta_i) + G_d\, F_d + G_r\, F_r \qquad 3.2$$

with:

- G_t= solar irradiance on the tilted surface of the panel
- G_b= solar beam irradiance (direct irradiance).
- θ_i= angle of incidence between the solar rays and the normal to the module plane
- G_d = solar diffuse irradiance
- F_d= transposition factor of the diffuse component
- G_r = solar reflected irradiance

- F_r= transposition factor of the reflected component

and

$$cos\theta_i = cos\theta_z cos\beta + sin\theta_z sin\beta \cos(\phi_s - \gamma) \quad 3.3$$

- θ_i = angle of incidence
- θ_z= solar zenith angle
- β= tilt angle of the surface relative to the horizontal
- ϕ_s= solar azimuth
- γ= surface azimuth.

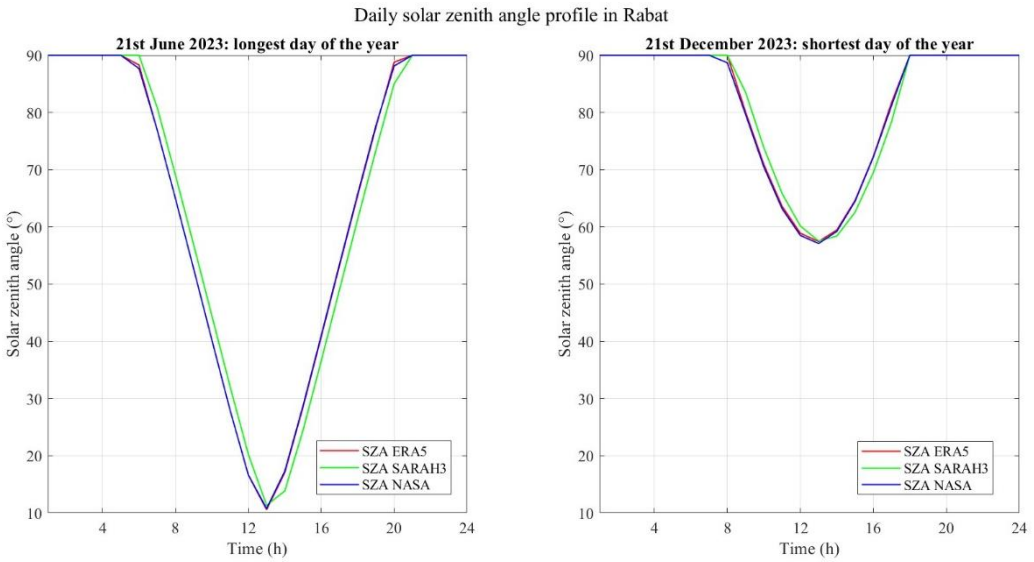

Figure 3.3 - Graphical plot of daily solar zenith angle profile in Rabat.

In the graphs presented, the solar angles typical of the two solstices, summer and winter, are analyzed; in this case, the values for the city of Rabat are shown. For 21 June 2023, the graph extends on the vertical axis from 10° to 90°, displaying an inverted bell-shaped trend that is very regular, remaining constant at 90° until 05:00 and again from 20:00. The three curves are distinct, with none overlapping, though they are nearly indistinguishable, differing only by a few tenths of a degree.

For 21 December 2023, the winter solstice, the trend is very similar to the previous graph; the inverted bell shape is narrower and more rounded, and values different from 90° appear between 08:00 and 16:00. The minimum value is 57°, compared to 10° in the previous graph.

This difference can be explained by the dependence of the zenith angle on the solar hour angle and the solar declination, through the formula:

$$cos\theta_z = sin\phi sin\delta + cos\phi cos\delta cos(h) \quad 3.4$$

with:

- θ_z= solar zenith angle
- ϕ = latitude of the location
- δ = solar declination (maximum +23.5° on 21 June, minimum −23.5° on 21 December)
- h = solar hour angle (measuring how far the Sun has moved relative to the local meridian)

In June, the Sun culminates near the zenith, so the solar zenith angle (SZA) can decrease significantly because the solar declination is maximally positive.

In December, however, the solar declination is maximally negative, so the Sun does not rise high in the sky; the minimum SZA is therefore much higher, the Sun appears lower on the horizon, and the zenith angle does not decrease to very small values.

SOLAR ALTITUDE

The solar altitude is defined as $h_s = 90° - \theta_z$. This parameter is considered fundamental, as it provides a graphical and visual indication of the apparent height of the Sun in the sky. Higher values of h_s correspond to lower values of θ_z, favoring a more normal incidence of solar rays and reducing optical losses due to surface reflection.

Solar geometry also influences the optical path length of irradiance through the atmosphere and, consequently, the spectral composition of the incident irradiance, with well-known effects on the spectral response of photovoltaic materials.

The solar altitude is derived from the different databases depending on whether they provide the solar zenith angle (as in the case of ERA-5 and SARAH-3) or directly the solar altitude h (as in the case of the NASA database).

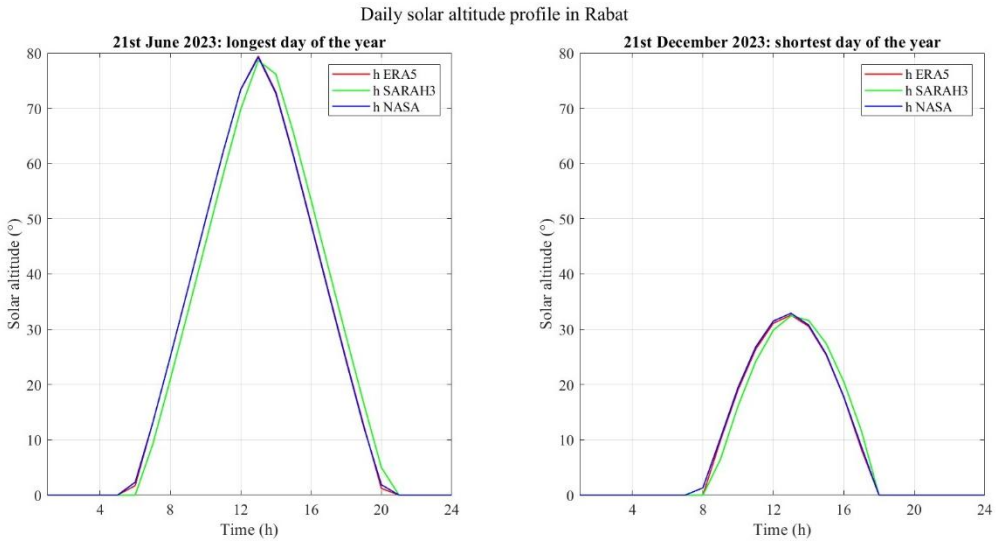

Figure 3.4 - Graphical plot of daily solar altitude profile in Rabat.

In the case of the city of Rabat, for 21 June 2023, the solar altitude ranges from 0° to 80°, starting to increase at 05:00, reaching its peak at 12:00, and then decreasing until it returns to 0° at 20:00.

For 21 December 2023, the solar altitude ranges from 0° (until 07:00) to a peak of 33°, which represents the maximum value for the winter solstice, when the Sun never reaches the zenith and remains lower in the sky.

The trends obtained from the three databases are comparable and mutually consistent. Only ERA-5 shows some inaccuracies when the solar altitude begins to deviate from zero, initially assuming slightly negative values before becoming positive; this behaviour can be attributed to system or acquisition errors rather than to an actual negative value of h_s and so corrected in the presented plot.

OUARZAZATE

TEMPERATURE

Also for the Ouarzazate curves, as observed for the city of Rabat, the ERA5 and SARAH-3 temperature profiles are perfectly overlapping, for the reasons discussed in the previous paragraphs.

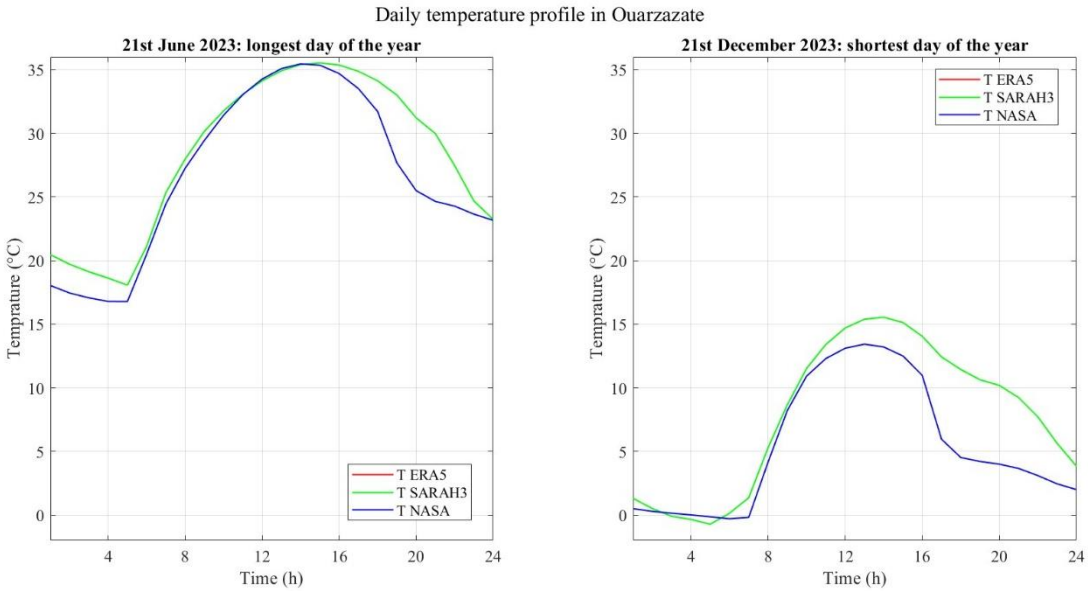

Figure 3.5 - Graphical plot of daily temperature profile in Ouarzazate.

For the day 21 June 2023, the trend of these two curves with respect to the NASA dataset is much more similar than in the case of Rabat, and the profiles appear almost superimposable up to the peak temperature of 35.7 °C reached at 14:00.

Temperatures are higher than those recorded in Rabat, since Ouarzazate is a city located within a desert environment, where the minimum temperature for this day was 16.8 °C for the NASA database and 18.0 °C for the ERA5 and SARAH-3 databases.

For the day 21 December 2023, the bell-shaped curve is much narrower, but the temperature trends of the three databases are comparable. The NASA curve remains lower than those of ERA-5 and SARAH-3; however, all three start from nearly constant values around 0 °C, occasionally reaching negative values.

Over the course of the day, the temperature increases up to 13.2 °C for the NASA database and 15.8 °C for the ERA-5 and SARAH-3 databases, resulting in a diurnal temperature range of approximately 16 °C. The curves then decrease after 14:00, reaching minimum values of about 4 °C for ERA-5 and SARAH-3 and 2 °C for NASA.

SOLAR ZENITH ANGLE

For the city of Ouarzazate, all the observations previously made regarding the solar zenith angle are applied: the correlation with the angle of incidence, with the solar irradiance on the inclined plane, and with the various fundamental solar angles, as well as how the minimum SZA value varies in the graphs for the summer and winter solstices.

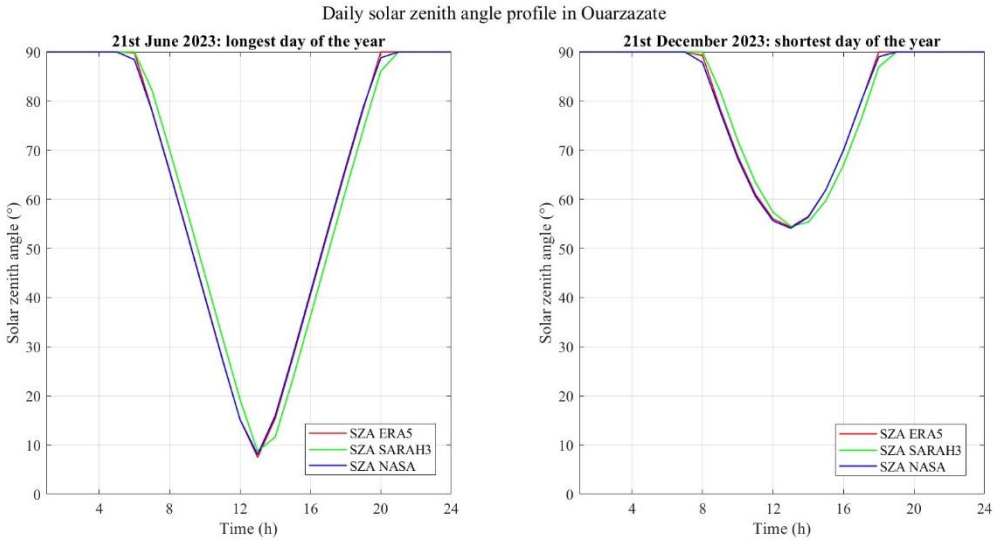

Figure 3.6 - Graphical plot of daily solar zenith angle profile in Ouarzazate.

On 21 June 2023, the solar zenith angle remains at 90° until 06:00 and decreases to a minimum of 9° at 12:00, rising again to reach 90° at 20:00.

On 21 December 2023, the solar zenith angle remains constant at 90° until 08:00, then decreases to a minimum of 54° at noon, and rises again to 90° by 18:00.

It is observed that, among the three curves ERA-5, SARAH-3 and NASA, both the trends and the values of this parameter are identical, although not perfectly overlapping. This allows all three curves to be distinguishable, while the differences between them are negligible.

SOLAR ALTITUDE

For the city of Ouarzazate, the solar altitude graphs are very similar to those of Rabat, with the only difference being that, during the summer solstice, the values range from 0° to 82°, reaching the peak at 13:00 and forming a profile with an almost linear increasing and decreasing slope for all three databases.

For the winter solstice, the curve starts to assume values different from zero at 07:00, reaches a peak not exceeding 36°, and then decreases again to zero at 19:00, resulting in a narrower bell-shaped profile.

Also in this case, the values and trends provided by the three databases differ by negligible amounts.

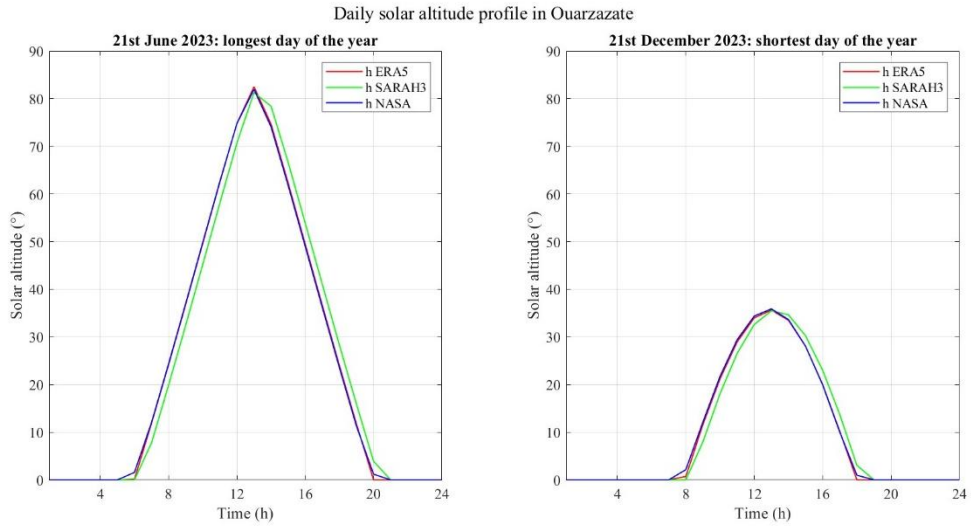

Figure 3.7- Graphical plot of daily solar altitude profile Ouarzazate.

3.2.2 Analysis of a horizontal panel

In this Section, the global irradiance parameters are analysed for the cities of Rabat and Ouarzazate. For Rabat, the panel azimuth angle is 5° and the tilt angle is 0°. For Ouarzazate, the panel azimuth angle is 10° and the tilt angle is 0°.

RABAT

In the case of a horizontal panel, the equations to be used for the calculation of the global irradiance component do not include the reflected irradiance. The irradiance on the panel plane (POA) corresponds to the global irradiance on the horizontal plane and, depending on the components provided by each database, these equations are different.

For ERA-5 and SARAH-3:

$$POA = GHI = Gb + Gd \qquad 3.5$$

For CERES-SYN:

$$POA = GHI = DNI \cdot \cos(\theta z) + DHI \quad 3.6$$

with $\theta_z = 90° - h$ ($sun\ height\ h$).

The results obtained by following this method for the city of Rabat are shown in the figures below.

The trends of daily global irradiance in Rabat on 21 June 21 and 21 December 2023 are analysed. The first curve has a wide and symmetrical profile, with peaks around 1000 W/m² and a duration of about 14 hours of daylight. During the winter solstice, instead, the curve is much more contained, with a maximum around 400 - 500 W/m² and a sunlight window reduced to about 9 hours. Here too, the differences between the datasets are mainly noticeable in regularity: NASA shows a more uniform trend, SARAH-3 more variability, and ERA-5 slightly lower peak values and an irregular trend.

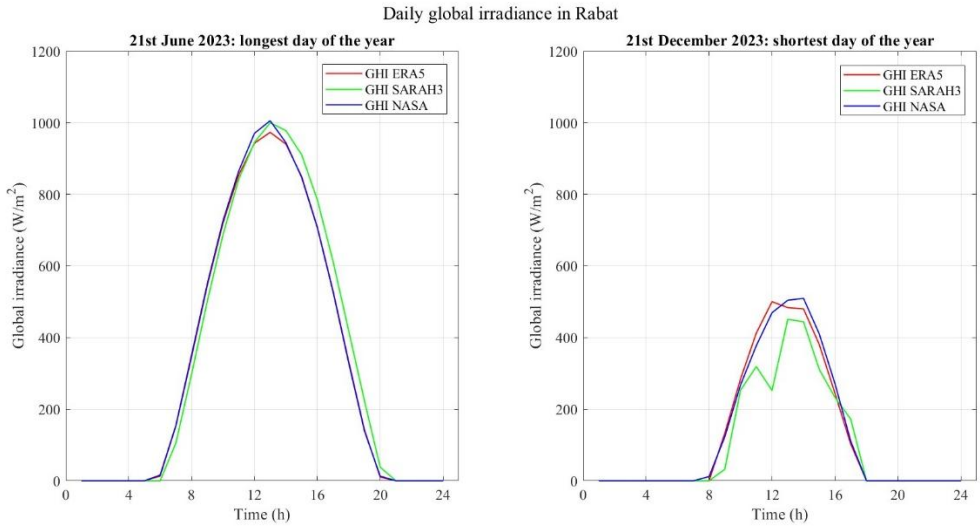

Figure 3.8 - Graphical plot of daily global irradiance in Rabat on a horizontal panel.

Subsequently, it is represented the trend of solar irradiance in two distinct time intervals: the first corresponding to the week of the summer solstice, characterized by the maximum annual availability of daylight hours, and the second relating to the week of the winter solstice, during which the availability of sunlight is minimal. This comparison makes it possible to clearly highlight the differences between the two periods and between the different databases.

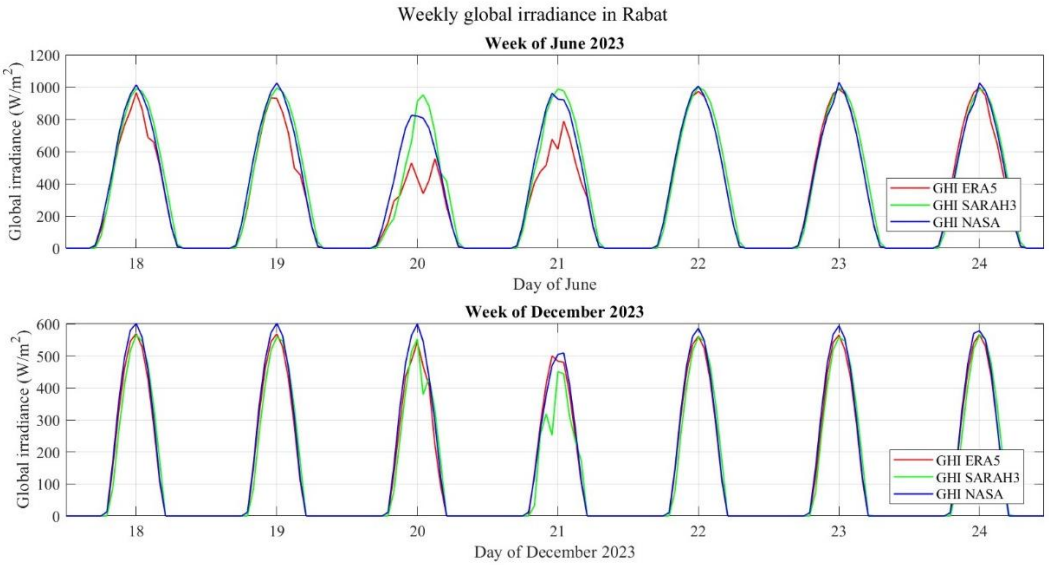

Figure 3.9 - Weekly global irradiance in Rabat on a horizontal panel.

In the weekly graphs of Rabat, the week of June shows a very regular daily cycle, with peaks between 900 and 1000 W/m² and long days. The week of December instead shows lower values, with maximums around 600 W/m² and shorter days. ERA-5 tends to smooth the peaks compared to NASA, while SARAH-3 shows greater hourly variability.

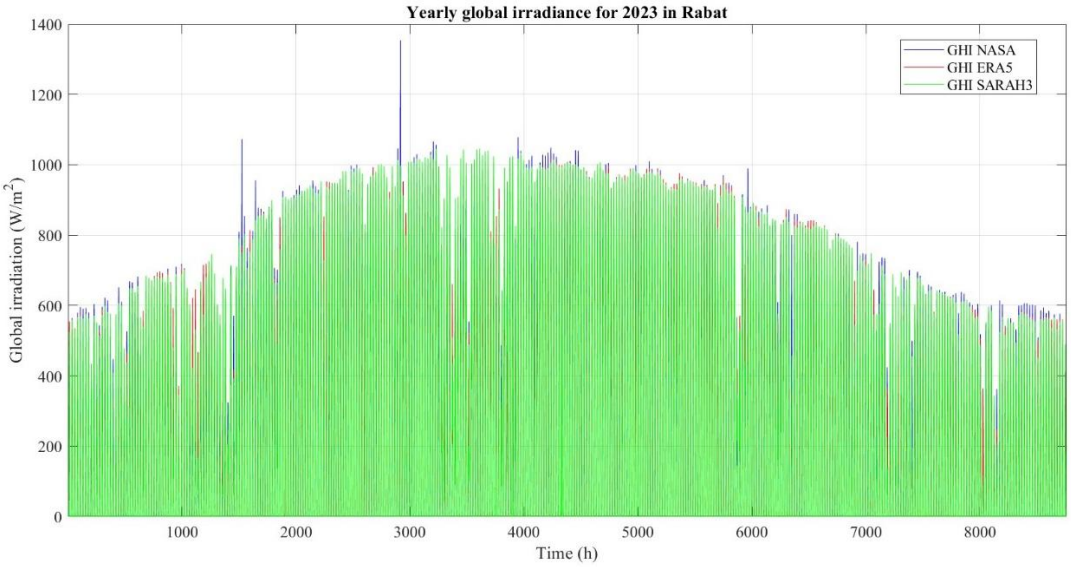

Figure 3.10 - Yearly global irradiance in Rabat on a horizontal panel.

Finally, in the annual graph of global irradiance, a typically seasonal trend can be observed, with minimum values in the winter months and maximum values in the summer months. The lowest values are recorded between January and December, corresponding to the first and last 800 hours of the year, where irradiance drops below 600 W/m². The peak is located between hours 4300 and 4500, which correspond to June and July, with values reaching about 1010 W/m² on the most irradiated days.

OUARZAZATE

The equations used for the city of Ouarzazate are those previously described for Rabat, using the specific solar altitudes for the new location. Therefore, in this section only the graphical results and their respective descriptions are shown.

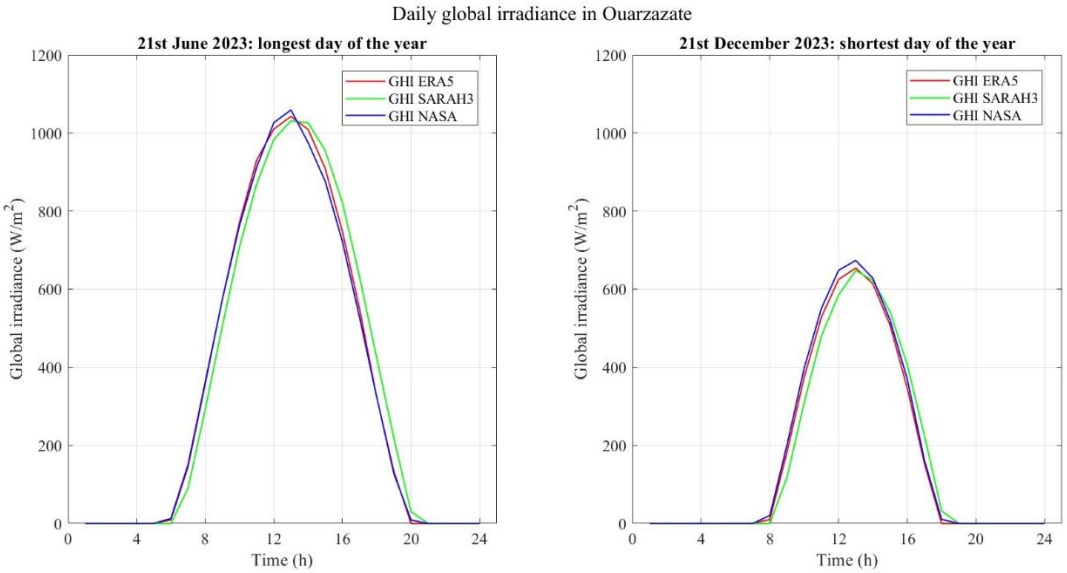

Figure 3.11 - Graphical plot of daily GHI profile in Ouarzazate.

In the daily graphs of Ouarzazate, the difference between the summer solstice and the winter solstice is clearly visible. On June 21, the global irradiance curve has a wide and regular trend, with values rising rapidly in the morning, reaching a peak close to 1000 W/m² around noon, and slowly decreasing in the afternoon. On December 21, instead, the curve is much narrower and lower, with a maximum not exceeding 700 W/m², but still higher than those of the city of Rabat, thanks to the site's desert location.

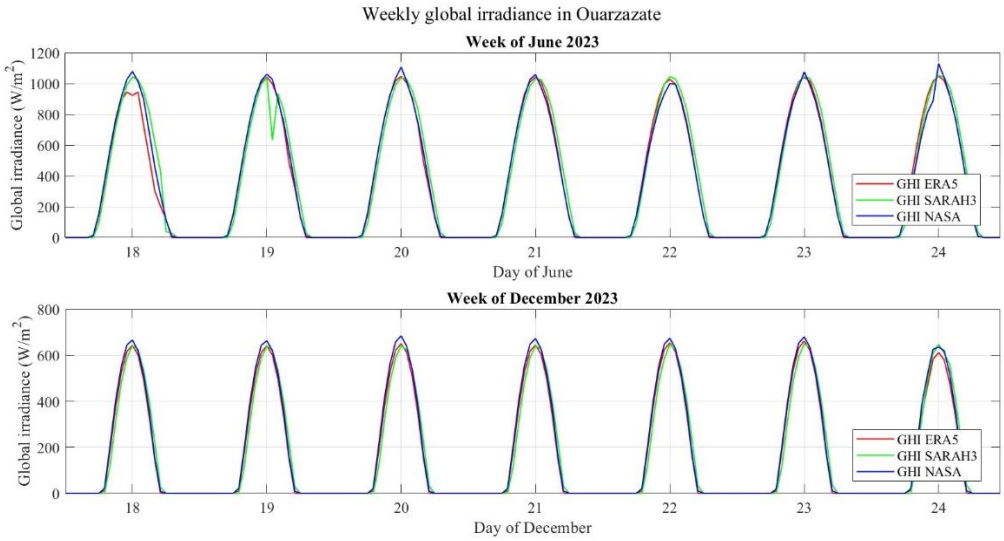

Figure 3.12 - Graphical plot of weekly GHI profile in Ouarzazate.

In the weekly graphs of Ouarzazate, the week of June highlights a sequence of days with regular and very high peaks, exceeding 1000 W/m² and repeating daily with a bell-shaped trend. The week of December instead shows lower peaks, around 600 - 700 W/m², still higher values than those of Rabat thanks to the desert location of the site.

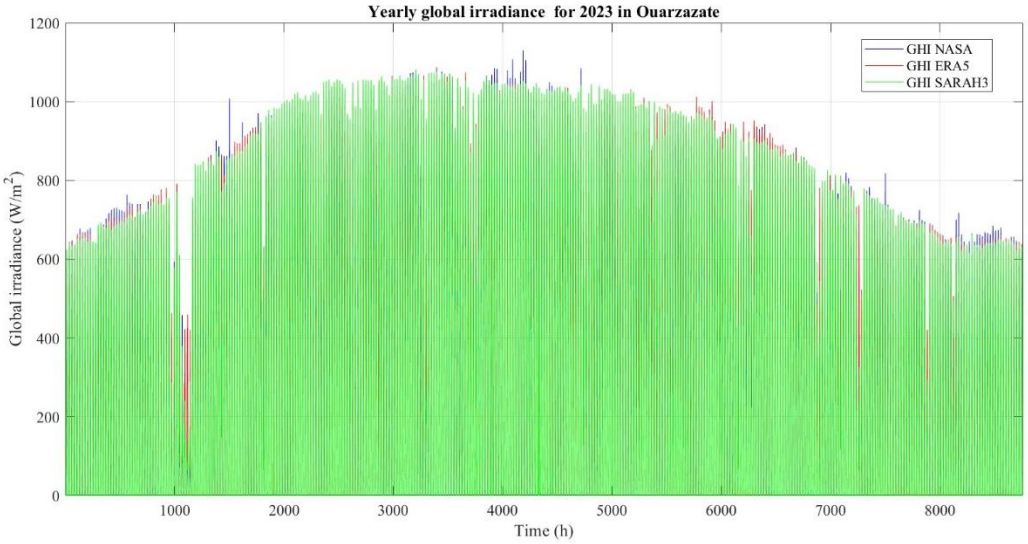

Figure 3.13 - Graphical plot of yearly GHI profile in Ouarzazate.

In the annual global irradiance graph of Ouarzazate, the trend is similar to that of Rabat but with generally higher values thanks to the inland position and clearer skies. Here too, the peak occurs between June and July, around hours 4300 - 4500,

with values exceeding 1050 W/m². The winter minimums are still above 600 W/m², between the initial and final hours of the year.

3.2.3 Analysis of an optimal angle panel

To obtain the trend of global irradiance on an inclined plane, it is first necessary to determine the optimal tilt angle; in the case of the PVGIS portal, this value is automatically calculated and provided. For the city of Rabat, the optimal tilt angle is 33°, which coincides with the city's latitude, while the azimuth angle remains 5°. For the city of Ouarzazate, the optimal tilt angle is 32°, with an azimuth angle of 10°.

RABAT

DATABASE VALUES

In this section, the values obtained directly by downloading the SARAH-3 and ERA-5 databases are compared with the results of the equations already implemented in the model, which allow the computation of irradiance for any desired inclination.

In the case of the inclined plane, the component of irradiance reflected from the ground is also included to obtain the irradiance on the plane.

For these two databases, the components provided by the dataset are simply summed:

$$POA = Gb, tilt + Gd, tilt + Gr, tilt \tag{3.7}$$

For the NASA database, instead, it is necessary to derive the irradiance component on the inclined plane starting from the values provided exclusively for the horizontal plane. Consequently, the direct, diffuse, and reflected components on the inclined plane are obtained by applying specific geometric and radiometric transformations. The formulas implemented in MATLAB to perform this conversion are the following:

$$POA = DNI \cdot \cos(\theta i) + DHI\left(1 + \frac{\cos(\beta)}{2}\right) + GHI \cdot \rho g \cdot 1 - \frac{\cos(\beta)}{2} \tag{3.8}$$

$$\cos(\theta i) = \sin(h)\ \cos(\beta) + \cos(h)\ \sin(\beta)\ \cos(\gamma s - \gamma) \tag{3.9}$$

where:

- h: solar altitude
- β: tilt angle of the panel plane
- γ_s: solar azimuth
- γ: panel azimuth
- GHI: global component on horizontal (direct projected + diffuse)
- P_g: ground albedo, provided with hourly resolution by the NASA database.

If the daily curve is considered, it can be noted that NASA stands out for its more uniform curve, while ERA-5 and SARAH-5 show slight variations in the peaks. The curves become more irregular and the differences between the models become more evident: SARAH-5 tends to underestimate, ERA-5 shows greater variability, and NASA remains more stable. June 21 shows a curve with peaks between 900 and 1000 W/m². On December 21, the curve shows a peak around 800 W/m².

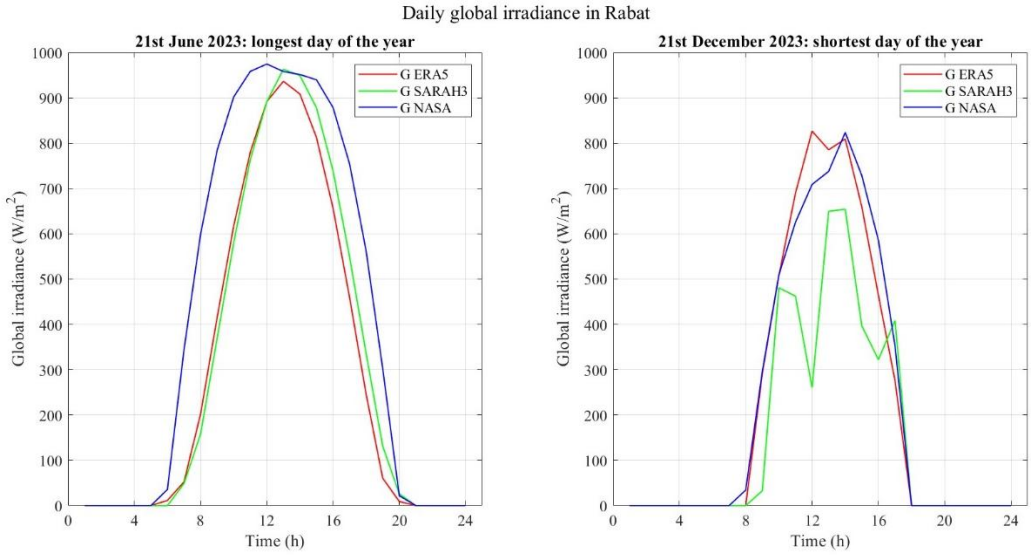

Figure 3.14 – Daily global irradiance in Rabat on an optimal angle tilted panel, with database values.

The following graph shows instead the weekly trend of the global irradiance component in the city of Rabat. For the month of June, the trend includes daily peaks between 900 and 1000 W/m² and good regularity, although for some of the days considered there is a large gap between one database and another, with a maximum of 500 W/m² for ERA-5 and 900 W/m² for NASA on the same day. In the week of December, the values do not decrease significantly, but remain fairly regular, with maximums around 900 - 1000 W/m².

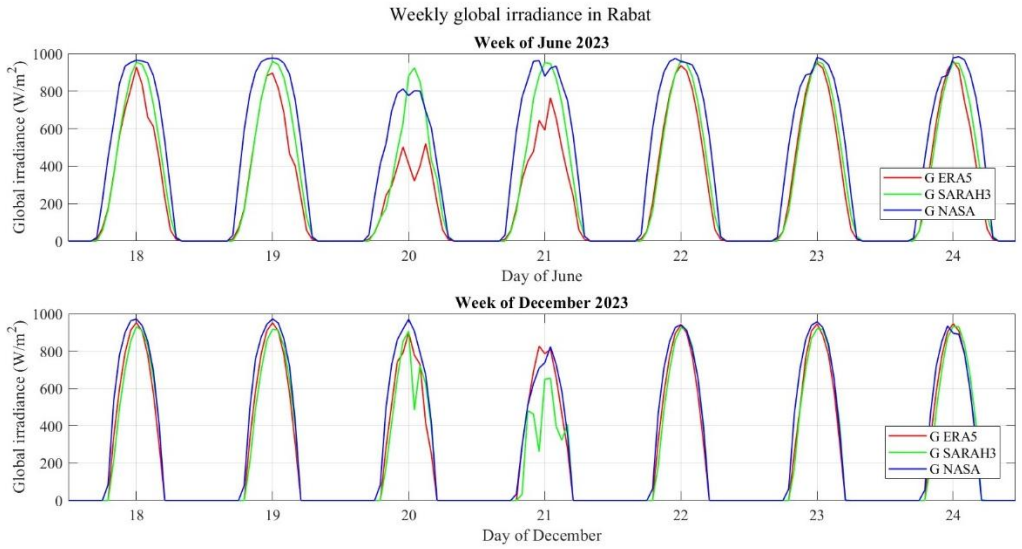

Figure 3.15 - Weekly global irradiance in Rabat on an optimal angle tilted panel, with database values.

The graphical results obtained for the annual trend are more regular compared to those of the horizontal panel analysed previously; in fact, no marked seasonal trend is observed, but rather an almost uniform profile throughout the year, since the panel with optimal inclination maximizes the capture of solar irradiance in all seasons.

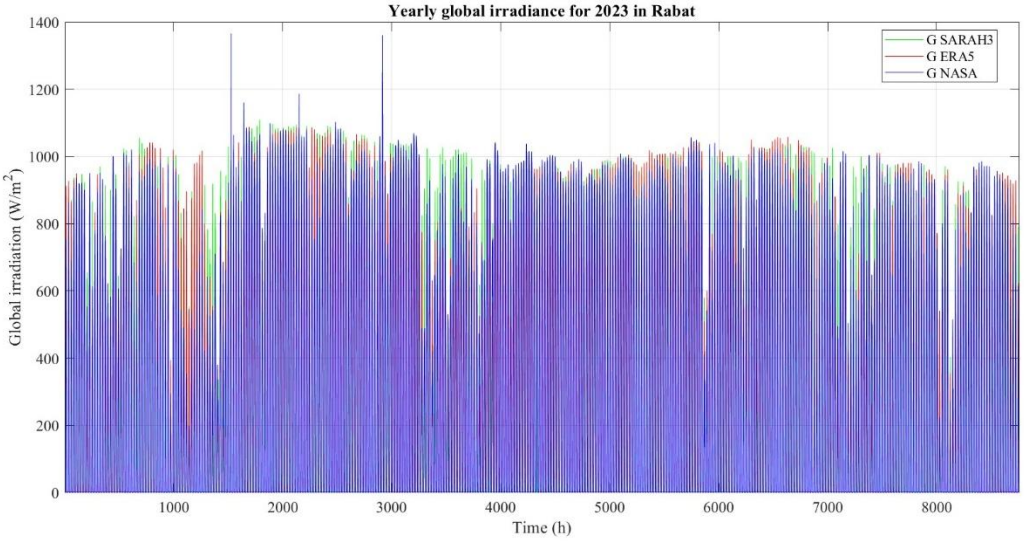

Figure 3.16 - Graphical plot of yearly global irradiance in Rabat on an optimal angle tilted panel, with database values.

CALCULATED VALUES

In this section, the results relating to the trend of global solar irradiance incident on a panel with optimal inclination are analysed. The difference compared to the previous paragraph lies in the way the data were obtained. In this case, in fact, not only for the NASA dataset were the values of irradiance incident on the horizontal plane reprocessed to derive those on the inclined plane, but the same procedure was also applied to the ERA-5 and SARAH-3 datasets . This choice makes it possible to ensure greater consistency among the graphs generated from the three different inputs and to highlight the differences compared to the previously analysed case.

The formulas used for all three databases are the following:

$$POA = DNI \cdot \cos(\theta i) + DHI \cdot 1 + \frac{\cos(\beta)}{2} + GHI \cdot \rho g \cdot 1 - \frac{\cos(\beta)}{2} \quad 3.10$$

$$\cos(\theta i) = \sin(h)\ \cos(\beta) + \cos(h)\ \sin(\beta)\ \cos(\gamma s - \gamma) \quad 3.11$$

where:

- h: solar altitude
- β: tilt angle of the panel plane
- γ_s: solar azimuth
- γ: panel azimuth
- GHI: global component on horizontal (direct projected + diffuse)
- ρ_g: ground albedo, provided with hourly resolution by the NASA database and considered fixed and equal to 0.2 for the SARAH-3 and ERA-5 databases.

Below is the result relating to global solar irradiance incident on a plane inclined at 33° in the site of Rabat.

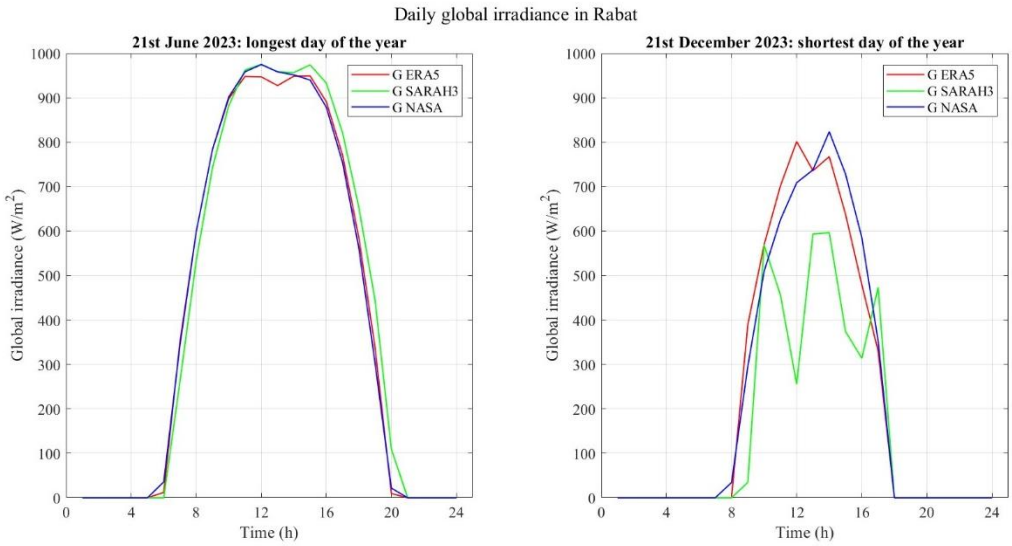

Figure 3.17 – Daily global irradiance in Rabat on an optimal angle tilted panel, with calculated values.

It is from the daily trend that more details on irradiance behaviour and differences among the datasets can be observed. In Rabat, on the day of the summer solstice, global irradiance shows a regular trend with a peak around 980 W/m².

The three databases present similar and uniform curves, which can be explained by considering the uniformity of the solar source itself, being a summer day in a low-cloud area. The day is characterized by a clear profile, with a rapid increase in the morning and a symmetrical decrease in the afternoon. On the winter solstice, direct irradiance decreases significantly, as do the daylight hours and therefore the width of the bell-shaped curve. Peak values range between 600 and 800 W/m², showing clear differences among the datasets.

For SARAH-3, the curve is fragmented and shows minimums reaching 300 W/m²; the trend is more detailed and variable during the day, but this is due to systematic errors in data acquisition and not to shading, since the dataset is satellite-based. NASA and ERA-5 appear less variable but still less uniform compared to the June curves.

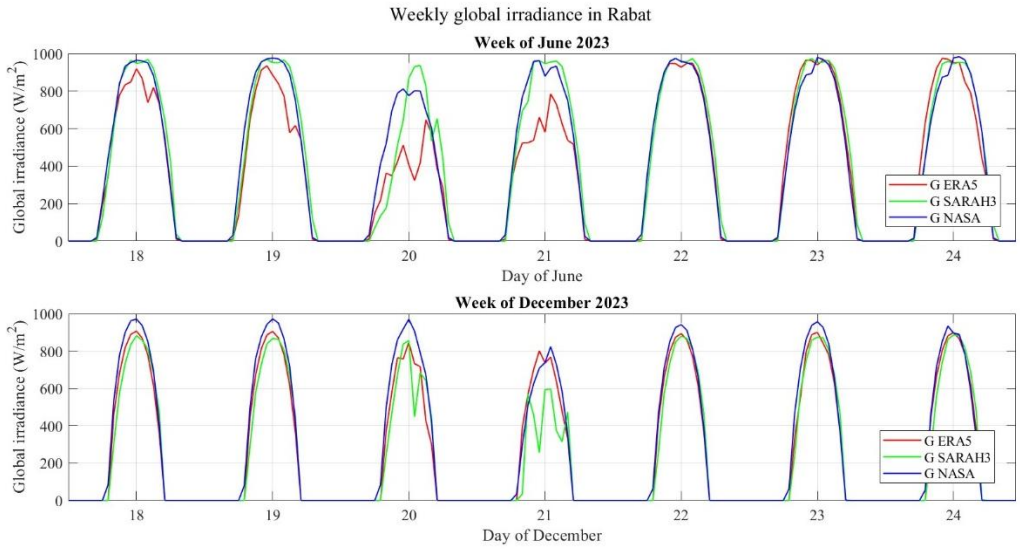

Figure 3.18 - Weekly global irradiance in Rabat on an optimal angle tilted panel, with calculated values.

Considering the weekly trend in the city of Rabat, it is observed that during the week of June, daily values reach peaks between 900 and 1000 W/m². The curves show some variability among the datasets, with ERA-5 tending to underestimate irradiance values compared to NASA and SARAH-3. The overall trend is regular, but with more marked differences among the sources; the ERA-5 dataset in fact presents a broken curve, explainable by the reanalysis that the PVGIS software performs to provide satellite data recombined with observations from surface meteorological stations. In the week of December, peak values remain high, almost constant around 900 W/m², and reach higher values for the NASA dataset, based on purely satellite observations.

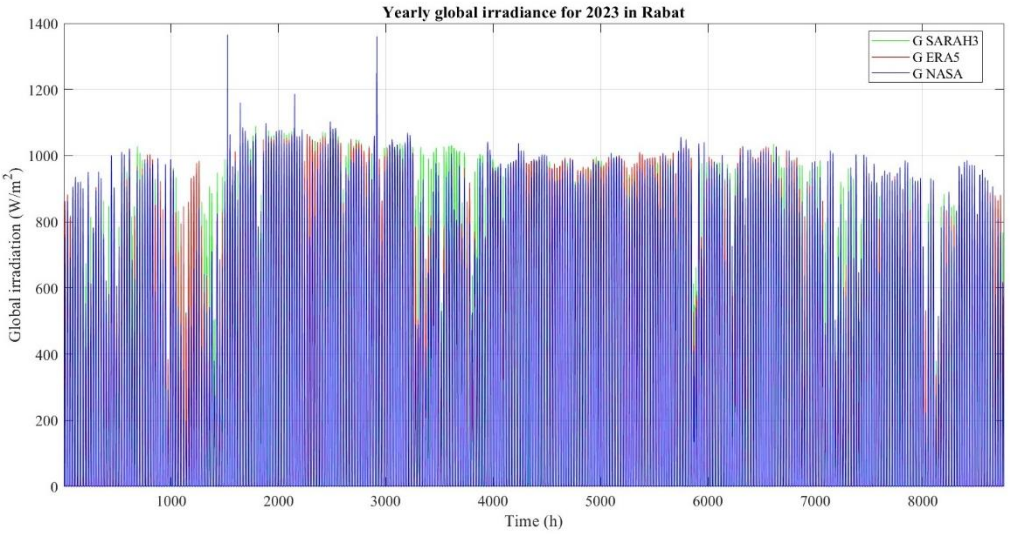

Figure 3.19 - Yearly global irradiance profile in Rabat on an optimal angle tilted panel, with calculated values.

Finally, the annual graph shows peaks exceeding 1000 W/m². The curves of the three datasets partially overlap, but with significant differences: SARAH-3 and ERA-5 show more marked and detailed oscillations, especially in the range from hours 900 to 1300 of the year, corresponding to the months from February to March. NASA tends to underestimate the maximum values overall, although it presents peaks exceeding 1380 W/m². Variability is accentuated, with dispersion among the datasets especially in the winter months, but the overall trend is not bell-shaped but rather uniform throughout the analysed period, since with optimal inclination the incident irradiance is optimized not only in the sunniest months.

OUARZAZATE

DATABASE VALUES

As in the case of Rabat, also for Ouarzazate the values provided directly on the inclined plane are those of the ERA-5 and SARAH-3 datasets only, while for the NASA database, the values are obtained from the previously described formulas.

In the daily graphs relating to Ouarzazate, it is possible to appreciate even more clearly the uniform trend of the curves, free of significant irregularities and characterized by peaks close to 1000 W/m² both in the summer solstice and in the winter solstice, with an almost perfect overlap among the models.

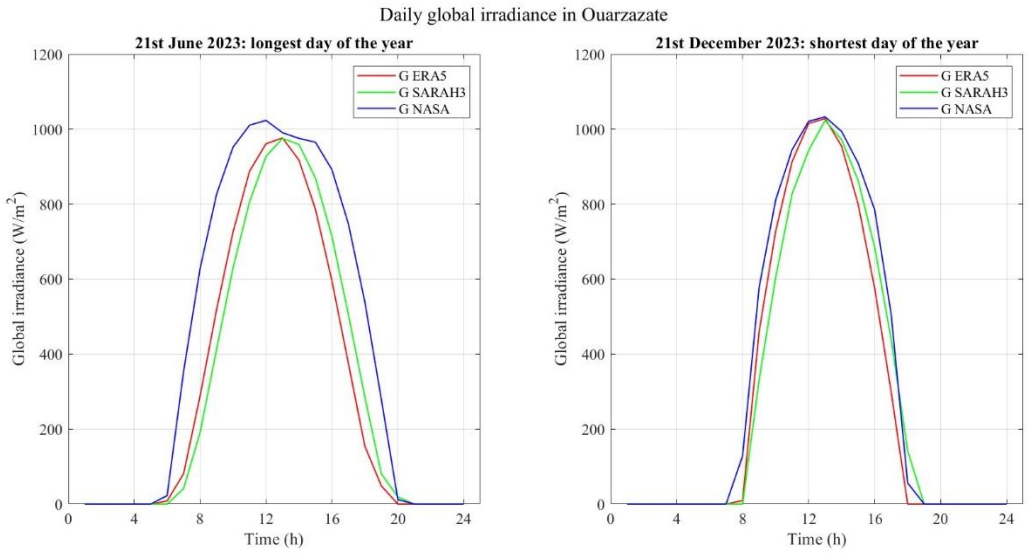

Figure 3.20 - Daily global irradiance profile in Ouarzazate on an optimal angle tilted panel, with database values.

In the weekly graphs shown later, both in the week of June and in that of December, the daily curves repeat with great regularity. Summer peaks remain around 1000 W/m² for all three databases, but even the winter ones are around 1000 W/m². NASA shows greater uniformity, while ERA-5 and SARAH-3 present slight oscillations in peak values, without altering the general shape.

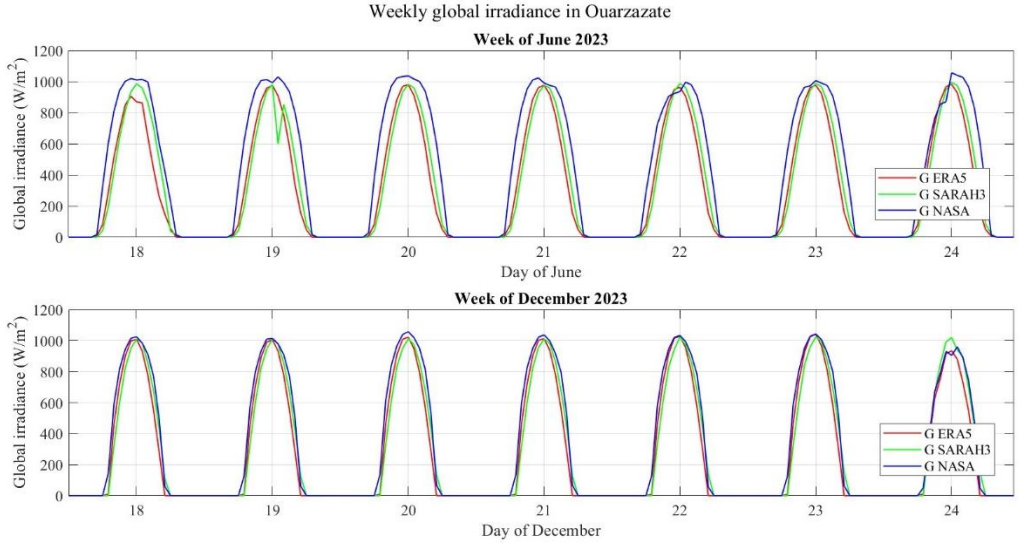

Figure 3.21 - Weekly global irradiance profile in Ouarzazate on an optimal angle tilted panel, with database values.

In this case too, for the graphical plot of the entire year, no signs of atmospheric instability or seasonal discontinuities emerge, but rather a regular repetition of daily and weekly profiles.

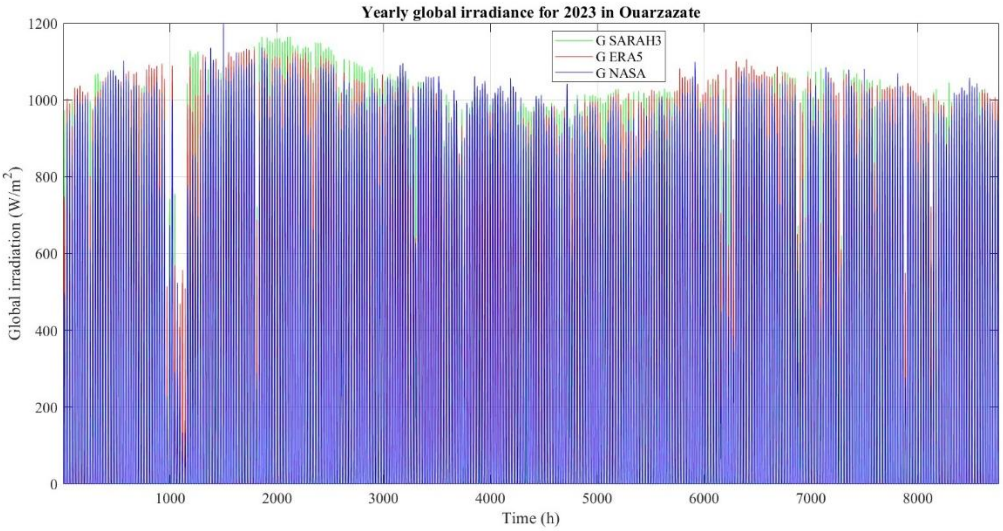

Figure 3.22 - Yearly global irradiance profile in Ouarzazate on an optimal angle tilted panel, with database values.

CALCULATED VALUES

Also for the site of Ouarzazate, in this section the global solar irradiance data on a horizontal plane are processed in order to obtain the corresponding values on a plane with optimal inclination, equal in this case to 32°. The formulas used are the same as those presented in the section dedicated to the city of Rabat. Below the results are reported in graphical form.

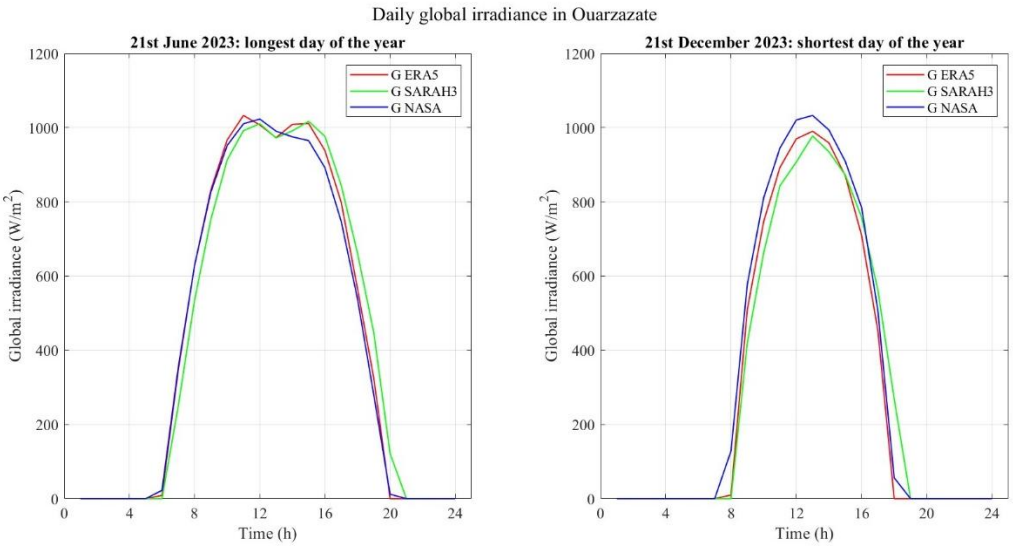

Figure 3.23 - Daily global irradiance profile in Ouarzazate on an optimal angle tilted panel, with calculated values.

In the daily graphs, regularity in the three curves is also repeated. During the summer solstice, at the site of Ouarzazate, peak values are slightly above 1000 W/m², and the curves of the three datasets are very close to each other. During the winter solstice, the bell-shaped curve is narrower but not lower, reaching maximums above 1000 W/m². The overall trend appears more stable and regular compared to Rabat, with less variability among the databases.

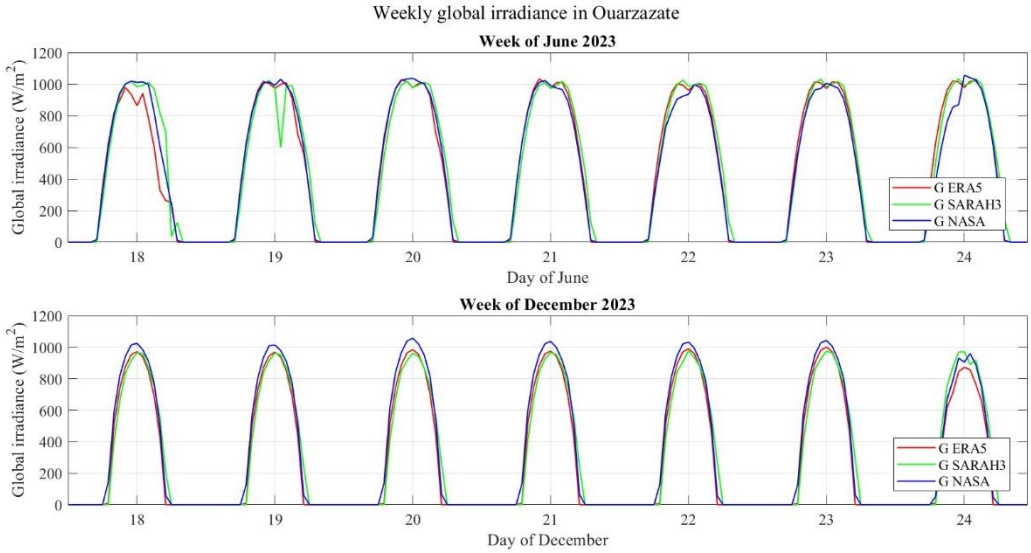

Figure 3.24 - Weekly global irradiance profile in Ouarzazate on an optimal angle tilted panel, with calculated values.

In the weekly analysis, for the days of June the daily peaks are between 900 and 1000 W/m². The dataset curves are consistent and regular, with NASA showing greater consistency among the days and SARAH-3 continuing to follow a broken curve. For the week of December, peak values remain high, between 980 and 1000 W/m². The curves are more irregular compared to June.

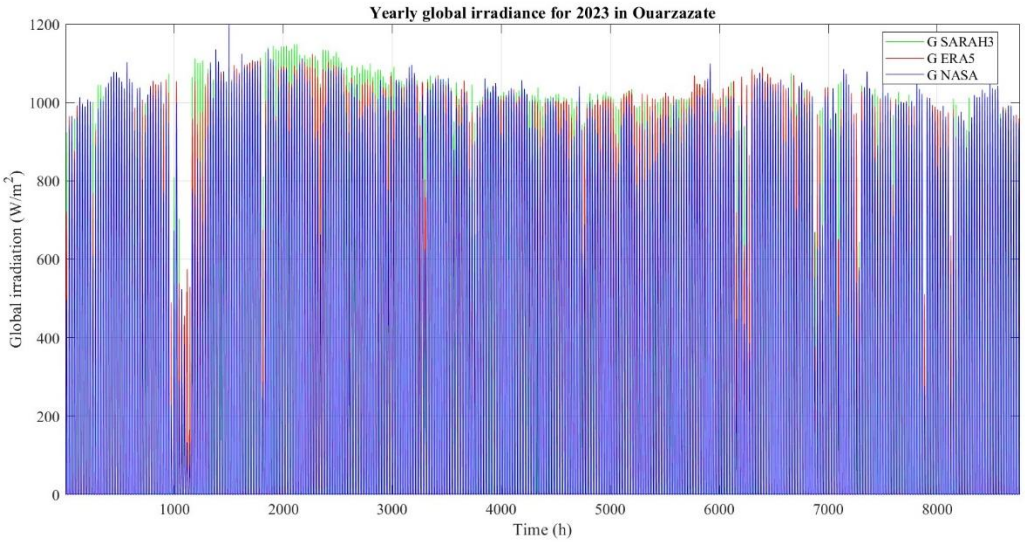

Figure 3.25 - Yearly global irradiance profile in Ouarzazate on an optimal angle tilted panel, with calculated values.

Finally, for the annual trend is characterized by maximum values around 1000 - 1100 W/m², with more regular and stable curves compared to Rabat. The overall trend is more sinusoidal and less dispersed, with seasonality almost absent throughout the year. The comparison with Rabat highlights how Ouarzazate presents a more stable solar potential, less influenced by atmospheric conditions.

3.3 Graphical comparison of WT parameters from different databases

For the acquisition of wind parameters, several limitations arise in identifying an open-access database that also provides a historical time series of past years, as most available datasets are primarily designed for forecasting purposes or lack an updated historical archive. For this reason, the ERA5 and MERRA-2 databases were selected, accessed respectively through the PVGIS interface and the NASA POWER Data Access Viewer.

The selected temporal range spans from 1 January 2023 to 31 December 2023, with an hourly temporal resolution. The resulting dataset consists of a .csv file containing 8760 wind speed values, at 10 meters of height, which is subsequently used as input for a program implemented in MATLAB.

The cities considered in the analysis are Rabat, Tangier, and Tarfaya. Rabat exhibits a moderate wind regime, strongly influenced by its proximity to the Atlantic Ocean, with generally stable average wind speeds throughout the year. Peak values occur more frequently during the spring and summer months, associated with coastal circulation patterns.

Tangier is located at the northernmost part of Morocco, near the Strait of Gibraltar, between the Atlantic Ocean and the Mediterranean Sea (35.76° N, 5.83° W). The city is characterized by a frequently strong and highly variable wind regime, with elevated peak values due to wind channeling effects within the strait.

Tarfaya is situated in the southwestern part of Morocco, along the Atlantic coast, in an area close to the Sahara Desert (27.94° N, 12.93° W). It is characterized by intense and persistent winds throughout the year, with high average wind speeds and frequent peak events.

The daily, monthly and annual graphical results for the three cities are presented in the following sections.

RABAT

Using a MATLAB program, a function is initially implemented to identify the windiest and least windy days in Rabat for the year 2023.

The following image presents the hourly graphical results for the least windy day, an average wind day, and the windiest day of 2023 for the city of Rabat. In this case, the graphs exhibit a smoother trend, showing that wind speed increases and decreases gradually without abrupt changes.

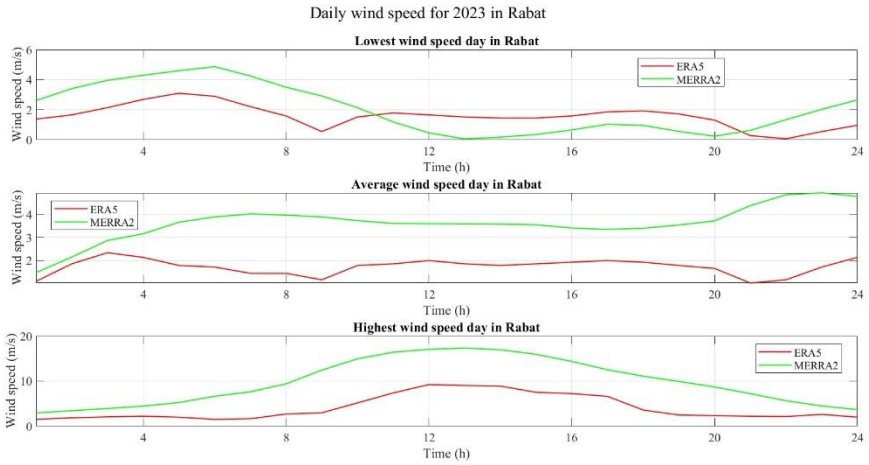

Figure 3.26 - Daily wind speed profile in Rabat at 10 meters of height.

As identified, the least windy day is 22 March 2023, during which a rise in wind speed is observed in the early hours of the day. The maximum peak reaches 4.9 m/s in the MERRA-2 database and 3.2 m/s in ERA5 at the same time. Only in the second part of the day do the two curves diverge, resulting in MERRA-2 values being lower than ERA5. This type of discrepancy is justifiable, as wind speeds are very low, making small differences difficult to detect.

For the day with an average wind speed, the differences between the two databases are even smaller, approximately 1.5 m/s throughout the day. Wind speeds remain fairly constant over the 24-hour period, averaging around 2 m/s for ERA5 and 3.9 m/s for MERRA-2.

The day with the highest wind speed is 22 October 2023. From the early hours of the day, wind speeds are around 5 m/s, increasing to 10 m/s for ERA5 and 17 m/s for MERRA-2. By the end of the day, the profiles gradually decrease.

After identifying these reference days, the investigation is expanded to a weekly timeframe. By plotting three days before and three days after each reference day, it is possible to obtain the complete week containing the least windy day, the week corresponding to the average wind speed value, and the windiest week.

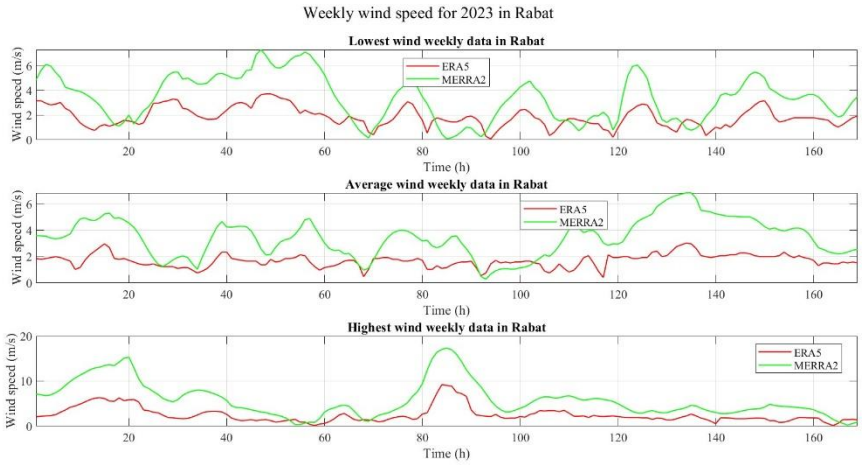

Figure 3.27 – Weekly wind speed profile in Rabat at 10 meters of height.

Since the least windy day for Rabat in 2023 was 22 March, the corresponding least windy week covers the period from 19 March to 25 March. The average wind speed during this week was 3.5 m/s, with a minimum of 0.06 m/s and peak values not exceeding 8 m/s. These values are typical for the area under consideration. Regarding the datasets, MERRA-2 presents slightly higher values than ERA5, while following the same trends and variations throughout the period.

A week characterized by an average wind speed was identified as the period from 3 January to 10 January 2023. The analysis showed an average wind speed of 2.5 m/s, a minimum of 0.5 m/s, and a peak of 7 m/s. Similarly, MERRA-2 reported higher values than ERA5, rarely falling below the latter's profile. Some values during this week were even higher than those recorded in the week containing the least windy day of the year, confirming that wind speed patterns are irregular and not easily predictable.

Finally, the week containing the windiest day of 2023 spans from 19 October to 25 October. The trends in both datasets were relatively consistent, ranging from near-zero wind conditions up to maximum values of 9.5 m/s for ERA5 and 17.2 m/s for MERRA-2. During the first day of the week, wind speed increased, particularly during nighttime hours, and then decreased over the subsequent days to approximately 2 m/s, a value typical for Rabat. On the fourth day, a temporary increase in wind speed was observed, which then stabilized over the following three days.

Expanding the analysis to a macroscopic level, the graphical output of wind speed trends over the entire year 2023 is analysed below.

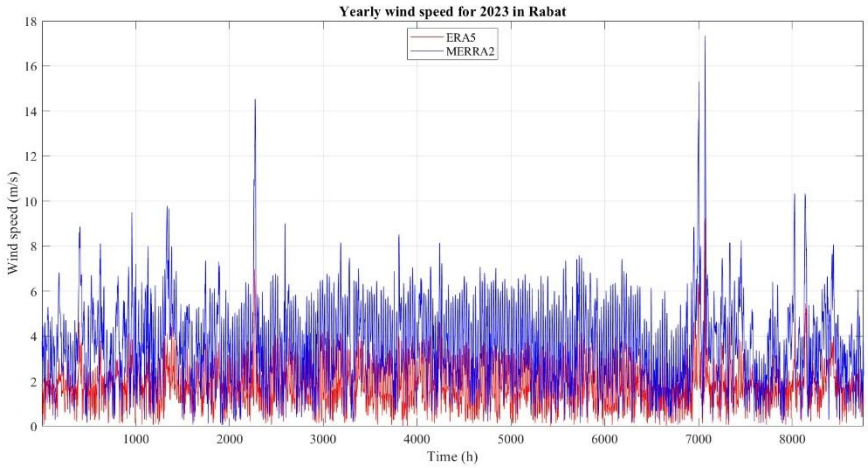

Figure 3.28 – Yearly wind speed profile in Rabat at 10 meters of height.

From this graph, even if in a qualitative manner, it can be observed that wind speed, unlike global solar irradiance, does not exhibit a bell-shaped annual trend or a clear seasonal dependence between winter and summer periods. Instead, wind speed displays more pronounced fluctuations, varying on a daily basis without a recurring or predictable pattern.

The average wind speed calculated over the entire year 2023 is equal to approximately 3.59 m/s. The observed peak values are around 9.5 m/s, while certain anomalies reach values exceeding 16 m/s. Since this behaviour is observed only in the MERRA-2 database and not in ERA5, it is concluded that these values are attributable to systematic and modelling errors rather than to actual wind gusts or storm events. Looking at the overall annual trends, the two databases show significant discrepancies: the MERRA-2 profile is almost uniformly shifted by approximately 2 m/s throughout the year, resulting in systematically higher wind speed values compared to the ERA5 database.

The graphical output of wind speed trends over the entire year 2023 is analysed below. The two databases show significant discrepancies, as the MERRA-2 profile is almost uniformly shifted by approximately 2 m/s throughout the year, resulting in systematically higher wind speed values compared to the ERA5 database.

TANGIER

By specifically analysing the minimum, average, and maximum wind speed values for the city of Tangier in 2023, the following reference days are identified: a minimum value of 0.03 m/s on 11 November 2023, an average value of 4.50 m/s

on 23 January 2023, and a maximum value of 15.98 m/s on 10 February 2023. The results of the daily analysis are presented in the following description and corresponding graphs.

The day characterized by the lowest wind speed is 11 November 2023, during which a very similar trend is observed in both the ERA5 and MERRA-2 datasets. The day begins with wind speed values of approximately 2.5 m/s, which then gradually decrease until reaching near-zero values around 12:00. The difference between the two curves remains limited throughout most of the day, on the order of approximately 0.5 m/s.

The average wind speed condition is observed on 23 January 2023. On this day, the ERA5 database reports wind speed values ranging between 3.5 m/s and 4.0 m/s for most of the 24-hour period, while the MERRA-2 database exhibits slightly higher values, varying from approximately 3.8 m/s to 6.2 m/s. Nevertheless, both datasets are characterized by limited intra-day fluctuations, indicating a relatively stable wind regime over the course of the day.

Finally, the day with the highest wind speed corresponds to 10 February 2023. During this day, the minimum wind speed recorded over the 24-hour period is 10.3 m/s. The wind speed increases during the central hours of the day, reaching peak values of approximately 13.8 m/s for the ERA5 dataset and 16 m/s for the MERRA-2 dataset. These values are considered plausible for the representation of a windy day in a coastal city such as Tangier.

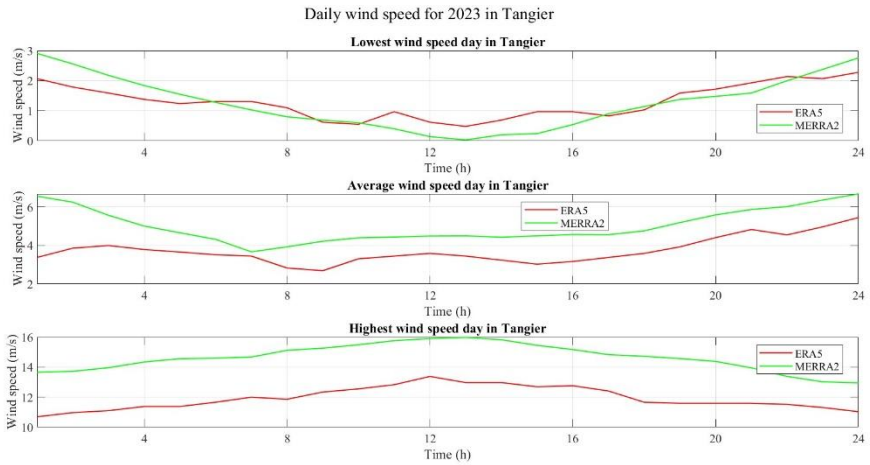

Figure 3.29 – Daily wind speed profile in Tangier at 10 meters of height.

Expanding the investigation to the weeks containing these reference days, the weekly analysis is presented below. From this weekly perspective, the period from 7 November to 14 November is identified as the least windy week of 2023. The average wind speed over these seven days is equal to 2.5 m/s, with several hours characterized by wind speeds close to 0 m/s and peak values not exceeding 3.9 m/s. Throughout the entire week, no significant alterations are observed, and the trend appears fluctuating but nearly constant.

A week characterized by an average wind speed is identified as the period from 20 January to 27 January. In this case, the average wind speed is 4.6 m/s; however, the trend is relatively variable, starting at the beginning of the week with values around 5 m/s, then decreasing and subsequently exhibiting peak values up to 10 m/s. The differences between the two databases are not substantial, and both datasets follow the same slope variations at the same time instants.

The third analysed week corresponds to the period from 7 February to 13 February 2023. During this week, the highest wind speed value of the year is recorded, reaching approximately 16 m/s. It is observed that in the preceding days the wind speed tends to increase and subsequently decrease in the following hours. Differences between the ERA5 and MERRA-2 databases are on the order of 2 m/s, and the recorded results are comparable on an hour-by-hour basis.

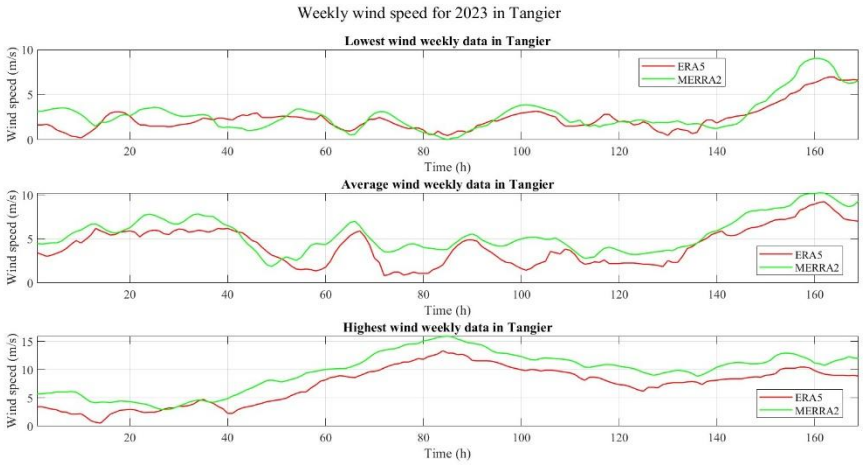

Figure 3.30 – Weekly wind speed profile in Tangier at 10 meters of height.

Broadening the perspective to a macroscopic level, the graphical output of wind speed trends over the entire year 2023 is analysed below.

From the graph, it can be qualitatively observed that the differences between the ERA5 and MERRA-2 datasets are significantly smaller than those identified for the city of Rabat. Throughout the year, both datasets exhibit changes in slope during the same periods, with wind speed values ranging between 6 m/s and 14 m/s in February, followed by an average trend between 1 m/s and 6 m/s during the central months of the year, and then increasing again between late September and early October.

Also in this case, the wind speed trend proves to be highly unpredictable, with no recurring or clearly identifiable peak or minimum periods throughout the year. However, the variation between maximum and minimum values is significantly higher than that observed for the city of Rabat, where wind speed remained relatively close to a consistent range throughout the year.

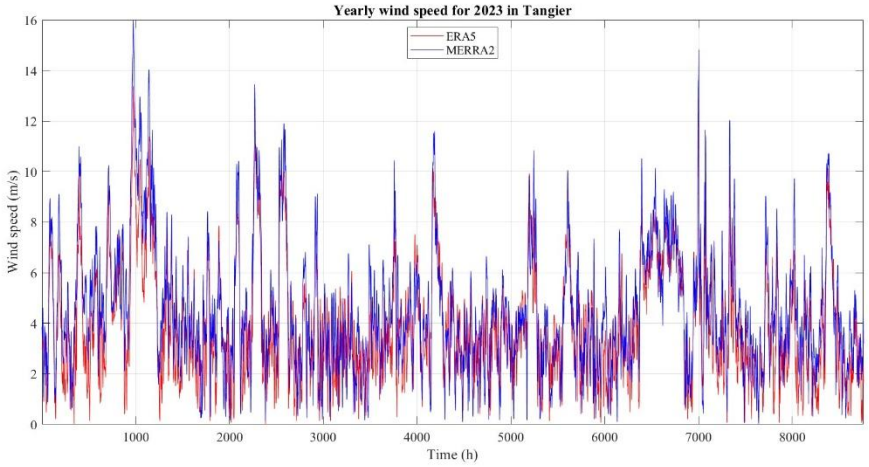

Figure 3.31 - Yearly wind speed profile in Tangier at 10 meters of height.

TARFAYA

The third city considered in this analysis is Tarfaya. To evaluate its wind profile, the daily wind speed trends for three representative days of 2023 are initially presented in the following description and corresponding graphs.

The first day, corresponding to the lowest wind speed, is 1 November 2023, during which the wind speed remains almost constant, with an average value of 1.9 m/s in the MERRA-2 dataset and 2.2 m/s in ERA5. The difference between the two

datasets is only a few tenths of a unit, and the minimum wind speed is approximately 0.02 m/s.

The day corresponding to the average wind speed is 1 February 2023, with a mean value of 5.56 m/s. In this case as well, the curve remains smooth and nearly constant over the 24-hour period, without significant maxima or minima.

The day with the highest wind speed is 7 November 2023, reaching a maximum value of 12.54 m/s. The entire day is characterized by high wind speeds, starting from a minimum of 9 m/s in the ERA5 dataset and increasing during the second part of the day, before decreasing around 20:00. The MERRA-2 dataset also shows high wind speed values, but with limited variation, exhibiting only minor fluctuations around 11 m/s.

Overall, the graphs obtained at the daily level are considered consistent and comparable.

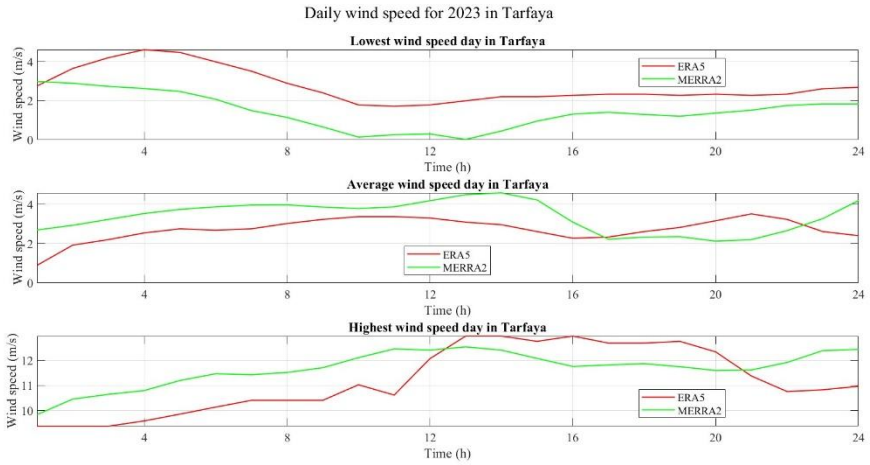

Figure 3.32 - Daily wind speed profile in Tarfaya at 10 meters of height.

Expanding the analysis to a weekly timeframe, the periods containing these three representative days are investigated. For the lowest wind speed condition, the week considered spans from 29 October to 4 November (centred around 1 November). The weekly wind data for Tarfaya, compared to the other two cities, exhibit a more variable trend, with the curve appearing more jagged. The average wind speed during this week is 5 m/s. The trend remains below 5 m/s during the first three days and increases gradually to reach approximately 10 m/s during the final three days of the week. Both databases display peaks and minimum at the same time instants;

however, small calibration and systematic errors prevent the curves from perfectly overlapping.

The week corresponding to average wind speed is that of 1 February 2023, covering the period from 28 January to 4 February. The mean wind speed during these seven days is 4.8 m/s, with minimum reaching 0 m/s and peaks up to 8 m/s. In this specific case, the trends of the two datasets diverge, with variations reaching up to 4 m/s. The slope of the trend differs between ERA5 and MERRA-2: ERA5 exhibits an almost bell-shaped profile, whereas MERRA-2 remains nearly constant.

The third week analysed includes the highest wind speed of the year and spans from 3 November to 10 November 2023 (centred around 7 November). During the first three days, wind speed averages approximately 6.4 m/s, then increases gradually before decreasing in a similar regular manner. In this case, the two datasets return to comparable trends, although the curves are not perfectly overlapping.

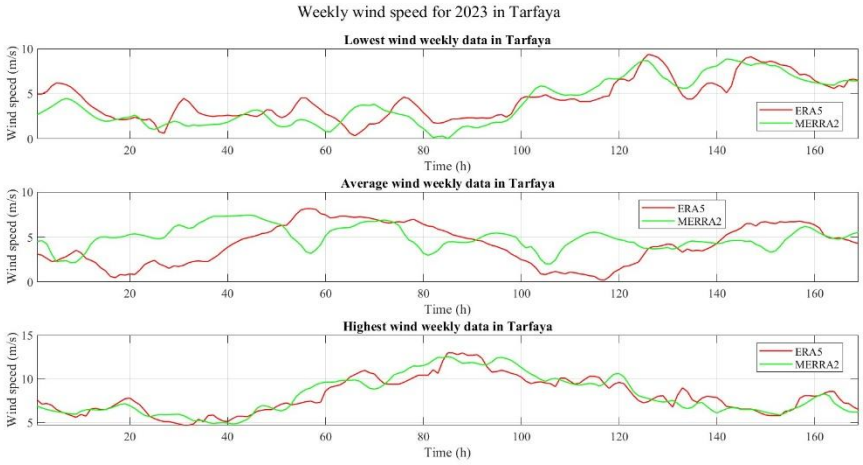

Figure 3.33 – Weekly wind speed profile in Tarfaya at 10 meters of height.

Broadening the perspective to a macroscopic level, the annual wind speed trend for Tarfaya is analysed below. The city is characterized by strong winds throughout the entire year 2023, with no pronounced seasonal variation in the wind speed profile.

Over the year, the trend shows a mean value of 5.56 m/s, which is higher than that observed for both previously analysed cities. As highlighted in the daily analysis, the absolute minimum wind speed is close to zero, consistent with the other cases, reaching a value of 0.02 m/s, while the maximum peak value is 12.54 m/s.

This peak value is lower than the maximum wind speeds recorded for Rabat and Tangier; however, this comparison is of limited significance, as isolated extreme values have been shown to correspond to anomalies, gusts, or windstorms that are not representative of the overall wind regime.

Looking at the overall annual trends, the ERA5 and MERRA-2 databases exhibit very similar behaviour, following the same changes in slope during the same periods of the year, with no substantial discrepancies between the two datasets.

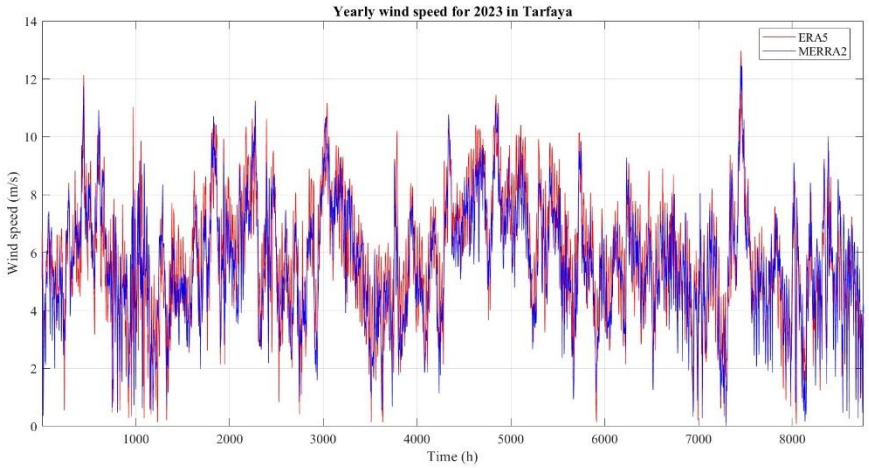

Figure 3.34 – Yearly wind speed profile in Tarfaya at 10 meters of height.

Chapter 4

4 Error analysis between different databases

This Chapter presents the error analysis of ERA-5, SARAH-3, and NASA datasets with respect to a reference profile, defined as the mean profile among the three datasets already considered up to this point.

Among the cities analysed in Chapter 3, only one is selected here to further develop the analysis of the different error metrics: Rabat.

Global irradiance and wind speed are the two parameters analysed in this Chapter and were identified as the most suitable variables for error analysis. Rabat is chosen because, in this city, both parameters have been considered and plotted previously.

In the MATLAB program, errors over the entire year 2023 are considered, and in the analytical results reported in Table 4.1 and Table 4.2. The average value over 8760 hours is presented, as this approach is more accurate and consistent than considering only a specific day.

Finally, the values obtained from the error calculation of the two fundamental parameters were used to estimate how these uncertainties propagate, ultimately affecting the error in the estimation of both photovoltaic and wind energy production.

4.1 Definitions of the considered error metrics

The error metrics considered relevant are presented in the following Sections: 4.1.1 Mean absolute error, 4.1.2 Root mean square error and 4.1.3 Error standard deviation.

4.1.1 Mean absolute error

The Mean Absolute Error (MAE) is a statistical metric used to quantify the average magnitude of the differences between the reference values and estimated or modelled values.

It provides a direct measure of the typical error committed by a model or dataset, without allowing positive and negative deviations to cancel each other.

The general formulation is:

$$MAE = \frac{1}{N}\sum_{i=1}^{N}\left|x_i - x_{ref}\right| \tag{4.1}$$

with:

- N: total number of observations, in this case $N = 8760$.
- x_i: dataset value.
- x_{ref}: reference dataset, mean profile of the three datasets.

It retains the same physical units as the variable under analysis, which facilitates interpretation. From a mathematical perspective, it corresponds to the L^1 norm of the error.

4.1.2 Root mean square error

The Root Mean Square Error (RMSE) quantifies the average magnitude of the deviations between reference data and each dataset considered.

The higher the RMSE, the greater the variability of the estimated data and the lower their reliability. RMSE is therefore used to assess whether the model produces consistent results or exhibits irregular errors.

The general formulation is:

$$RMSE = \sqrt{\frac{1}{N}\sum_{i=1}^{N}\left(x_i - x_{ref}\right)^2} \tag{4.2}$$

with:

- N: total number of observations, in this case $N = 8760$.
- x_i: dataset value.

- x_{ref}: reference dataset, mean profile of the three datasets.

It retains the same physical units as the variable under analysis, and it corresponds to the L^2 norm of the error.

4.1.3 Error standard deviation

The standard deviation is generally used to quantify the dispersion of a dataset around its own mean, describing its internal variability.

Its general formulation is:

$$\sigma = \sqrt{\frac{1}{N}\sum_{i=1}^{N}\left(x_i - x_{ref}\right)^2} \quad 4.3$$

However, in the present study the result of this formula equal and the objective is not to describe the intrinsic variability of each dataset, but rather to quantify the discrepancy between each dataset and the reference profile.

Therefore, computing the standard deviation of the dataset values around their own mean would not represent a measure of error, but only the internal variability of the series.

For this reason, the standard deviation of the errors is considered instead.

With the error defined as:

$$e_i = x_i - x_{ref} \quad 4.4$$

with:

- x_i: dataset value.
- x_{ref}: reference value (mean profile of the three datasets).

The error standard deviation general formulation is:

$$\sigma_e = \sqrt{\frac{1}{N}\sum_{i=1}^{N}(e_i - \bar{e})^2} \quad 4.5$$

with:

- N: total number of observations, in this case $N = 8760$.
- e_i: dataset error for each time step.
- $\bar{e}$: mean bias error for the entire dataset.

Unlike the standard deviation of the raw dataset, σ_e provides information on the consistency of each dataset with respect to the reference profile and represents a meaningful component of the overall error structure.

4.2 Error analysis numerical results

In this Section, error numerical results obtained by comparing ERA-5, SARAH-3 and NASA dataset are presented and analysed. The considered parameters are global irradiance and wind speed during the year 2023.

4.2.1 Global irradiance error numerical results

In this Section, the numerical results for global irradiance selected error metrics are presented and justified.

Table 4.1 - Error analysis for global irradiance.

GLOBAL IRRADIANCE			
Database	**MAE** (W/m²)	**RMSE** (W/m²)	σ_e (W/m²)
ERA-5	16.0	34.8	34.6
SARAH-3	22.5	43.1	43.0
CERES-SYN1	15.8	31.7	31.7

MEAN ABSOLUTE ERROR

The analysis of the Mean Absolute Error reveals the degree of consistency between each individual database and the reference Mean Profile. Among the analysed datasets, CERES-SYN1 exhibits the best performance with the lowest deviation, reporting a MAE of 15.784 W/m². This indicates that the CERES algorithms align closely with the ensemble average, likely due to its sophisticated cloud property retrieval mechanisms which effectively modulate surface irradiance.

ERA-5 shows a performance remarkably similar to CERES-SYN1, with a MAE of 15.982 W/m². This result is consistent with literature validating ERA-5 as a robust

reanalysis tool that, despite its coarser spatial resolution compared to satellite-only products, effectively captures the average dynamics of daily irradiance [41].

Conversely, SARAH-3 presents the highest deviation among the three, with a MAE of 22.488 W/m². While this value remains within acceptable limits for solar resource assessment, the higher MAE suggests that SARAH-3 may capture local transient phenomena or cloud optical depths differently than the reanalysis ERA-5 and the CERES system, leading to a larger average departure from the mean profile. In general, MAE values below 20-30 W/m² in inter-model comparisons indicate a strong coherence among the datasets regarding the daily evolution of global irradiance.

ROOT MEAN SQUARE ERROR

The Root Mean Square Error provides insight into the spread of the residuals and penalizes larger deviations more heavily than the MAE. Consistent with the MAE findings, CERES-SYN1 demonstrates the highest stability, achieving the lowest RMSE of 31.701 W/m². This suggests that large discrepancies or outliers between CERES-SYN1 and the mean profile are rare.

ERA-5 follows with an RMSE of 34.810 W/m². The proximity of this value to the CERES-SYN1 result reinforces the reliability of the ERA-5 reanalysis for energy applications, confirming its ability to reproduce global irradiance patterns with accuracy comparable to specialized satellite products, as noted in recent validation studies [43].

SARAH-3 records the highest RMSE at 43.058 W/m². The gap between SARAH-3 and the other two databases is more pronounced in the RMSE metric than in the MAE. This behaviour indicates that while SARAH-3 generally follows the mean trend, it is subject to more frequent or significant episodic deviations and larger scatter. This can be attributed to the different physical models used to treat cloud albedo and water vapor absorption in the SARAH algorithms compared to the ERA-5 assimilation scheme [42].

However, considering the typical variability of GHI, an RMSE in the range of 30 - 45 W/m² is characteristic of high-quality irradiance products when compared against a consensus mean.

ERROR STANDARD DEVIATION

The Error Standard Deviation isolates the random component of the error, removing the influence of systematic bias MBE. A crucial observation from Global irradiance error numerical results

In this Section, the numerical results for global irradiance selected error metrics are presented and justified.

Table 4.1 is that for all three databases, the values are almost identical to the RMSE values.

Mathematically,

$$RMSE^2 = MBE^2 - {\sigma_e}^2 \tag{4.6}$$

This proximity implies that the Mean Bias Error MBE is practically negligible for all datasets relative to the mean profile. This is an expected mathematical outcome when comparing individual members of an ensemble to the ensemble mean itself, as the biases tend to cancel out.

Consequently, the errors presented in Global irradiance error numerical results

In this Section, the numerical results for global irradiance selected error metrics are presented and justified.

Table 4.1 are almost entirely driven by random variance rather than systematic overestimation or underestimation.

CERES-SYN1 again shows the lowest dispersion equal to 31.7 W/m², confirming it as the dataset with the lowest noise relative to the group average. ERA-5 and SARAH-3 display higher variance with $\sigma_e = 34.6 \frac{\mathrm{W}}{\mathrm{m}^2}$ and $\sigma_e = 42.9 \frac{\mathrm{W}}{\mathrm{m}^2}$ respectively.

The higher standard deviation in SARAH-3 suggests that its day-to-day fluctuations are less correlated with the smoothed consensus of the Mean Profile, possibly due to its higher sensitivity to high-frequency cloud variability which might be smoothed out in the ERA-5 reanalysis and the mean profile itself [35].

4.2.2 Wind speed error numerical results

In this Section, the numerical results for wind speed selected error metrics are presented and justified.

Table 4.2 - Error analysis for wind speed.

WIND SPEED			
Database	**MAE** (m/s)	**RMSE** (m/s)	σ_e (m/s)
ERA-5	0.62	0.73	0.44
MERRA-2	1.24	1.47	0.88

MEAN ABSOLUTE ERROR

Regarding wind speed, the analysis of the Mean Absolute Error highlights a significant disparity in performance between the two reanalysis datasets when compared to the reference mean profile.

ERA-5 demonstrates superior consistency, recording a notably low MAE of 0.619 m/s. This result suggests that the European reanalysis aligns closely with the ensemble consensus, effectively capturing the daily wind dynamics.

In contrast, MERRA-2 exhibits a deviation exactly double that of its counterpart, with an MAE of 1.238 m/s.

This discrepancy is well-documented in the literature; although MERRA-2 is a robust tool for global climatology, validation studies often indicate that ERA-5 outperforms it in near-surface wind estimations [44].

The performance gap is largely attributed to the higher spatial and temporal resolution of ERA-5 (~31 km grid) compared to MERRA-2 (~50 km grid), which allows the former to better resolve local wind patterns and topographic effects that influence the mean profile construction.

ROOT MEAN SQUARE ERROR

The Root Mean Square Error analysis reinforces the trends observed with the MAE, emphasizing the stability of the ERA-5 dataset.

The RMSE for ERA-5 is restricted to 0.733 m/s, a value that is considered excellent in wind resource assessment, where errors below 1 m/s are typically targeted for reliable energy yield predictions.

Conversely, MERRA-2 presents a higher RMSE of 1.466 m/s. Since the RMSE is particularly sensitive to larger errors, this indicates that while MERRA-2 generally follows the synoptic trends, it experiences more frequent or sharper deviations from the mean profile.

These deviations may stem from differences in the data assimilation schemes (4D-Var for ERA-5 and 3D-Var for MERRA-2), which affect how observational data is integrated into the atmospheric model, leading to distinct behaviours during periods of high wind variability or rapid atmospheric transitions [45].

ERROR STANDARD DEVIATION

The analysis of the Error Standard Deviation provides insight into the random component of the error, separating it from systematic bias.

For ERA-5, the standard deviation is remarkably low at 0.439 m/s. Interestingly, there is a noticeable difference between the RMSE = 0.733 m/s and the σ_e= 0.439 m/s.

This implies, according to Eq. 4.6, the presence of a non-negligible systematic bias MBE between ERA-5 and the mean profile, likely caused by the specific weighting or averaging method used to generate the reference profile.

For MERRA-2, the standard deviation rises to 0.877 m/s. The wider dispersion confirms that the random noise in the MERRA-2 dataset is significantly higher than in ERA-5.

From an engineering perspective, a lower σ_e in ERA-5 implies that its fluctuations are more predictable and strictly correlated with the reference trend, whereas MERRA-2 exhibits a more scattered distribution of residuals.

This confirms the findings of recent comparative studies, which position ERA-5 as the current state-of-the-art for wind energy applications due to its reduced random error and better representation of the planetary boundary layer [46].

4.3 Statistical analysis of error metrics

This Section provides a statistical analysis of the Mean Bias Error and the normalized Mean Absolute Error. Global irradiance and wind speed are selected as the reference parameter for this analysis.

The numerical results presented in Section 4.2 are now illustrated using boxplots and histograms, binned into irradiance categories ranging from 0 W/m^2 to 1000 W/m^2 with steps of 50 W/m^2 [47] and wind speed categories from 0 m/s to 7 m/s with 1 m/s steps.

Specifically, in this analysis, the following statistical parameters are plotted for each category:

- The first quartile (25th percentile), representing the value below which 25% of the distribution lies, and the third quartile (75th percentile), defining the lower 75% of the data.
  These values constitute the lower and upper bounds of the blue "boxes", which enclose the central 50% of the distribution called interquartile range.

- The median (50th percentile), indicated by a red line, which defines the central value of the distribution and separates the lower and upper halves of the data.
- The minimum and maximum observed values, excluding anomalies, identified by the black "whiskers."
- The outliers, displayed as individual points, plotted in this case within a range from a minimum of -200 W/m^2 to a maximum of +200 W/m^2.
- A green curve representing the mean of the errors, which mathematically corresponds to the MBE, is superimposed on the plot.

4.3.1 MBE graphical results for global horizontal irradiance

The boxplot graphical results for global irradiance values for the databases ERA-5, SARAH-3 and NASA are presented, and green curve represents the mean value of the bias errors.

The boxplot is accompanied by the data distribution of the predicted irradiance, allowing for the statistical contextualization of the results within each category.

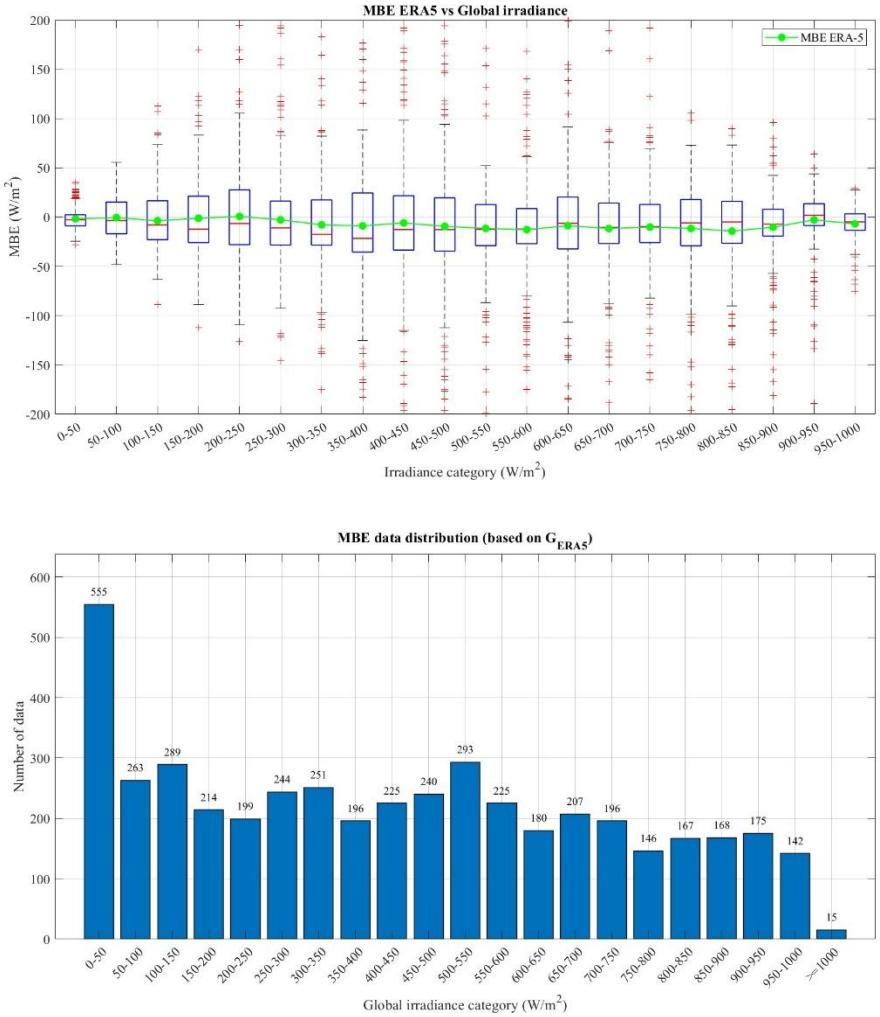

Figure 4.1 - MBE statistical distribution for ERA-5 database.

The first graphical analysis focuses on the Mean Bias Error distribution for the ERA-5 dataset across the binned irradiance categories.

Observing the medians, indicated by the red horizontal lines within the boxes, a clear systematic tendency of the database to underestimate the global irradiance emerges, as the central values consistently lie below the zero-error threshold across almost all boxplots, particularly from 100 to 850 W/m².The statistical dispersion, represented by the height of the interquartile range, reaches its maximum in the low-to-intermediate irradiance categories, specifically between 200 W/m² and 400 W/m².

Conversely, the model performs remarkably well at both the extremes of the spectrum: the boxes and whiskers are extremely narrow in the highest irradiance categories from 850 to 1000 W/m², as well as in the lowest 0-50 W/m² bin,

demonstrating high accuracy and stability under very cloudy and clear-sky conditions.

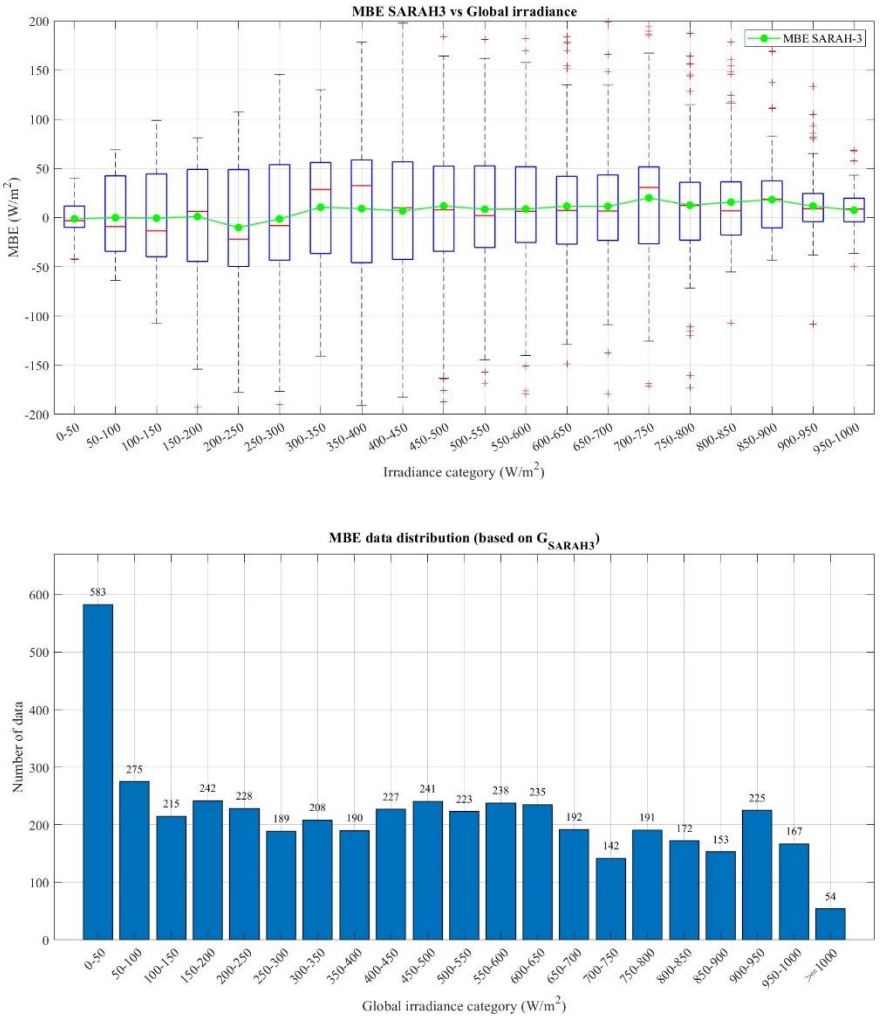

Figure 4.2 - MBE statistical distribution for SARAH-3 database.

In stark contrast to ERA-5, the MBE boxplot for the SARAH-3 database reveals a more complex error profile, characterized by an underestimation at lower irradiances and a pronounced systemic overestimation in the mid-to-high ranges.

From the 300 W/m² bin up to the 800 W/m² bin, the medians are visibly shifted into the positive domain, peaking at a positive bias of approximately +30 W/m² in the

350-400 W/m² and 700-750 W/m² categories, following a noticeable negative dip of about -20 W/m² in the 200-250 W/m² range.

The widest boxes are located in the intermediate ranges between 300 and 500 W/m², highlighting a significant spread in absolute errors. The upper whiskers in these categories stretch significantly upwards, indicating that the model occasionally overestimates irradiance by nearly +200 W/m² before reaching the outlier threshold.

However, for irradiance values exceeding 850 W/m², the distribution tightens significantly closer to zero, confirming that SARAH-3 also provides highly reliable estimates when dealing with peak solar radiation.

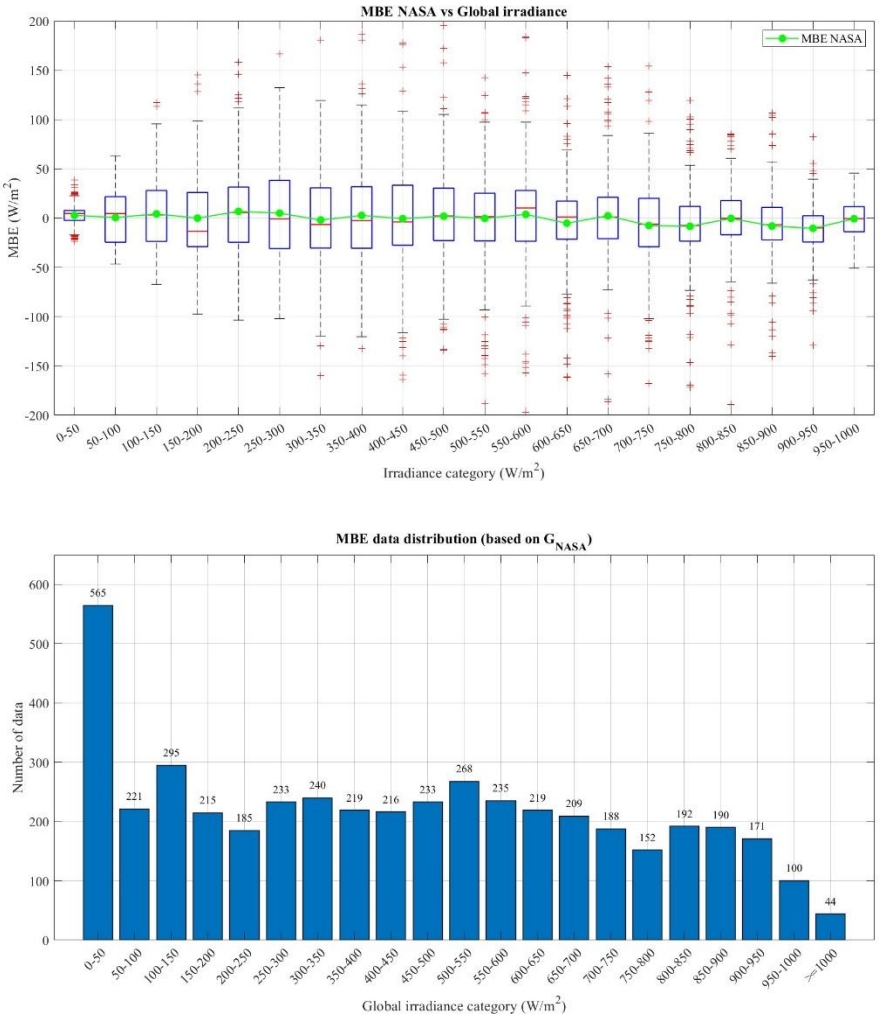

Figure 4.3 - MBE statistical distribution for NASA database.

The NASA database MBE boxplot presents a more balanced overall error profile compared to the previous two datasets.

The medians fluctuate closely around the zero line across the entire spectrum, showing no severe systemic underestimation or overestimation, apart from a slight negative bias in the 100-300 W/m² range and a minor positive shift between 550 and 650 W/m².

Despite this centered median, the interquartile ranges, blue boxes, maintain a considerable width across a broad plateau from 150 W/m² to 600 W/m², suggesting a persistent variance in absolute error.

Furthermore, the presence of dense, symmetrical outliers, red crosses, reaching the ±200 W/m² limits in almost every category indicates that while the NASA model is accurate on average, it is susceptible to occasional, yet significant, individual prediction errors regardless of the irradiance level.

4.3.2 NMAE graphical results for global horizontal irradiance

This Section analyses the boxplots and distribution charts of the nMAE for the ERA-5, SARAH-3, and NASA databases, evaluated against the reference dataset, i.e. the ensemble mean of the three.

Analogous to the previous Section, blue boxplots are utilized to represent the distribution of the individual percentage normalized absolute errors. These are calculated by dividing the absolute difference between the predicted and measured values by 1000 W/m^2 and expressing the result as a percentage. The green curve represents the mean value of these errors, the normalized absolute error itself, is superimposed on the graph. The boxplot is accompanied by the data distribution of the predicted irradiance, allowing for the statistical contextualization of the results within each category.

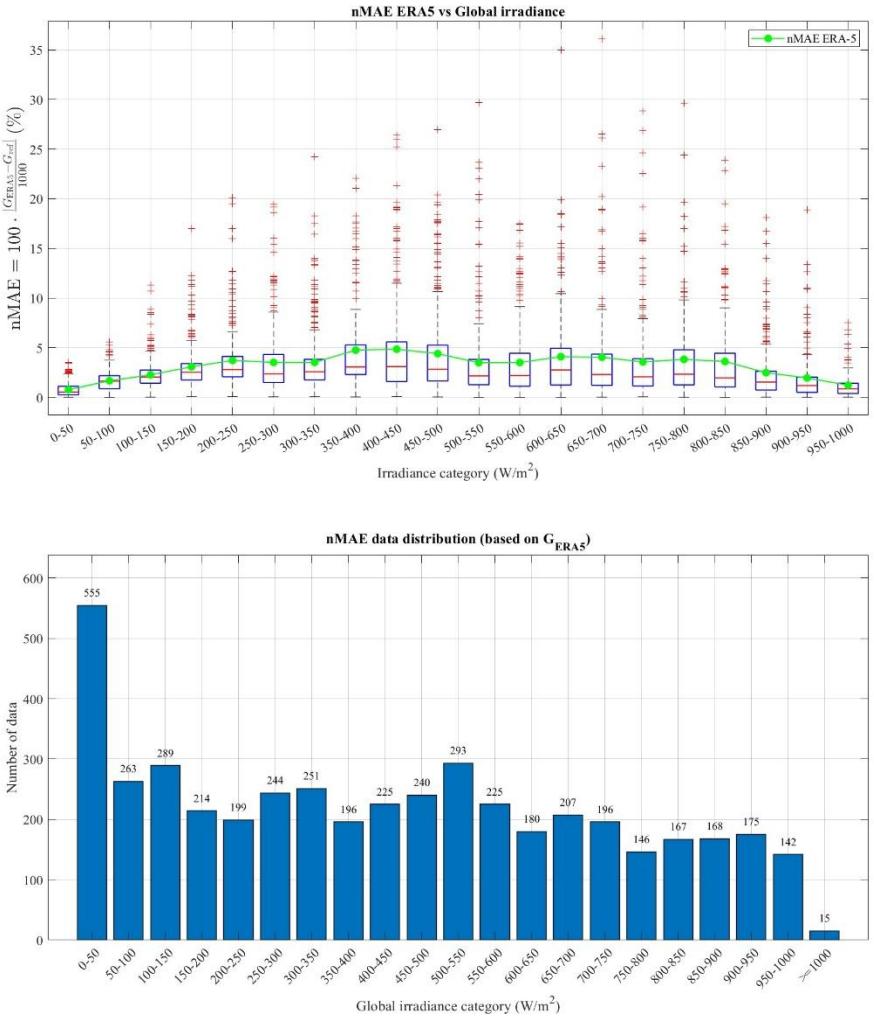

Figure 4.4 - nMAE statistical distribution for ERA-5 database.

The first graphical analysis focuses on the Normalized Mean Absolute Error chart for ERA-5.

The relative uncertainty exhibits a bell-shaped distribution across the spectrum, peaking in the intermediate irradiance categories. In the lowest irradiance boxplots 0-50 W/m^2, the mean error is surprisingly minimal, starting around 1%, with extremely compact interquartile ranges. This is mathematically driven by the normalization factor (fixed at 1000 W/m^2), which suppresses the percentage error at low absolute values.

As irradiance increases, the ERA-5 model's absolute variance grows in the intermediate 350-450 W/m^2 categories, the green mean curve peaks at just under

5%, and the blue boxes widen, covering a spread from approximately 1.5% up to 5.5%.

However, beyond the 850 W/m^2 threshold, the relative accuracy improves drastically. The boxes become extremely compact again, and the mean error smoothly stabilizes below 2.5%, proving the dataset's robustness for high-yield solar energy assessments.

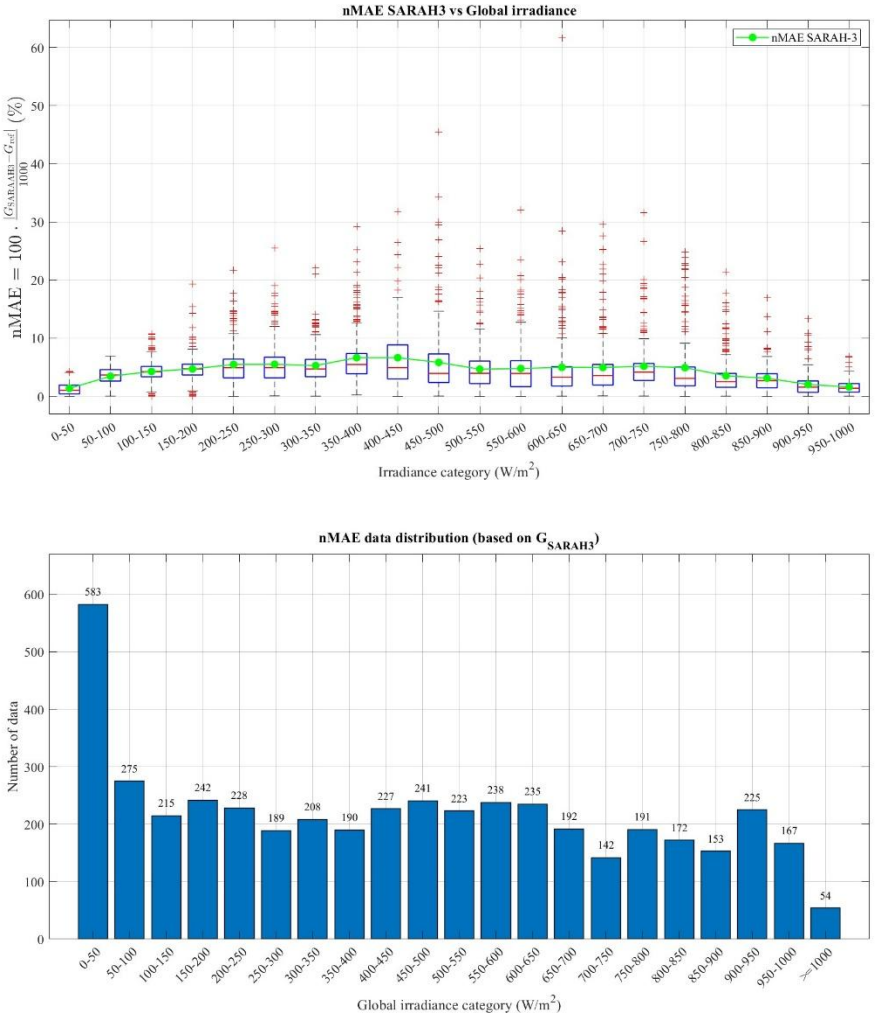

Figure 4.5 - nMAE statistical distribution for SARAH-3 database.

The SARAH-3 nMAE distribution exhibits an overall higher error profile with a more pronounced peak in the intermediate ranges compared to ERA-5.

In the 400-450 W/m^2 boxplot, the mean relative error reaches its highest value of roughly 6.5%, with the 75th percentile box edge capping near 9%. This confirms

that SARAH-3 experiences its greatest absolute deviations during mid-level or highly variable conditions. Furthermore, exceptional outliers are present, notably one isolated instance in the 600-650 W/m^2 bin exceeding 60%.

Nevertheless, the error profile is highly constrained at the extreme edges of the spectrum. By the time the irradiance reaches the lowest category 0-50 W/m^2 or the highest category >900 W/m^2, the green curve drops to roughly 1-2%. For values above 850 W/m^2, the boxes shrink to a minimal width, highlighting excellent relative precision for nominal and peak operating conditions of solar energy systems.

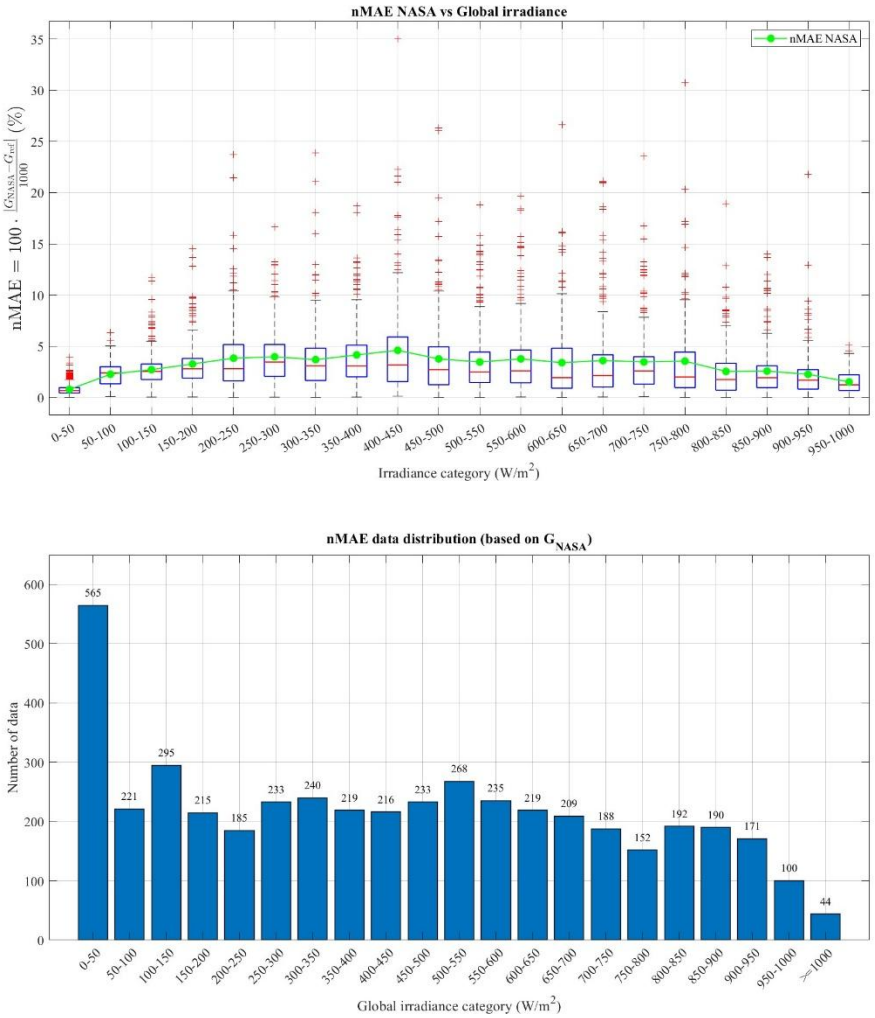

Figure 4.6 - nMAE statistical distribution for NASA database.

Finally, the nMAE distribution for the NASA dataset follows a similar bell-shaped trend to ERA-5, but with specific distributional characteristics regarding its outliers.

The mean error in the lowest 0-50 W/m^2 class is minimal and around 1%, but notably, this category contains a dense cluster of outliers reaching up to 4%, showing concentrated instances of mismatch at near-zero irradiances.

Despite this, the model's bulk error peaks similarly in the mid-range: the interquartile boxes widen significantly around 400-450 W/m2, where the green mean relative error rises to roughly 4.5% and outliers reach up to 35%.

For the high irradiance classes above 850 W/m2, the NASA database shows outstanding consistency, with tighter boxes and a mean percentage error flattening out near the 1.5-2.5% mark, indicating minimal relative deviation from the ensemble reference during clear-sky hours.

4.3.3 MBE graphical results for wind speed

In this Section, the same categorization procedure used for global radiation is applied to the wind speed data, using 1 m/s step increments. For the Mean Bias Error, the lower and upper limits are set to -5 m/s and +5 m/s, respectively. Categories containing fewer than 30 observations are filtered out and excluded from the analysis. These typically correspond to the highest wind speed ranges, which are reached only during occasional turbulence peaks.

Subsequently are presented the boxplot results for the datasets ERA-5 and MERRA-2.

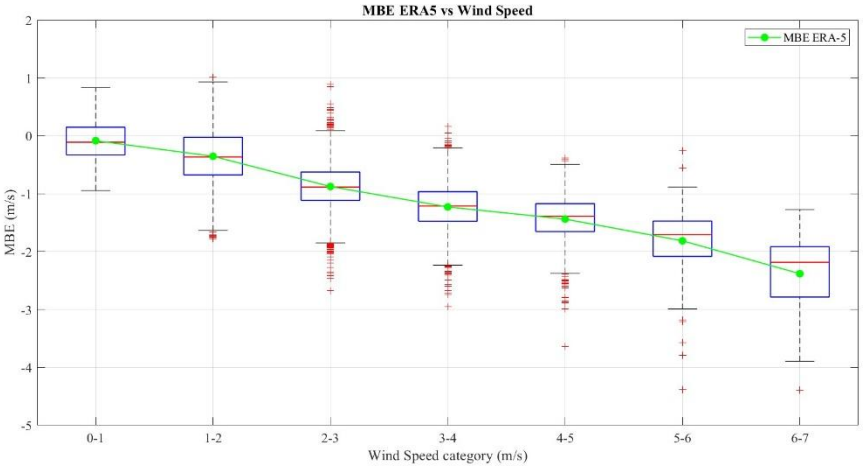

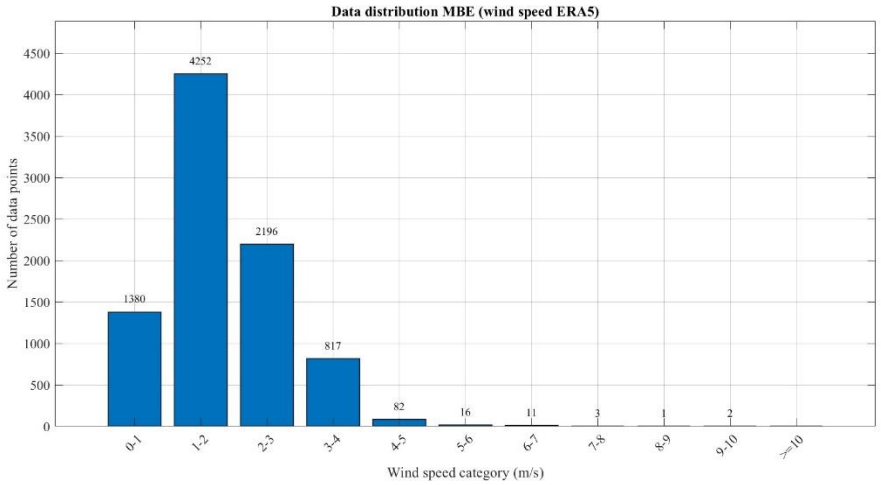

Figure 4.7 - MBE statistical distribution for ERA-5 database.

A distinct downward trend is observable for ERA5 model's systematic error as a function of the measured wind conditions.

For low wind speeds such as 0-1 m/s category, the error is close to zero, suggesting adequate calibration. However, as wind speed increases, the mean green line and the blue boxes progressively shift towards negative values. In the 6-7 m/s category, the average MBE reaches approximately -2.5 m/s.

The ERA5 model exhibits a systematic tendency to underestimate wind speed compared to the reference data. The magnitude of this underestimation increases proportionally with higher actual wind speeds.

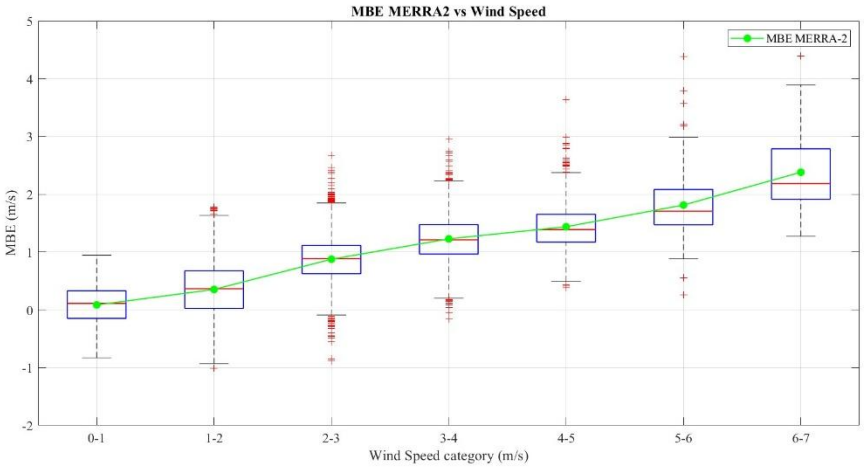

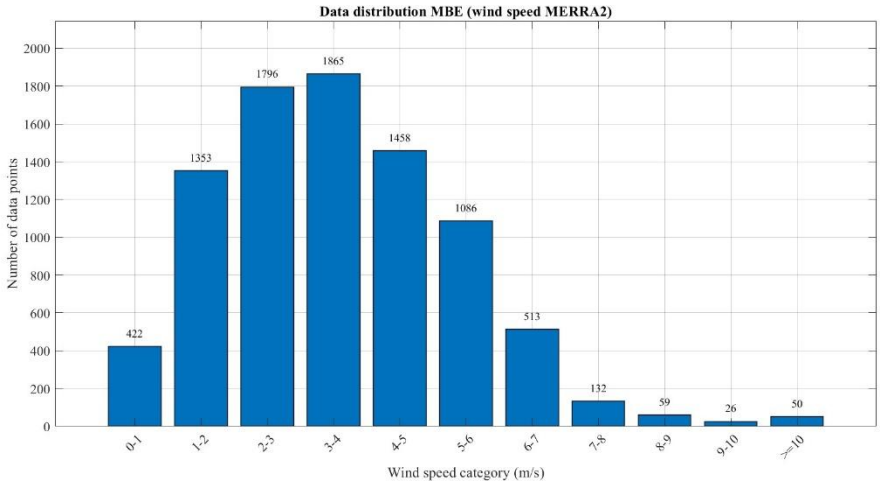

Figure 4.8 - MBE statistical distribution for MERRA-2 database.

The trend observed in graph of the systematic error for the MERRA2 is virtually the inverse of that seen in the ERA5 dataset.

Starting from an almost negligible bias in the lowest wind category such as 0-1 m/s, the MBE displays a clear positive, upward trajectory. As wind intensity increases, the mean error rises almost linearly, exceeding +2.0 m/s in the 6-7 m/s wind speed class.

In contrast to ERA5, the MERRA2 model systematically overestimates wind speed. Like the previous dataset, however, the model's structural bias amplifies proportionally as the true wind speed increases.

4.3.4 NMAE graphical results for wind speed

In this Section, the graphs of the normalized Mean Absolute Errors (nMAE) are presented. The normalization is performed with respect to a reference value corresponding to the mean wind speed calculated over the entire annual dataset of 8760 observations that corresponds to 2.71 m/s.

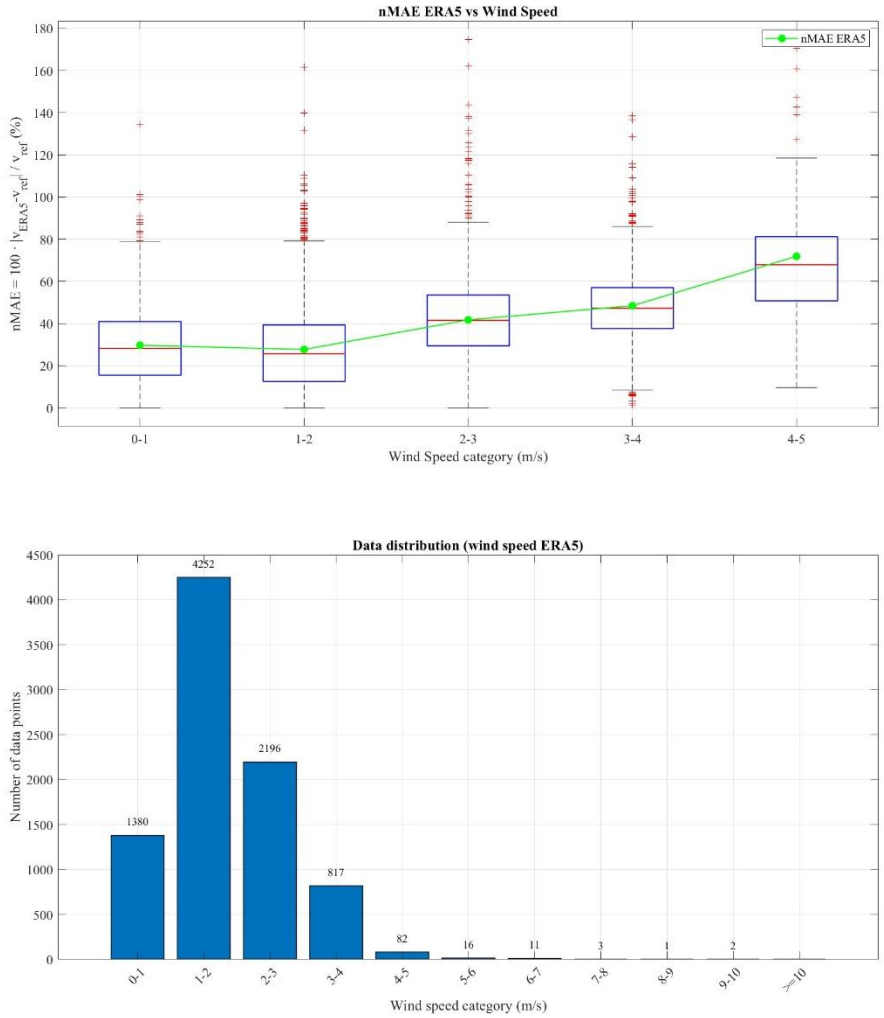

Figure 4.9 - nMAE statistical distribution for ERA-5 database.

In the ERA-5 dataset, the nMAE establishes a baseline of approximately 30% error in the lowest wind categories of 0-1 m/s and 1-2 m/s, indicating a relatively stable initial calibration. Following this phase, the error escalates sharply: the mean value represented by the green line exceeds 40% in the 2-3 m/s range and spikes dramatically past 70% in the 4-5 m/s category.

A cross-reference with the ERA5 data distribution histogram is fundamental to accurately interpreting this graph. The ERA5 dataset is heavily left-skewed, with most measurements concentrated in very low wind. Beyond 3 m/s, the sample size collapses precipitously; the 4-5 m/s category, where the error spikes so dramatically, contains a mere 82 data points out of thousands of total samples.

Therefore, the massive percentage errors and extreme outliers recorded at the upper boundary of the ERA5 boxplot are statistically insignificant. These extreme values represent mathematical anomalies generated by a sample size too small to be representative, and consequently, they must be discarded from the general assessment of the database's predictive capability.

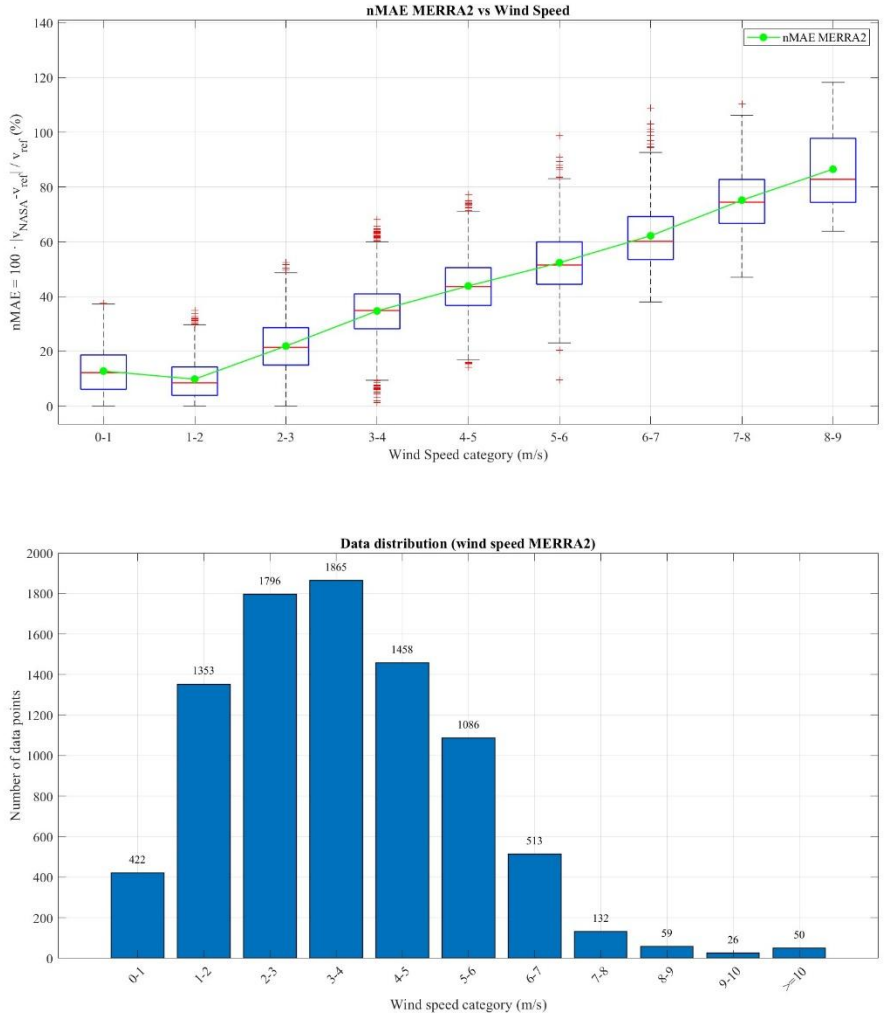

Figure 4.10 - nMAE statistical distribution for MERRA-2 database.

As for the MERRA-2 dataset, a structurally different, near-linear upward trajectory in the percentage error is evident. For low wind, the model exhibits excellent accuracy, with the mean nMAE hovering around a 10-15%. However, as wind intensity increases, the error begins a steady ascent, surpassing 50% in the 5-6 m/s range and approaching 90% in the 8-9 m/s category.

Crucially, the interpretation of this severe error amplification at higher wind speeds must again be contextualized using the data distribution histogram. Unlike ERA-5, the MERRA-2 dataset features a more robust, bell-shaped distribution centred around moderate winds and maintains statistical validity up to the 5-6 m/s class.

Nevertheless, the availability of data drops drastically at the extreme right tail. For instance, the 7-8 m/s and 8-9 m/s categories contain only 132 and 59 data points, respectively. Consequently, while the trend shows a genuine degradation in model performance as wind increases, the exceptionally high percentage errors and wide variance observed in these final upper categories lack statistical robustness.

Just as with ERA-5, rather than indicating a complete structural failure of the model, these extreme values at high wind speeds are primarily driven by data scarcity, should be considered statistical anomalies, and must be discarded when evaluating the model's overall reliability.

4.4 Error propagation in energy production estimation

This Section analyses the error propagation associated with global irradiance and wind speed parameters, and its impact on photovoltaic and wind power generation, respectively.

The numerical results of the error analysis are presented for each database under consideration. Such an investigation highlights how uncertainties in a single input parameter can significantly alter the estimated energy yield.

Consequently, understanding these deviations is crucial for the design of new power plants that rely on satellite-derived datasets, thereby emphasizing the strict need for their validation.

4.4.1 Error impact on PV energy estimation

Solar power generation calculation relies on the following formula, which highlights the direct dependence of the power output on solar irradiance:

$$P_{PV} = P_{nom} \cdot \frac{G}{G_{STC}} \cdot [1 + \gamma(T_{cell} - T_{STC})] \quad 4.7$$

with:

- P_{PV}: output power generated by the PV module.
- P_{nom}: nominal power of the considered module at standard test conditions.

- G: incident solar irradiance on the plane of the array.
- G_{STC}: reference solar irradiance at STC = 1000 W/m^2
- γ: temperature coefficient for power, representing the performance degradation as temperature rises.
- T_{cell}: operating temperature of the PV cell.
- T_{STC}: is the reference temperature at STC = 25°C.

A second parameter affected by error is the cell temperature, which also exhibits a direct proportionality to solar radiation, depending on the parameters already described in Eq. 1.5 of Section 1.1.3.

$$T_c = T_a + (NOCT - 20) \cdot \frac{G}{800} \quad 4.8$$

To compute the numerical results on power generation, a MATLAB script is implemented to evaluate the overall annual percentage error of global irradiance for each dataset, yielding the results ΔG shown in Table 4.3.

An experimental approach was preferred over the partial derivative method for error propagation analysis. First, the cell temperature was calculated using typical daily average parameters; specifically, both the maximum irradiance incorporating the maximum positive error and the nominal irradiance were substituted into Equation 4.8. The relative percentage error was then determined with respect to the nominal value. It is observed that the cell temperature is linearly affected by the irradiance error, which propagates directly to the temperature calculation, as shown in the results.

Subsequently, the specific cell temperature values were used in Equation 4.7 to derive the maximum and nominal photovoltaic power outputs. Finally, the relative error between these two power values was calculated for the three datasets and summarized in the table. The power generation of a single monocrystalline panel is calculated assuming the following typical values constant for the city of Rabat during the peak hours:

- $G = 850 \pm \Delta G$ W/m^2
- $\gamma = -0.0035$/°C
- $NOCT = 45$°C
- $T_{amb} = 30$ °C and, consequently $T_{cell} = 56.6$ °C
- $P_{nom} = 450$ Wp and, consequently $P_{PV} = 340$ W.

The results estimate for each dataset are summarized in Table 4.3, alongside their respective percentage errors relative to the expected average value.

Table 4.3 – Error propagation for a single panel PV power generation yield.

DATABASE	ΔG	T_{CELL}	P_{PV}	ΔP_{PV}
ERA-5	3.1%	57.4 °C	350W	2.9%
SARAH-3	3%	57.4 °C	350W	2.9%
NASA	4.3%	57.7 °C	354W	4.1%

As shown, the percentage error affecting the power output is consistently slightly lower than the corresponding error on global irradiance.

This damping effect is strictly related to the thermal behaviour of the photovoltaic module, since higher irradiance estimates inherently lead to higher calculated cell temperatures. Consequently, the resulting thermal losses partially offset the expected power gain, thereby mitigating the initial error and reducing the final deviation in power generation.

4.4.2 Error impact on WT energy estimation

This Section investigates how the error in the wind speed parameter propagates to wind power generation.

The power calculation relies on the following equation, previously described in Section 1.2.1:

$$P_{WT} = \frac{1}{2} \cdot \rho \cdot A \cdot C_p \cdot v^3 \tag{4.9}$$

The equation clearly highlights the cubic dependence of power on wind speed, thereby amplifying the impact of any associated estimation error.

In this case as well, the error was not determined using partial derivative theory; instead, an experimental approach was adopted through a MATLAB script. Typical reference point values were processed to calculate both the maximum wind power output incorporating the maximum error percentage for each dataset and the

nominal reference power. The relative percentage error was then calculated as the difference between these two results, normalized to the reference value.

The numerical results of power production for a residential wind turbine are summarized in Table 4.4, evaluated for the typical values characterizing the city of Rabat:

- $\rho = 1.225$ kg/m^3
- h = 20 meters
- R = 3.5 m and, consequently A = 38.5 m^2
- $C_p = 0.40$
- $v = 5$ m/s and, consequently $P_{nom} = 1180$ W.

Table 4.4 – Error propagation for a single residential WT power generation yield.

DATABASE	ΔV	P_{WT}	ΔP_{WT}
ERA-5	20%	2040W	73%
MERRA-2	25%	2300W	95%

It is crucial to note that the percentage error in wind power generation is not simply triple the error in wind speed, as the current approach is experimental rather than theoretical.

Linear error propagation theory suggests $\Delta P_{WT} \approx 3\Delta v$ and this approximation is only valid for small deviations. For significant errors, such as the 20% or 25% observed in satellite datasets, the mathematical expansion of the cubic term $V^3 = (V \pm \Delta V)^3$ introduces higher-order components that heavily amplify the final deviation.

A 25% overestimation in wind speed strictly translates to a severe 95% overestimation in calculated power, highlighting the extreme sensitivity of wind energy assessments to the accuracy of input meteorological data. The resulting error in wind power remains comparable to a threefold error in wind speed and these findings align with the theoretical partial derivative framework, even though the methodology employed deviates from it.

4.5 Final evaluation of databases' performance

Based on the comparative error analysis presented in Sections 4.2 and **Errore. L'origine riferimento non è stata trovata.**, a definitive assessment can be made regarding the suitability of the analysed databases for scientific research and energy system planning in Morocco.

Regarding solar irradiance, the results indicate an elevated level of accuracy for both the NASA dataset with CERES-SYN1 model and ERA-5 dataset.

CERES-SYN1 exhibited the lowest statistical error MAE, confirming its status as a high-precision tool for purely solar applications, particularly effective in capturing cloud radiative effects in the distinct climatic zones of Morocco, from the Mediterranean coast to the Sahara.

However, ERA-5 showed a performance remarkably close to the satellite product, demonstrating that modern reanalysis data can successfully compete with specialized satellite derivations for daily global irradiance estimations.

In terms of wind speed, the distinction is far more pronounced. ERA-5 significantly outperforms the NASA dataset that uses MERRA-2 model, halving the MAE and reducing the random dispersion σ_e.

This superiority is critical for the Moroccan territory, where wind resources are heavily influenced by complex orography like the Atlas Mountains and thermal breezes along the Atlantic coast. The coarser resolution of MERRA-2 proves less adequate for capturing these local wind regimes compared to the finer grid and advanced assimilation of ERA-5.

In conclusion, given this massive advantage in wind modelling and the near-identical solar performance, to have consistency between data and different parameters, ERA-5 is evaluated as the best reference database for the reliable simulation of renewable energy systems in the Moroccan territory.

Chapter 5

5 The case study of the residential PV power plant at UIR

In this Chapter, a case study of a residential photovoltaic power plant located at the Université Internationale de Rabat (UIR) is presented.

Section 5.1 describes the system configuration, including its installed capacity, power electronics, and energy storage specifications.

Section 5.2 considers historical production data obtained from the university's meteorological station.

In Section 5.3, the error analysis is further developed by comparing the real dataset adopted as a reference with a satellite-based database selected according to the criteria defined in Section 4.1. This comparison is carried out in order to validate the acceptability and reliability of the data collected at the university.

5.1 Description of the university PV power plant

The EEBLAB laboratory photovoltaic system consists of 8 panels, with 2 panels for each technology, in order to allow a comparative analysis within the laboratory of the energy production and efficiency of the different types of modules. Specifically, 2 single-crystalline panels (s-Si), 2 multi-crystalline panels (mc-Si), 2 amorphous silicon panels (a-Si), and 2 Copper Indium Gallium Selenide (CIGS) panels are installed.

Initially, the panels were connected in series to optimize energy production. Subsequently, to obtain a more accurate and fair comparison, the electrical

connections were disconnected, and data acquisition was performed on individual panels operating independently.

Figure 5.1 – Residential PV power plant of the International University of Rabat.

5.1.1 PV modules specifications

The single-crystalline panel, Uranus Panels rated at 250 W, presents a nominal power of 250 W under standard test conditions. The open-circuit voltage is 37.92 V, while the short-circuit current reaches 8.62 A. The maximum power point occurs at a voltage of 30.96 V and a current of 8.07 A, values that ensure stable operation and good compatibility with standard power conversion systems.

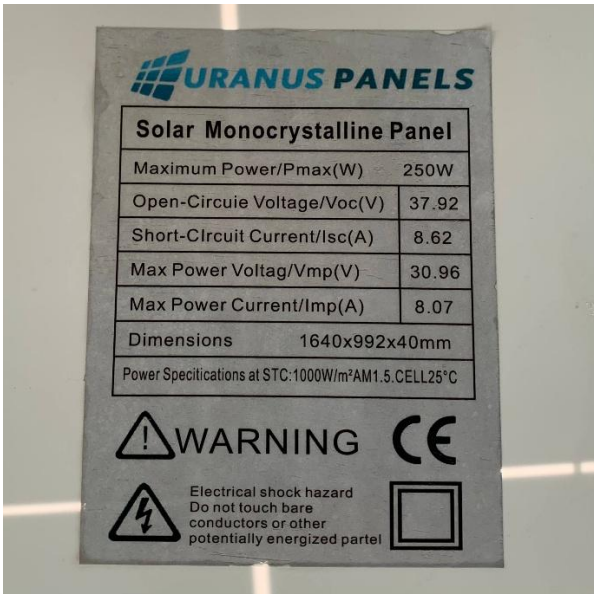

Figure 5.2 - Data sheet of the single-crystalline PV panel installed in the UIR plant.

The multi-crystalline panel manufactured by Amerisolar (model AS-6P30) presents a nominal power of 265 W, measured under standard test conditions (STC), corresponding to a solar irradiance of 1000 W/m², a cell temperature of 25 °C, and a solar spectrum of AM 1.5. From an electrical standpoint, the module operates with an open-circuit voltage of 38.3 V and a short-circuit current of 9.09 A. The maximum power point is located at a voltage of 30.9 V and a current of 8.58 A, values that ensure good compatibility with most commercially available inverters. A positive power tolerance of up to +3 % ensures that, under real operating conditions, the module can deliver a power output at least equal to its rated value.

Figure 5.3 - Data sheet of the multi-crystalline PV panel installed in the UIR plant.

The CIGS (Copper Indium Gallium Selenide) configuration consists of a string of two modules in series. The total string V_{oc} reaches $\approx 80\ V$ with a peak power output of $\approx 110 - 115\ W$, so the single photovoltaic module reaches a nominal power of approximately 55 W under standard test conditions. From an electrical perspective, the module is characterized by an open-circuit voltage ranging between 39 - 40 V, while the short-circuit current lies in the interval of 1.70 - 1.75 A. The maximum power point is reached at a voltage between 31.0 V and 33.0 V and a corresponding current of 1.55 - 1.65A.

These values reflect the intrinsic characteristics of thin-film CIGS technology, which typically exhibits lower current levels compared to crystalline silicon modules, but relatively high operating voltages. Such features make CIGS modules suitable for applications where performance under diffuse irradiance and partial shading conditions are required.

The amorphous silicon (a-Si) photovoltaic module included in the comparison is also an experimental device, with a rated power output of 79.8 W under standard test conditions. Electrically, the module operates with an open-circuit voltage of 20.8 V and a short-circuit current of 5.36 A calculated at 1.443 m^2. The maximum power point occurs at a voltage of 16.48 V and a current of 4.85 A.

Compared to crystalline silicon technologies, amorphous silicon modules are characterized by lower operating voltages and efficiencies, but they benefit from

good performance under low irradiance conditions and reduced sensitivity to high operating temperatures.

5.1.2 Power electronics and data acquisition

Electrical connections originating from the 4 photovoltaic modules, manufactured using different technologies, converge toward a common voltage sensor, which is used to measure the voltage at the terminals of the panels. This information is subsequently employed for the indirect estimation of the module operating temperature, exploiting the dependence of the open-circuit voltage on the cell temperature.

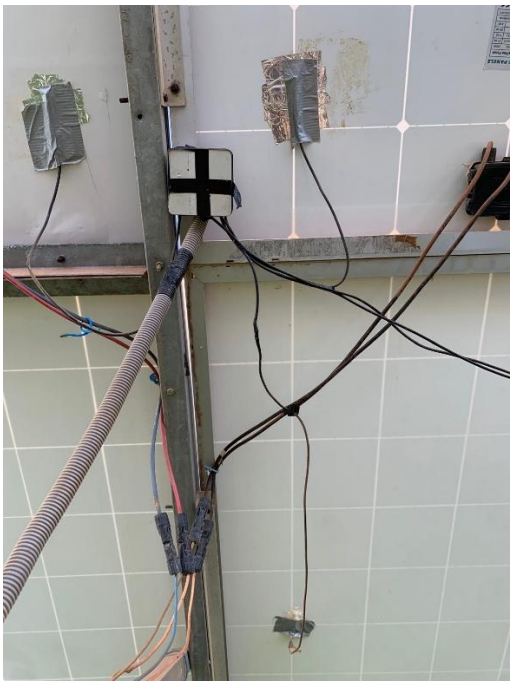

Figure 5.4 - Voltage sensor connected from the panels to the Arduino Nano.

Inside the laboratory, an Arduino Nano microcontroller is installed and is responsible for the acquisition and recording of electrical data. In particular, voltage values are measured using 4 experimental sensors, one for each panel, while current values are acquired through 4 industrial-grade sensors, characterized by higher stability and metrological reliability.

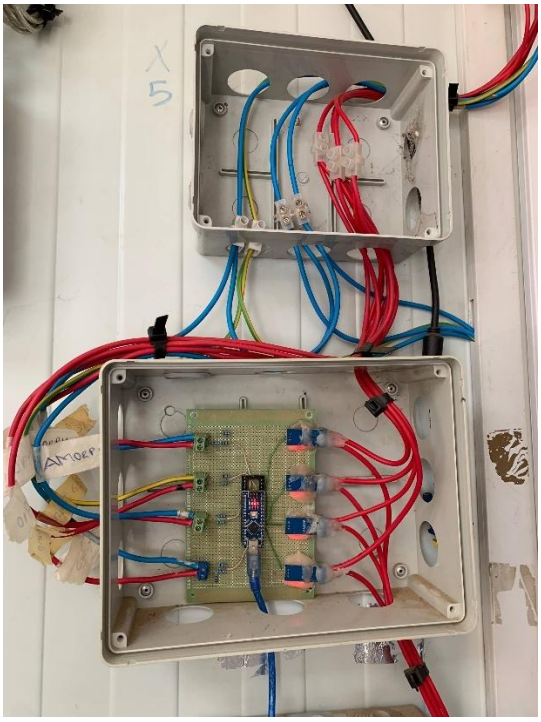

Figure 5.5 - Arduino Nano connection for measuring voltage and current.

Voltage and current data are acquired in real time and subsequently combined to enable continuous monitoring of the Maximum Power Point (MPP) of each photovoltaic module. This acquisition and analysis system effectively performs the function of an analogue MPPT, as it allows the identification of the operating point corresponding to maximum power without the use of complex digital algorithms or dedicated power converters.

In parallel with the experimental system, 4 commercial MPPT charge controllers supplied by Victron Energy are installed. The CIGS photovoltaic system uses a Victron SmartSolar 250/60 charge controller with two modules connected in series (2S). The single-crystalline and multi-crystalline photovoltaic modules are each operated as a single module and interfaced with a Victron BlueSolar 150/35 charge controller. The amorphous silicon module is also configured as a single module and connected to a Victron BlueSolar 150/35 controller.

Figure 5.6 - Different MPPT of the UIR laboratory.

These devices also operate in real time, but with a temporal resolution of 1 minute. They determine the maximum power point by combining information from photovoltaic panels and the energy storage system, which consists of lead-acid batteries.

5.1.3 Battery storage configuration

The energy storage system is composed of batteries OUTDO 150-12 (GEL) rechargeable sealed lead-acid batteries. Each unit provides $12\,V$ nominal voltage and a capacity of $150\,Ah$ (at the 10-hour discharge rate).

The laboratory operates two distinct energy storage configurations. A hybrid battery bank is used for the single-crystalline, multi-crystalline, and CIGS photovoltaic systems; it consists of four batteries arranged in a 2S2P topology, with two parallel strings, each composed of two batteries connected in series. This configuration results in a nominal system voltage of 24 V and a total storage capacity of 300 Ah, as expressed in the following expression, where $S_1$and S_2denote the two series branches.

$$V_{total} = 24\,V\,,\; C_{total} = 300\,Ah \tag{5.1}$$

In addition, a separate and independent storage circuit is dedicated to the amorphous silicon system and consists of a single battery operating at a nominal voltage of 12 V with a total capacity of 150 Ah, as reported in the following expression.

$$V_{total} = 12\,V\,,\; C_{total} = 150\,Ah \tag{5.2}$$

Figure 5.7 - Battery storage configuration of the UIR power plant.

Continuous day-by-day monitoring of the photovoltaic panel performance is, however, challenging. This limitation arises because the production system is not connected to an active load; as a result, the storage batteries remain almost constantly in a fully charged state. Under these conditions, the sensors are unable to accurately track the dynamic charging and discharging processes, nor to continuously represent the real-time evolution of power, voltage, and current with second-by-second resolution.

Finally, the system cannot be directly connected to a portion of the university electrical grid. This limitation is due to frequency compatibility and synchronization issues between the UIR electrical grid and the photovoltaic generation system, which prevents the direct injection of the produced energy without the implementation of additional interface and control devices.

5.2 Analysis of the real meteorological data

This section presents the results of the data collected from the UIR meteorological station.

Section 5.2.1 introduces the databases considered in the analysis, namely the real dataset used as a reference and the NASA satellite-based database.

Section 5.2.2 describes the adopted methodology and the MATLAB code implemented for data processing and analysis.

Section 5.2.3 reports the parameters of primary interest for photovoltaic technology, including global irradiance, temperature, and wind speed, as derived from both databases.

5.2.1 Introduction of the two compared datasets

The university weather station is located on the roof of the EEBLab laboratory and is composed of an anemometer to measure wind direction and wind speed, along with a sensor for air temperature and relative humidity. In addition, insolation data is recorded instead of continuous irradiance data due to measurement error considerations. Finally, a pyranometer is installed with the same orientation as the photovoltaic panels in order to acquire global solar irradiance data, i.e., the sum of direct and diffuse components. For this purpose, a standard research-grade thermopile pyranometer, such as the Kipp & Zonen CMP3, is utilized, providing reliable measurements with a typical expected daily accuracy of ±5% [48].

Figure 5.8 - UIR weather station.

The meteorological station collects data at a 10-second or one-minute temporal resolution and therefore provides wind speed, wind direction, air temperature, global irradiance, diffuse irradiance, reflected irradiance, relative humidity, precipitation rate, atmospheric pressure, dew point, and daily precipitation at this temporal resolution. To compare on-site measured meteorological data with satellite-derived data from databases, only the variables directly related to the energy conversion mechanisms of photovoltaic and wind power plants were selected, excluding meteorological parameters of a merely descriptive or maintenance-related nature.

Subsequently, the graphs of the mentioned parameters are analysed in detail for the year 2025, since the meteorological station has undergone maintenance only

recently and provides accurate data exclusively for the past year. Regarding satellite data, only a single dataset is considered in this section, as the objective of the analysis is not a relative comparison among different satellite products, but rather the assessment of consistency between measured data and satellite data. The meteorological station is assumed as the reference, while the satellite dataset represents an alternative modelled source, selected among those most widely used and validated in literature.

The use of a single dataset makes it possible to maintain a clear and linear methodological framework, avoiding interpretative ambiguities associated with the simultaneous use of multiple products characterized by different assumptions and spatial or temporal resolutions. This choice is considered appropriate in the present context, as it allows the analysis to focus on the direct comparison between measured data and satellite data, explicitly acknowledging that no conclusions are intended regarding the relative accuracy of different datasets, as this aspect has already been addressed in Section 4.2.

Accordingly, the months of August and October were selected as representative of the most and least sunny seasons, considering the availability and reliability of the collected data, which temporally extend only up to this month. In particular, it was decided to perform a graphical analysis of a single representative day for each month, rather than computing monthly averages and plotting the resulting trends. This choice stems from the approximation error that would have propagated into subsequent calculations and from the accuracy of the recorded measured data, which are considered more complete and reliable for 1 August 2025 and 10 October 2025, days for which no anomalies were detected at the meteorological station and, consequently, no data gaps were present in the data files.

The satellite dataset selected for solar irradiance data is CERES SYN, while MERRA-2 is used for wind data. Both datasets are made available within the data viewer of the NASA POWER platform; therefore, from this point onward, the two datasets will be collectively referred to as “NASA”. The selected solar data used for the comparison are those referring to solar irradiance on a horizontal plane, as this is the quantity measured by the real UIR meteorological station. Furthermore, the NASA database was chosen because it provides, at least for global irradiance, the best performance in terms of data accuracy, reliability, and availability of the parameters required over the widest possible temporal range, extending up to the current year 2025.

5.2.2 Methodology

The files corresponding to the two-month period are downloaded from the NASA POWER Data Access Viewer interface.

A MATLAB program is then implemented to open these files and generate vectors for each required parameter, specifically:

- Air temperature at 2 m above ground level (T2M, °C).
- Global irradiance on a horizontal plane (ALLSKY_SFC_SW_DWN, All-Sky Surface Shortwave Downward Irradiance, Wh/m²).
- Diffuse irradiance on a horizontal plane (ALLSKY_SFC_SW_DIFF, All-Sky Surface Shortwave Diffuse Irradiance, Wh/m²).
- Wind speed at 10 m above ground level (W10S, m/s).

Graphical plots are then obtained for 1 August 2025 and 10 October 2025.

For a consistent comparison, it is necessary to plot the real data acquired by the meteorological station for the same days and with the same temporal resolution. This requires a preprocessing step on the real .csv data provided by the UIR university, since their temporal resolution is significantly higher, with data acquired every 10 seconds.

A second section of the MATLAB program reads the time stamps under consideration, aggregates the acquired data into hourly intervals over the 24-hour period, and then computes and outputs the hourly averages. This results in an ordered and essential dataset that is directly comparable with the hourly files downloaded from the NASA dataset.

5.2.3 Graphical results

1 AUGUST 2025

GLOBAL IRRADIANCE

This section presents the results obtained from the comparison of the datasets, starting with the global irradiance parameter. During the month of August in

Morocco, in the Rabat region, daylight lasts approximately 15 hours, from 05:00 to 19:00 (sunrise at 05:30 and sunset at 19:30 on 1 August).

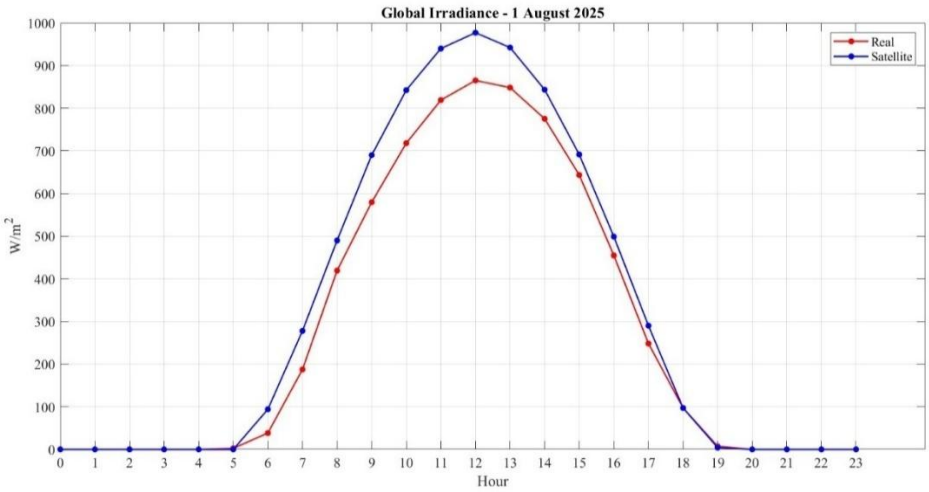

Figure 5.9 - Graphical comparison of real and satellite GHI data on the 1st August.

The observed trends of the two curves are similar and exhibit a bell-shaped profile, as expected for a solar irradiance plot. The non-zero values start at the same time for the two curves after shifting the real measured data one hour backward, since NASA data are stored according to the GMT (Greenwich Mean Time) convention, while in this month Morocco adopts the GMT+1 time zone. This adjustment results in curves that are not perfectly overlapping but are nevertheless comparable. The maximum value of satellite-derived irradiance reaches approximately 970 W/m², whereas the measured value peaks at around 860 W/m², resulting in a difference of about 100 W/m² during the central hours of the day. This discrepancy may be attributed to calibration errors of the university meteorological station, insufficient cleaning of the sensing surface, or data acquisition errors, discussed in detail in Section 4.3.

TEMPERATURE

The plot of temperature evolution is relevant for evaluating the thermal behaviour of the photovoltaic panel. For 1 August 2025, a comparable trend is observed in both datasets. The measured dataset starts at 21.4 °C and remains approximately constant until 06:00, while the NASA satellite dataset starts at a slightly higher temperature of about 22.3 °C and remains nearly constant until 05:00. Subsequently, the temperature increases in both cases, reaching a peak at around 13:00 of 27.5 °C for the satellite curve and 28.5 °C for the real curve. During the

afternoon hours, both curves decrease, following a descending trend without returning to the early morning values, stabilizing instead at approximately 22 °C for the measured data and 23 °C for the satellite data.

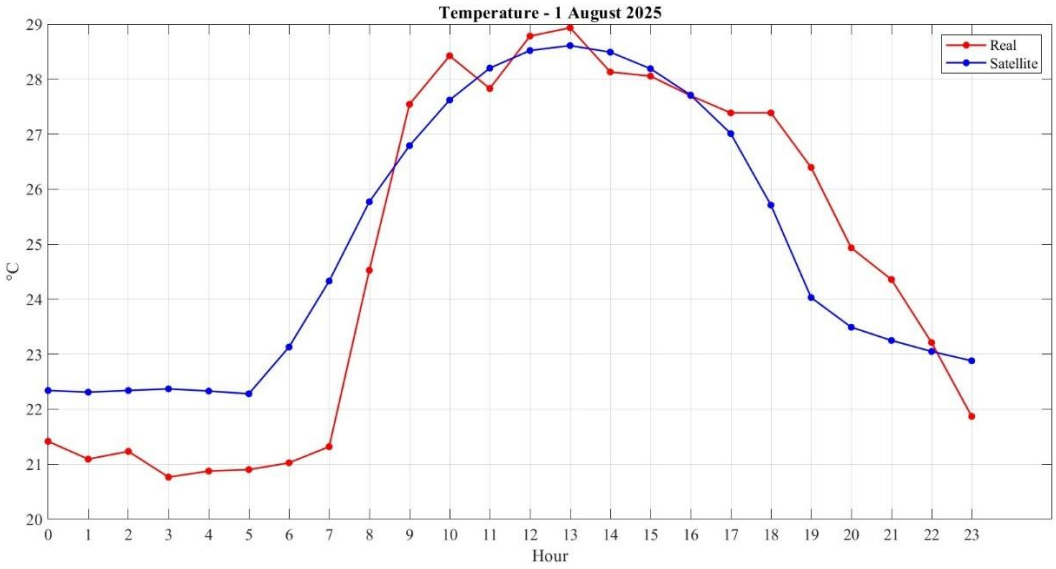

Figure 5.10 - Graphical comparison of temperature data on the 1st August.

Overall, the measured curve appears significantly less smooth than the satellite-derived one, as it is based on averages of near-instantaneous measurements from the meteorological station, which may include acquisition noise or temporary malfunctions. In contrast, satellite data are often interpolated or derived from images acquired every 1-3 hours, resulting in smoother profiles.

WIND SPEED

Finally, the wind speed trends measured at the UIR university and satellite-based of 1 August 2025 are presented. This parameter shows the largest discrepancy between satellite-derived data and real ones. Both datasets exhibit a similar general pattern, with lower values from 00:00 to approximately 07:00, followed by an increase reaching peak values around 14:00 - 15:00, and then a decrease toward the evening. However, the magnitude of the values differs significantly: the satellite-derived wind speed averages around 2.5 m/s, while the measured data exhibit an average of approximately 6 m/s. Peak wind speeds recorded by the UIR meteorological station exceed 9.7 m/s, whereas satellite-derived values do not exceed 4.5 m/s.

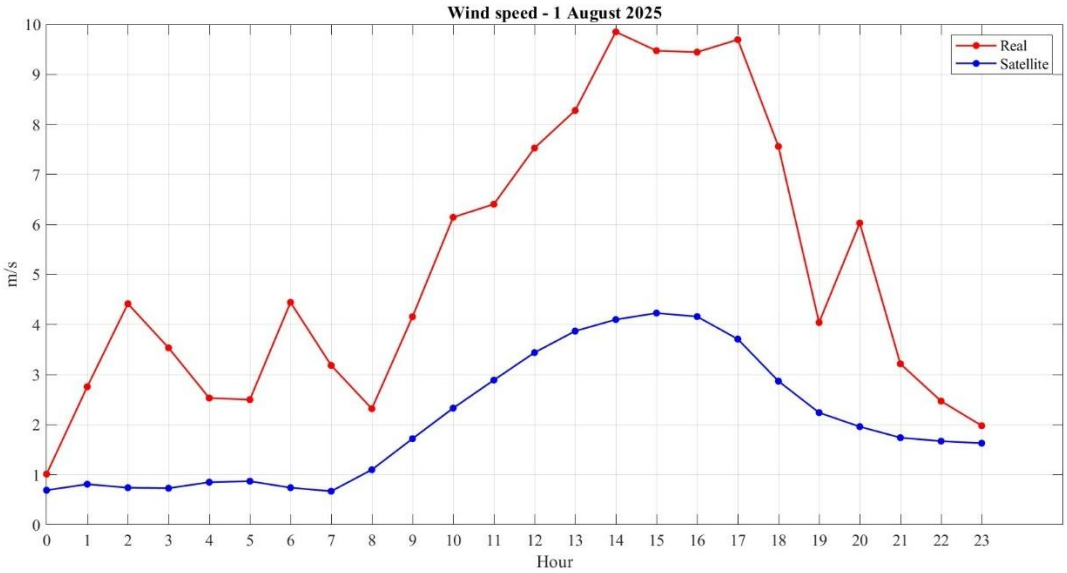

Figure 5.11 - Graphical comparison of wind speed data on the 1st August.

These differences can be reasonably justified by several factors. The ground-based profile consists of near-instantaneous measurements and is therefore influenced by temporary gusts or periods of reduced wind within the same hour, resulting in an irregular and jagged curve with abrupt variations. This behaviour is typical of wind data, which are inherently non-uniform throughout the day. Moreover, measurements are performed at different heights: although the meteorological station is installed on the laboratory roof and mounted on a support structure that adds approximately one additional meter, the effective measurement height reaches a maximum of about 5 m. Satellite wind data, on the other hand, are typically referenced to a height of 10 m, where measurement interferences are reduced and wind speeds may differ. Finally, satellite products rely on scatterometers or numerical models, which tend to smooth rapid variations and underestimate peak values.

10 OCTOBER 2025

GLOBAL IRRADIANCE

For the month of October, 10 October was selected for analysis. On this specific date in 2025 (up to 25 October), the time shift between the NASA database and the university dataset is one hour, corresponding to the GMT+1 time zone. Daylight lasts approximately 12 hours, fewer than in the summer month, starting at 07:00 and ending around 19:00.

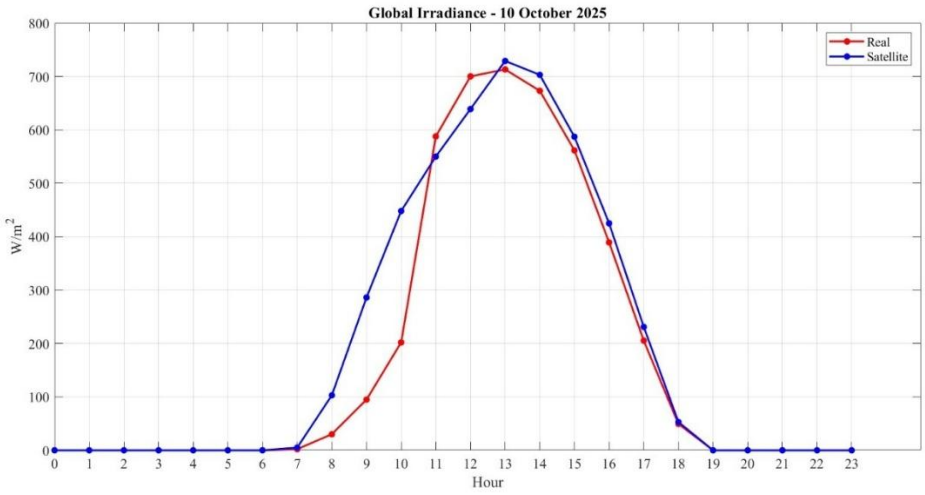

Figure 5.12 - Graphical comparison of real and satellite GHI data on the 10th October.

In this case as well, the two trends are comparable, although not overlapping, with measured values slightly lower than the satellite-derived ones, for the reasons discussed in the previous sections. The peak occurs between 12:00 and 13:00 and is approximately 730 W/m² for the satellite data and 710 W/m² for the measured data, resulting in a difference of about 20 W/m². This discrepancy is smaller than in August, although more pronounced deviations between the two curves are observed during the morning hours.

TEMPERATURE

For the temperature on 10 October 2025, the measured curve starts at approximately 19.2 °C and remains at this level for the first eight hours of the day. The satellite-derived curve, in contrast to the summer case, starts at lower values, around 18.2 °C. The temperature increase of the satellite curve follows a bell-shaped trend during the morning hours, reaching a peak of 24.1 °C at 14:00 and then decreasing during the evening to approximately 19.2 °C. The measured curve again exhibits a more irregular behaviour, increasing until around 12:00, when it reaches a peak of 23.8 °C, and then decreasing almost linearly until it returns to the same value as the initial temperature, approximately 19.2 °C.

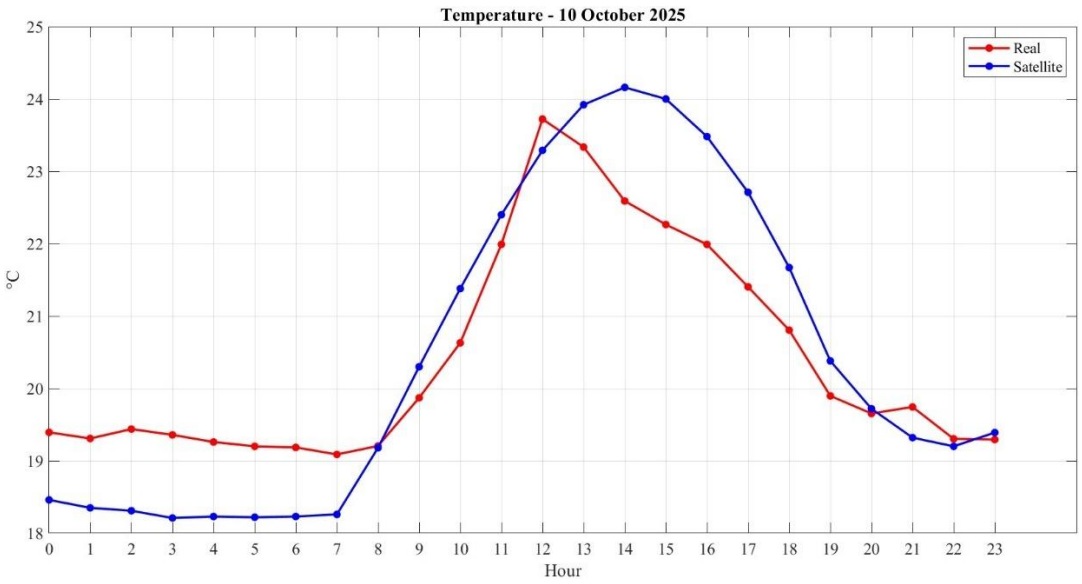

Figure 5.13 - Graphical comparison of temperature data on the 10th October.

WIND SPEED

Finally, the wind speed trend for the Technopolis area of Rabat on 10 October 2025 is analysed. The difference between the two curves is particularly evident between 12:00 and 19:00, with the satellite-derived curve reaching peak values of approximately 5.7 m/s, while the measured curve shows significantly higher peaks, up to about 14 m/s. As in the summer case, the measured profile is more irregular and dynamic, whereas the satellite-derived profile is smoother and generally underestimates wind speed values.

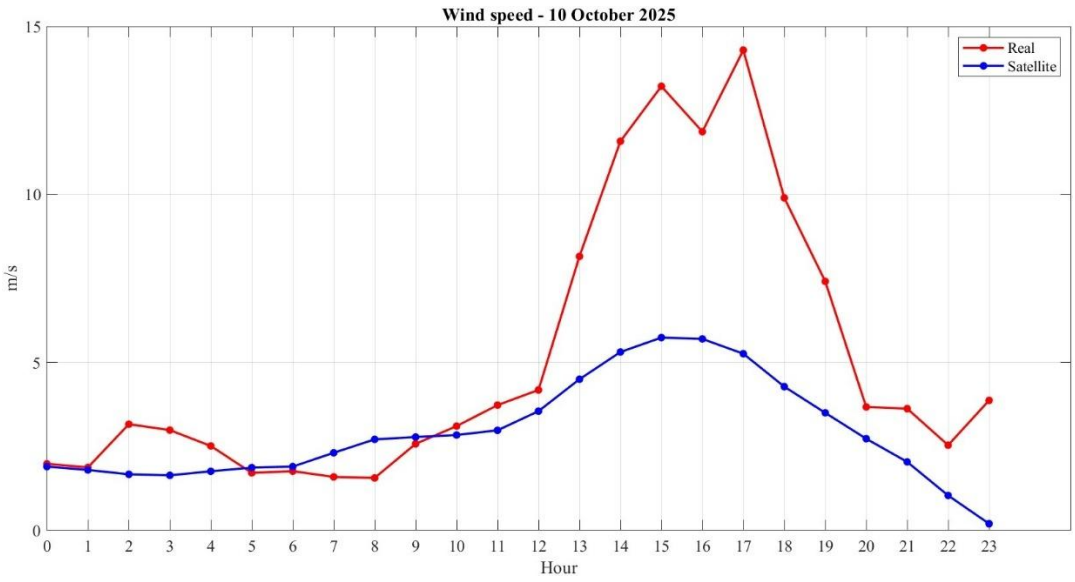

Figure 5.14 - Graphical comparison of wind speed data on the 10th October.

5.3 Error analysis between real and satellite datasets

In Section 5.2.3, a graphical result was obtained that relates the hourly data of the same day for the two different datasets, namely the measured (ground-based) and the satellite-derived data.

In Sections 5.3.2, 5.3.3 and 5.3.4, the differences between the two datasets are analysed from a quantitative perspective, by means of error metrics that are most relevant in the context of a photovoltaic system study. The selected error metrics are presented, as they are considered the most suitable for describing the differences between the real database and the NASA satellite database.

In Section 5.3.5, the results and the corresponding comments are presented, concluding whether the obtained values are acceptable or not.

5.3.1 Mean absolute error

In this case study, Mean Absolute Error (MAE) is used to quantify the average magnitude of the differences between the real data values took as a reference and satellite values.

It provides a direct measure of the typical error committed by a model, without allowing positive and negative deviations to cancel each other.

The general formulation is:

$$MAE = \frac{1}{N}\sum_{i=1}^{N}|x_{sat} - x_{real}| \quad 5.3$$

with:

- N: total number of observations, in this case $N = 24$, corresponding to the number of hours in a day.
- x_{sat}: satellite dataset value, in this case NASA dataset.
- x_{real}: real dataset value, in this case from UIR weather station.

It retains the same physical units as the variable under analysis, which facilitates interpretation. From a mathematical perspective, it corresponds to the L^1 norm of the error.

5.3.2 Mean bias error

The analysis begins by considering the systematic deviation, i.e., the extent to which the satellite data overestimate (positive MBE) or underestimate (negative MBE) the measured parameters with respect to the real data acquired by the UIR meteorological station, and therefore with respect to a local bias.

The general expression is:

$$MBE = \frac{1}{N}\sum_{i=1}^{N}(x_{sat} - x_{real}) \quad 5.4$$

with:

- N: total number of observations, in this case $N = 24$.
- x_{sat}: satellite dataset value.
- x_{real}: real dataset value.

This formulation is then applied to the specific cases of each parameter and for each analysed month.

Moreover, it is considered useful since it is able to identify, in general terms, whether one curve is higher than the other and therefore which of the two overestimates or underestimates the actual values of the parameters.

In the sum over the 24 hours, if the absolute error is not used, there is the possibility that this summation cancels out; however, in the case of the parameters considered,

namely global irradiance, temperature, and wind speed, this does not occur. Therefore, it is deemed effective to include the error in the subsequent results.

5.3.3 Root mean square error

In this Section, the Root Mean Square Error (RMSE) is analysed. This metric quantifies the average magnitude of the deviations between satellite-derived data and observed measurements.

The higher the RMSE, the greater the variability of the estimated data and the lower their reliability. RMSE is therefore used to assess whether the model produces consistent results or exhibits irregular errors.

The general formulation is:

$$RMSE = \sqrt{\frac{1}{N}\sum_{i=1}^{N}(x_{sat} - x_{real})^2} \quad 5.5$$

with:

- N: total number of observations, in this case $N = 24$.
- x_{sat}: satellite dataset value.
- x_{real}: real dataset value.

For the case under analysis, results are presented in Section 5.3.5, respectively for the summer month and for the autumn month.

5.3.4 Coefficient of determination

The R^2 error metric measures how well the satellite-derived data explain the variability of the observed data acquired by the meteorological station.

Its value ranges between 0 and 1: values close to 1 indicate a strong correlation and good predictive capability.

The general formulation is:

$$R^2 = 1 - \frac{\sum_{i=1}^{N}(x_{real} - x_{sat})^2}{\sum_{i=1}^{N}(x_{real} - \bar{x})^2} \quad 5.6$$

with:

- N: total number of observations, in this case $N = 24$.
- x_{real}: real dataset value.
- x_{sat}: satellite dataset value.
- $\bar{x}$: mean of real values.

This formula can be interpreted as follows:

- $R^2 = 1$: the model perfectly explains the observed data.
- $R^2 = 0$: the model provides no explanatory power and is equivalent to using the mean value.
- $R^2 < 0$: the model performs worse than the mean value (severe modeling error).

For the UIR case study, the results obtained are presented in Section 5.3.5.

5.3.5 Error analysis numerical results

In this Section, the numerical results of the error metrics considered most suitable for describing the real and satellite databases taken into account for the localization of the International University of Rabat are presented.

Separately for each different parameter, there is a summary of results for global irradiance on a horizontal plane, air temperature at 2 meters above ground level, and wind speed at 10 meters above ground level for the two selected days of the year, 1 August 2025 and 10 October 2025.

GLOBAL IRRADIANCE

Table 5.1 – Error analysis for global irradiance at UIR.

GLOBAL HORIZONTAL IRRADIANCE				
Day	**MAE** (W/m²)	**MBE** (W/m²)	**RMSE** (W/m²)	**R^2**
1 August 2025	41.1	40.7	61.5	0.996
10 October 2025	31.2	23.0	68.1	0.94

MEAN ABSOLUTE ERROR

The analysis of the Mean Absolute Error (MAE) provides a measure of the average magnitude of the errors in the satellite estimates, without considering their direction. Comparing the two selected days, a noticeable reduction in the absolute error is observed as the season transitions from summer to autumn.

For the day of 1 August 2025, the MAE reaches 41.12 W/m². It is crucial to observe that this value is almost identical to the Mean Bias Error MBE = 40.652 W/m². This proximity indicates that the error on this summer day is predominantly systematic: the satellite consistently overestimates the irradiance throughout the day, with very few periods of underestimation that would otherwise increase the MAE relative to the bias. This behaviour is typical of clear-sky days with high solar elevations, where calibration offsets or aerosol optical depth misinterpretations in the satellite algorithm translate directly into a constant positive bias [35].

In contrast, on 10 October 2025, the MAE decreases to 31.168 W/m², representing an improvement in the absolute accuracy of the satellite model of approximately 24% compared to the August case. This reduction can be attributed to the seasonal decrease in the maximum solar elevation angle, zenith angle effect and the lower absolute values of global irradiance reaching the surface. Since the MAE scales with the magnitude of the measured parameter, a decrease in available solar energy naturally tends to reduce the absolute value of the error in W/m² [49].

Furthermore, unlike the August case, the MAE for October 31.168 W/m² is noticeably larger than its corresponding MBE = 22.933 W/m². This divergence suggests that the error profile in October is less systematic and more variable; it implies the presence of alternating periods of overestimation and underestimation which partially cancel out in the bias calculation but accumulate in the absolute error metric. Nevertheless, a MAE of roughly 30 W/m² remains a robust result for daily hourly integration, confirming the reliability of the satellite dataset for autumnal energy estimation.

MEAN BIAS ERROR

For global irradiance, on 1 August 2025, a positive systematic deviation MBE = 40.652 W/m² is observed, indicating that the NASA database overestimates this parameter. The peak values of satellite and measured data reach approximately 980

W/m² and 870 W/m², respectively, with the latter being more plausible for non-ideal global irradiance, influenced by meteorological and physical factors.

As in the August case, for the day of 10 October 2025, a positive MBE = 22.933 W/m² is observed for global irradiance, indicating a slight overestimation of the satellite dataset with respect to the measured one. In this case, as also shown in the plots presented in the previous section, global irradiance values are even closer between the two datasets. This is particularly evident in the descending part of the bell-shaped curve, from 13:00 onward, when the MBE assumes values close to the order of tens of W/m².

The MBE remains positive, although larger, between 07:00 and 11:00, while a trend inversion is observed during the following two hours, in which the measured data exhibit higher values than the satellite-derived ones. This behaviour can be explained by temporal and spatial scale effects, meteorological factors, or operational characteristics of the ground-based station. Peak values remain comparable for both datasets, reaching approximately 710 W/m², which is consistent with typical global irradiance levels for the month of October in regions such as Rabat. The average MBE is fully acceptable, and the comparison can be considered solid and coherent.

One contributing factor is that satellite measurements represent averages over a larger spatial grid compared to the point measurement of the meteorological station, which introduces errors and leads to overestimation. A second reason is the satellite derivation approach: although accurate, satellite values are estimated through algorithms and recombination procedures rather than obtained via direct observation, which accounts for the presence of thin clouds, aerosols, or atmospheric particles.

Moreover, satellites observe reflected irradiance directed upward and infer surface irradiance through albedo models and angular distribution assumptions. If the observed surface is more reflective or uniformly illuminated, the satellite may assign a higher incoming irradiance value than the irradiance that is actually reaching the pyranometer. However, uncertainties also exist for ground-based instruments, such as imperfect calibration or maintenance, soiling (sensor dirt), thermal offsets, or non-optimal sensor alignment.

Given these considerations, the MBE value for global irradiance is acceptable, especially for daily data, as it is positive and moderate, consistent with values

reported in the literature. Satellite performance is therefore considered robust relative to the real measurements.

ROOT MEAN SQUARE ERROR

For global irradiance on 1 August 2025, the Root Mean Square Error is relatively high reaching RMSE = 61.485 W/m² but remains within acceptable error limits and represents a typical value for daily irradiance comparisons. Validation studies indeed show that, for days characterized by variable sky conditions, RMSE values may exceed 100 W/m².

The obtained error value is also consistent with the previously calculated MBE, and the discrepancies between the measured and satellite datasets can be justified by the same factors discussed in the previous paragraph, namely meteorological effects and spatial and temporal mismatches between the measurements.

Also, for the October day selected for the analysis, the Root Mean Square Error remains within acceptable values RMSE = 68.096 W/m² when compared to the daily variability of global horizontal irradiance (GHI), which is typically on the order of several hundreds of W/m².

In this case, the RMSE is higher than in the August case, contrary to the behaviour of the MBE, which was lower in October. This is due to the fact that, between 09:00 and 11:00, the satellite and measured curves deviate more significantly than on 1 August. While this behaviour is smoothed when computing the MBE through averaging, it is instead amplified in the RMSE due to the quadratic nature of the formulation.

COEFFICIENT OF DETERMINATION

As stated in the introduction, this value, being very close to 1, indicates that the satellite observation performs extremely well with respect to the ground-based measurement and that temporal variations are almost entirely captured.

By observing the solar irradiance trend, on 1 August 2025, $R^2 = 0.996$. A variation in the slope of the curve can be identified, following the same hourly steps in both datasets, increasing until around 12:00 and then decreasing thereafter, eventually reaching zero values and thus a null slope over the same time intervals. The two datasets can therefore be considered directly comparable.

Also, for 10 October 2025 the coefficient of determination exceeds 0.9, $R^2 = 0.941$, indicating that the two curves are comparable and that satellite data accurately reproduce the temporal variability of the measured data.

The plots show a clear increasing trend in both datasets from approximately 07:00 until 13:00, followed by a decreasing trend thereafter, with only minor differences in slope that are negligible over a 24-hour time horizon.

TEMPERATURE

Table 5.2 – Error analysis for temperature at UIR.

TEMPERATURE				
Day	**MAE** (°C)	**MBE** (°C)	**RMSE** (°C)	**R^2**
1 August 2025	1.1	0.3	1.3	0.86
10 October 2025	0.8	0.04	0.9	0.90

MEAN ABSOLUTE ERROR

For the temperature value on 1 August 2025, the MAE is recorded at 1.050 °C. This value, slightly exceeding unity, reflects the difficulty of the satellite model in perfectly resolving the intense surface heating typical of the peak summer period in Rabat. During August, local microclimatic effects and sharp diurnal temperature gradients are more pronounced, leading to a larger average discrepancy between the grid-averaged satellite data and the specific point measurement of the meteorological station.

Conversely, for 10 October 2025, the performance significantly improves, with the MAE dropping to 0.781 °C. This reduction of approximately 25% compared to the August case indicates a better alignment during the transition season. As solar forcing decreases and air temperatures become milder in autumn, the spatial variability of temperature fields tends to reduce, allowing the satellite algorithm to capture the local thermal dynamics with greater precision compared to the summer extremes.

Both values are within the acceptable range for energy applications. An MAE consistently close to or below 1 °C ensures that the simulation of temperature-dependent losses in photovoltaic modules remains accurate and reliable across different seasons.

MEAN BIAS ERROR

For temperature, on the 1 August 2025, a slight overestimation of the NASA satellite values relative to the real measurements from the meteorological station is also observed, MBE = 0.278 °C. From the previous Section's plots, peak temperatures are similar, reaching about 28.5 °C.

However, during the late afternoon hours (16:00 - 22:00), the MBE becomes negative, as the real measurements overestimate the values. This can be explained by imperfect maintenance of the meteorological instruments and residual heat accumulated in the sensor during the day, resulting in readings approximately one degree higher than the satellite values.

Considering the daily MBE, a bias of a few tenths of a degree is typical and not problematic in NWP/R models. Therefore, the temperature error is considered acceptable, and satellite data are robust relative to real measurements.

On 10 October 2025, MBE = 0.035 °C, with a daily average bias of only a few hundredths of a degree Celsius. Regarding the hourly behaviour of the deviation, it is negative and on the order of approximately 1 °C during the early hours of the day up to 07:00, when residual heat accumulation during the night or systematic errors in the measuring instruments may occur. Subsequently, the MBE becomes positive, indicating a slight overestimation of satellite values for most of the remaining hours of the day, with the exception of a few isolated peaks.

During the afternoon hours, the MBE increases, which can be explained by acquisition errors or by the analytical averaging applied to the real dataset, which may include data gaps and related limitations. Overall, the temperature MBE indicates good consistency and robustness between the two datasets.

ROOT MEAN SQUARE ERROR

The temperature for August day exhibits a relatively low RMSE, RMSE = 1.287 °C. If the early hours of the day are considered separately, this value would be

higher than the average RMSE of 1.287 °C, and the discrepancy between the two datasets would be more evident, since this metric penalizes larger errors. During the central hours of the day, approximately between 09:00 and 17:00, the RMSE decreases and then increases again, while remaining within acceptable limits.

The explanations for this behaviour are the same as those previously reported for the MBE. Considering the mean RMSE value for temperature, it can be noted that an error of approximately 1 °C is recurrent in the results of international studies, particularly in comparisons between satellite or reanalysis datasets and ground-based observations.

For 10 October, the temperature comparison between satellite-derived and measured data yields an RMSE lower than 1 °C, RMSE = 0.914 °C, indicating excellent agreement between the two datasets and therefore validating the satellite product with respect to the measurements recorded by the UIR university meteorological station.

COEFFICIENT OF DETERMINATION

On 1 August 2025, the value of the coefficient of determination for temperature is lower than that obtained for irradiance-related parameters, $R^2 = 0.856$, but it remains above 0.85, indicating that daily variability is still well captured. The increasing trend of both curves is observed over the same time intervals, particularly from the beginning of the day until approximately 10:00. The discrepancy increases during some subsequent hours, when the satellite curve continues to increase while the measured curve shows isolated decreases, and vice versa during the second part of the day.

Overall, considering the general behaviour of the curves, these discontinuities can be attributed to systematic and acquisition-related errors, which remain below 1 °C, or to differences in temporal resolution and approximations introduced by the averaging procedure. In validation studies of satellite reanalysis products such as MERRA-2, coefficients of determination for air temperature can reach values of approximately 0.99; however, lower values are still considered acceptable.

The value of R^2 for temperature is higher for 10 October 2025 than for 1 August 2025, reaching $R^2 = 0.895$. The observed trend increases until around 12:00 for the measured curve and until approximately 14:00 for the satellite-derived one, highlighting the main difference between the two datasets with respect to the

correlation calculation. From that point onward, both curves exhibit a decreasing trend.

This result is considered very good for temperature in satellite-versus-ground validation studies of meteorological datasets and is comparable with global validation results.

WIND SPEED

Table 5.3 – Error analysis for 10 meters wind speed at UIR.

WIND SPEED				
Day	**MAE** (m/s)	**MBE** (m/s)	**RMSE** (m/s)	**R^2**
1 August 2025	3.1	-3.1	3.5	0.84
10 October 2025	2.4	-2.2	3.5	0.78

MEAN ABSOLUTE ERROR

The analysis of the Mean Absolute Error MAE for wind speed reveals significantly larger discrepancies compared to the previously analysed parameters global irradiance and temperature.

This divergence is largely attributable to the source of the satellite data: while solar and thermal parameters were derived from the high-resolution NASA CERES-SYN1 algorithms, wind speed data are extracted from the NASA MERRA-2 reanalysis model. MERRA-2 operates on a coarser spatial grid (~50 km), which inherently struggles to capture local surface roughness and topographic acceleration effects that are detected by the ground station anemometer at UIR.

For the day of 1 August 2025, the MAE reaches 3.050 m/s. It is critically important to observe that this value is mathematically identical to the absolute value of the Mean Bias Error MBE = -3.050 m/s. This identity implies that the error on this day is entirely systematic: the MERRA-2 model consistently underestimates the wind speed at every hourly step, failing to reproduce the peak discrepancies caused by local thermal breezes or gusts. This behaviour highlights the "representation error" typical of reanalysis products, where a volume-averaged wind vector cannot fully

represent the kinetic energy measured at a specific point, especially in complex terrain.

On 10 October 2025, the MAE decreases to 2.400 m/s, marking an improvement in model performance of approximately 21% compared to the August case. Although the error remains substantial relative to the magnitude of the measured wind, the reduction indicates that the reanalysis model aligns better with the ground truth during the autumn season.

This behaviour is likely due to a shift from thermally driven local winds that are harder to model to more synoptic-scale weather patterns, easier to capture.

However, the persistence of a high MAE confirms that while NASA databases are excellent for solar resource assessment, the MERRA-2 wind product requires local calibration or "bias correction" before being used for precise wind energy yield calculations.

MEAN BIAS ERROR

For wind speed value on 1 August 2025, a negative MBE = -3.050 m/s is observed for the first time, with minimal differences in the early and late hours of the day when wind speeds are below 1 m/s for the satellite data and approximately 3 m/s for the real data. The MBE increases between 09:00 and 18:00, where the difference between the two datasets reaches 5.8 m/s at 14:00. This behaviour is observed over multiple days of the month, even though this work focuses on a single day, indicating a systematic underestimation of wind by the satellite dataset.

This error can be explained by the rapid variability of wind on very small spatial scales, as in this case study. Factors include terrain roughness, local obstacles of varying height affecting measurements differently, air mass transitions, sub-grid wind gradients, gusts, transient events, and, importantly, the very different temporal resolution of the two datasets.

Satellite data are already provided as hourly averages with their respective errors, whereas real measurements were collected at 10-second resolution and then averaged hourly. It should be noted that these acquisitions are not always regular, with missing data sometimes spanning several minutes, leading to different total counts per hourly average. Overall, this MBE value is consistent with the literature,

which highlights the difficulty of models in accurately estimating extreme wind values.

Also on the 10 October 2025 the systematic deviation is negative, MBE = -2.203 m/s, indicating that the satellite data underestimate wind speed values. In detail, the MBE trend oscillates between positive and negative values from the beginning of the day until approximately 12:00. However, these values remain lower than the average MBE, being on the order of about 1 m/s. From 12:00 onward, MBE values remain negative, confirming the underestimation of wind speed by the satellite dataset.

The difference between the two databases becomes significant during the central hours of the day up to 18:00, reaching very high MBE values, up to 10 m/s, before stabilizing at more acceptable levels. As previously observed, in the case of wind speed these results are acceptable and justifiable, since wind is a parameter characterized by very rapid variability, low spatial uniformity, and limited temporal coherence.

ROOT MEAN SQUARE ERROR

For wind speed data on 1 August 2025, the RMSE is relatively high RMSE = 3.478 m/s; however, it is interpreted considering the scientific literature. Numerous studies highlight that wind speed is one of the most challenging meteorological parameters to reproduce accurately, due to its high spatial and temporal variability and its strong dependence on local surface roughness, topography, and turbulence within the atmospheric boundary layer.

Satellite products and meteorological reanalysis provide spatially and temporally averaged estimates over grids with kilometre-scale resolution and fixed time intervals and therefore cannot resolve the microscale fluctuations captured by ground-based instruments. Consequently, RMSE values greater than 2 m/s and systematic biases are commonly observed, particularly over land and under moderate to strong wind conditions.

Validation studies of reanalysis products such as MERRA-2 report RMSE values that can reach or exceed 3 m/s in the presence of strong local heterogeneity, confirming that wind speed accuracy is intrinsically lower than that of other meteorological parameters. Therefore, the RMSE values obtained in this study can

be considered acceptable within the context of the known limitations of satellite and reanalysis data for near-surface wind speed estimation.

As in the previous cases, the error associated with wind speed is the highest among all the analysed parameters. For 10 October, RMSE = 3.547 m/s; however, this value can also be considered acceptable and consistent with the justifications and literature references already discussed.

COEFFICIENT OF DETERMINATION

For wind speed on 1 August 2025, the coefficient of correlation between the two curves is lower than that obtained for irradiance parameters, while still exceeding 0.8 but remaining below 0.85.

From the trends discussed in the previous section, the measured data exhibit a more irregular and fragmented profile, which explains why pointwise variability is not always accurately reproduced. Nevertheless, when considering the overall daily evolution, the value $R^2 = 0.837$ is considered acceptable.

In validations of satellite reanalysis products such as MERRA-2, coefficients of determination for wind speed in the range $0.81 \leq R^2 \leq 0.99$ are regarded as indicators of good correlation with in-situ measurements. Despite the presence of bias, temporal fluctuations are therefore well represented.

The R^2 value obtained for wind speed on 10 October 2025 is the lowest recorded in this analysis, R^2 = 0776, showing a slight degradation compared to the August correlation.

The measured data displays irregular behaviour during the early hours of the day, become more aligned with the satellite-derived trend during the central hours, and then return to a more irregular pattern around 16:00 and during the late hours of the day. These anomalies are localized and can be explained by approximations in the satellite-derived curve.

In the literature, R^2values in the range of 0.7 - 0.8 are commonly considered acceptable for wind speed, since this variable is strongly influenced by local effects, turbulence, and microscale variability that cannot be fully resolved by satellite or reanalysis products. Therefore, the obtained value is consistent with analogous

validation studies and reflects the well-known limitations in the representation of wind in gridded dataset.

Conclusions

The present thesis aims to evaluate the available databases for the characterisation of solar and wind resources. The validation of fundamental parameters, such as global irradiance and wind speed, is a crucial preliminary task for the planning and design of new renewable energy plants in this region. Indeed, Morocco and the wider Middle East and North Africa (MENA) area are considered pivotal for the technological and economic growth of the energy sector.

The geographical scope of the data acquisition encompasses the entire territory of Morocco. Datasets were selected based on superior geographical coverage, as well as high spatial and temporal resolution, while restricting the selection to open-access sources. The analysis of error metrics for the selected databases focused on the city of Rabat, which was identified as the most suitable location due to the concurrent presence of both energy sources and the availability of robust power distribution and transmission infrastructure.

The results obtained for solar irradiance datasets were excellent; for the year 2023, an overall error of 3% was recorded for both the PVGIS datasets ERA-5 and SARAH-3, while a 4.3% error was observed for the NASA Data Access Viewer dataset utilising the CERES-SYN1 model. These findings are highly significant for photovoltaic planning, as any error in the irradiance parameter propagates directly into the calculation of the potential energy yield. Furthermore, these results align with recent literature, which suggests that satellite-derived solar products have reached a high degree of maturity and reliability for the MENA region, often showing Mean Bias Errors (MBE) within a 5% threshold.

Conversely, the analysis of wind speed at a height of 10 metres yielded significant discrepancies. The PVGIS with ERA-5 and NASA with MERRA-2 datasets showed substantial errors of 20% and 25%, respectively. These results are attributable to the lack of ground-truth reference values and the limited availability of open-access databases. Moreover, wind resources are inherently more stochastic and less uniform than solar resources. Consequently, satellite-derived models alone, without the integration of in-situ observations, site-specific validation, and the application of corrective biases, appear insufficient for precise wind resource

assessment. This limitation is well-documented in international studies, which emphasise that global reanalysis products often struggle to capture local micro-scale effects and boundary layer dynamics without regional downscaling.

The findings were subsequently applied to a case study involving the International University of Rabat, utilising on-site measurements. Although these real-world data were limited to specific days rather than a full annual cycle, they provided a valuable basis for comparison.

In conclusion, if a single dataset must be chosen for the integrated planning of renewable energy plants in Morocco, ERA-5 is recommended. It offers optimal spatial resolution, combines reanalysis data rather than relying solely on modelling, provides extensive geographical coverage, and is open access. However, it must be specified that wind data require further processing and calibration against real meteorological stations before they can be reliably employed for engineering design.

References

[1] F. Spertino, ‘Solar photovoltaic systems’. 2023.

[2] F. Spertino and A. Abete, ‘Conversione fotovoltaica dell’energia’. 2001.

[3] N. Gupta, G. Alapatt, R. Podila, R. Singh, and K. F. Poole, ‘Prospects of Nanostructure-Based Solar Cells for Manufacturing Future Generations of Photovoltaic Modules’, *International Journal of Photoenergy*, vol. 2009, Nov. 2009, doi: 10.1155/2009/154059.

[4] S. Arya and P. Mahajan, ‘Solar Cell Modeling Parameters’, in *Solar Cells: Types and Applications*, S. Arya and P. Mahajan, Eds, Singapore: Springer Nature, 2023, pp. 197–210. doi: 10.1007/978-981-99-7333-0_7.

[5] R. Syahputra, ‘Modified Perturb and Observe Approach in MPPT for a Standalone Photovoltaic System’, *Journal of Electrical Technology UMY*, vol. 6, pp. 112–118, Dec. 2022, doi: 10.18196/jet.v6i2.18354.

[6] ‘A thorough review of PV performance, influencing factors, and mitigation strategies; advancements in solar PV systems’, in *Performance Enhancement and Control of Photovoltaic Systems*, Elsevier, 2024, pp. 13–57. doi: 10.1016/B978-0-443-13392-3.00002-5.

[7] ‘PV Module Temperature Sensor Selection According to IEC 61724-1’, Seven Sensor. Accessed: Mar. 05, 2026. [Online]. Available: https://www.sevensensor.com/pv-module-temperature-sensor-selection-according-to-iec-61724-1

[8] F. Spertino, ‘Generatori eolici per la connessione alla rete’. 2016.

[9] G. Bracco, ‘Wind and Ocean Energy Plants’. 2024.

[10] ‘Wind Energy Systems - Your Electrical Guide’. Accessed: Mar. 05, 2026. [Online]. Available: https://yourelectricalguide.com/2022/11/wind-energy-systems.html

[11] ‘Morocco’, *Wikipedia*. Mar. 05, 2026. Accessed: Mar. 05, 2026. [Online]. Available: https://en.wikipedia.org/w/index.php?title=Morocco&oldid=1341774049

[12] ‘Google Maps’, Google Maps. Accessed: Mar. 05, 2026. [Online]. Available: https://www.google.it/maps/place/Marocco/@31.8008346,-7.1513477,6z/data=!4m6!3m5!1s0xd0b88619651c58d:0xd9d39381c42cffc3!8m2!3d31.791702!4d-7.09262!16zL20vMDR3Z2g?entry=ttu&g_ep=EgoyMDI2MDMwMi4wIKXMDSoASAFQAw%3D%3D

[13] ‘Global Solar Atlas’. Accessed: Mar. 05, 2026. [Online]. Available: https://globalsolaratlas.info/map?c=11.523088,8.173828,3

[14] ‘Atlas de la Ressource Solaire au Maroc’. Accessed: Mar. 05, 2026. [Online]. Available: https://solaratlas.masen.ma/map?c=28.574874:-9.052734:5&s=33.452068:-12.612305

[15] Y. E. khchine, ‘Wind energy potential assessment for electricity and hydrogen production in Morocco’s southern regions’, *Energy Nexus*, vol. 19, p. 100474, Sep. 2025, doi: 10.1016/j.nexus.2025.100474.

[16] ‘Global Wind Atlas’. Accessed: Mar. 05, 2026. [Online]. Available: https://globalwindatlas.info

[17] ‘Xlinks Morocco–UK Power Project’, *Wikipedia*. Dec. 06, 2025. Accessed: Mar. 05, 2026. [Online]. Available: https://en.wikipedia.org/w/index.php?title=Xlinks_Morocco%E2%80%93UK_Power_Project&oldid=1326035529

[18] A. Hajou, Y. El Mghouchi, and M. Chaoui, ‘A new solar-wind complementarity index: An application to the climate of Morocco’, *Renewable Energy*, vol. 227, p. 120490, Jun. 2024, doi: 10.1016/j.renene.2024.120490.

[19] ‘Open Infrastructure Map’. Accessed: Mar. 05, 2026. [Online]. Available: https://openinframap.org/stats/area/Morocco

[20] ‘global-power-plants: global-power-plants: 5 rows where country_long = “Morocco” and primary_fuel = “Solar” sorted by gppd_idnr’. Accessed: Mar. 05, 2026. [Online]. Available: https://datasette.io/global-power-plants/global-power-plants?_sort=gppd_idnr&_facet=year_of_capacity_data&_facet_size=max&country_long__exact=Morocco&primary_fuel__exact=Solar#g.mark=bar&g.x_column=name&g.x_type=ordinal&g.y_column=primary_fuel&g.y_type=quantitative&g.size_column=rowid

[21] ‘global-power-plants: global-power-plants: 11 rows where country_long = “Morocco” and primary_fuel = “Wind” sorted by gppd_idnr’. Accessed: Mar. 05, 2026. [Online]. Available: https://datasette.io/global-power-plants/global-power-plants?_sort=gppd_idnr&_facet=year_of_capacity_data&_facet_size=max&country_long__exact=Morocco&primary_fuel__exact=Wind

[22] ‘Global Power Plant Database - Datasets’. Accessed: Mar. 05, 2026. [Online]. Available: https://datasets.wri.org//datasets/global-power-plant-database

[23] R. Peters, J. Berlekamp, K. Tockner, and C. Zarfl, ‘RePP Africa – a georeferenced and curated database on existing and proposed wind, solar, and hydropower plants’, *Sci Data*, vol. 10, no. 1, p. 16, Jan. 2023, doi: 10.1038/s41597-022-01922-1.

[24] ‘Open Infrastructure Map’. Accessed: Mar. 05, 2026. [Online]. Available: https://openinframap.org/stats/area/Morocco/plants

[25] ‘Open Infrastructure Map’. Accessed: Mar. 05, 2026. [Online]. Available: https://openinframap.org/stats/area/Morocco/plants

[26] ‘Open Infrastructure Map’. Accessed: Mar. 05, 2026. [Online]. Available: https://openinframap.org

[27] ‘Moroccan Agency for Solar Energy “MASEN” (Law 57.09) – Policies’, IEA. Accessed: Mar. 05, 2026. [Online]. Available: https://www.iea.org/policies/5521-moroccan-agency-for-solar-energy-masen-law-5709

[28] International Energy Agency, *Energy Policies Beyond IEA Countries: Morocco 2014*. in Energy Policies Beyond IEA Countries. OECD, 2014. doi: 10.1787/9789264211483-en.

[29] O. B. G. Admin, ‘Legal regulations governing the Moroccan power sector evolve alongside targets - Africa 2019 - Oxford Business Group’. Accessed: Mar. 05, 2026. [Online]. Available: https://oxfordbusinessgroup.com/reports/morocco/2019-report/economy/renewed-ambition-regulations-governing-the-power-sector-have-evolved-alongside-ambitious-energy-targets

[30] K. Sakhraoui, R. Agadi, C. Von Hirschhausen, and G. S. Ege, ‘Energy policy in morocco: Analysis of the national energy strategy’s impact on sustainable energy supply and transformation’, *Next Research*, vol. 1, no. 2, p. 100072, Dec. 2024, doi: 10.1016/j.nexres.2024.100072.

[31] ‘Energy policy of Morocco’, *Wikipedia*. Jan. 26, 2026. Accessed: Mar. 05, 2026. [Online]. Available: https://en.wikipedia.org/w/index.php?title=Energy_policy_of_Morocco&oldid=1334930703

[32] H. El Hafdaoui, A. Khallaayoun, and S. Al-Majeed, ‘Renewable energies in Morocco: A comprehensive review and analysis of current status, policy framework, and prospective potential’, *Energy Conversion and Management: X*, vol. 26, p. 100967, Apr. 2025, doi: 10.1016/j.ecmx.2025.100967.

[33] M. Daoudi, ‘Education in renewable energies: A key factor of Morocco’s 2030 energy transition project. Exploring the impact on SDGs and future perspectives’, *Social Sciences & Humanities Open*, vol. 9, p. 100833, Jan. 2024, doi: 10.1016/j.ssaho.2024.100833.

[34] H. El Hafdaoui, A. Khallaayoun, and K. Ouazzani, ‘Long-term low carbon strategy of Morocco: A review of future scenarios and energy measures’, *Results in Engineering*, vol. 21, p. 101724, Mar. 2024, doi: 10.1016/j.rineng.2023.101724.

[35] C. A. Gueymard, ‘A review of validation methodologies and statistical performance indicators for modeled solar radiation data: Towards a better bankability of solar projects’, *Renewable and Sustainable Energy Reviews*, vol. 39, pp. 1024–1034, Nov. 2014, doi: 10.1016/j.rser.2014.07.117.

[36] M. Ahmad and M. Zeeshan, ‘Validation of weather reanalysis datasets and geospatial and techno-economic viability and potential assessment of concentrated solar power plants’, *Energy Conversion and Management*, vol. 256, p. 115366, Mar. 2022, doi: 10.1016/j.enconman.2022.115366.

[37] K. Gruber, P. Regner, S. Wehrle, M. Zeyringer, and J. Schmidt, 'Towards global validation of wind power simulations: A multi-country assessment of wind power simulation from MERRA-2 and ERA-5 reanalyses bias-corrected with the global wind atlas', *Energy*, vol. 238, p. 121520, Jan. 2022, doi: 10.1016/j.energy.2021.121520.

[38] G. Gualtieri, 'Analysing the uncertainties of reanalysis data used for wind resource assessment: A critical review', *Renewable and Sustainable Energy Reviews*, vol. 167, p. 112741, Oct. 2022, doi: 10.1016/j.rser.2022.112741.

[39] 'JRC Photovoltaic Geographical Information System (PVGIS) - European Commission'. Accessed: Mar. 05, 2026. [Online]. Available: https://re.jrc.ec.europa.eu/pvg_tools/en/

[40] 'NASA POWER | Data Access Viewer (DAV)'. Accessed: Mar. 05, 2026. [Online]. Available: https://power.larc.nasa.gov/data-access-viewer/

[41] 'The ERA5 global reanalysis - Hersbach - 2020 - Quarterly Journal of the Royal Meteorological Society - Wiley Online Library'. Accessed: Mar. 05, 2026. [Online]. Available: https://rmets.onlinelibrary.wiley.com/doi/10.1002/qj.3803

[42] 'SARAH-3 – satellite-based climate data records of surface solar radiation', ResearchGate. Accessed: Mar. 05, 2026. [Online]. Available: https://www.researchgate.net/publication/379938343_SARAH-3_-_satellite-based_climate_data_records_of_surface_solar_radiation

[43] R. Urraca, T. Huld, A. Gracia-Amillo, F. J. Martinez-de-Pison, F. Kaspar, and A. Sanz-Garcia, 'Evaluation of global horizontal irradiance estimates from ERA5 and COSMO-REA6 reanalyses using ground and satellite-based data', *Solar Energy*, vol. 164, pp. 339–354, Apr. 2018, doi: 10.1016/j.solener.2018.02.059.

[44] J. Olauson, 'ERA5: The new champion of wind power modelling?', *Renewable Energy*, vol. 126, pp. 322–331, Oct. 2018, doi: 10.1016/j.renene.2018.03.056.

[45] J. Ramon, L. Lledó, V. Torralba, A. Soret, and F. J. Doblas-Reyes, 'What global reanalysis best represents near-surface winds?', *Quarterly Journal of the Royal Meteorological Society*, vol. 145, no. 724, pp. 3236–3251, 2019, doi: 10.1002/qj.3616.

[46] I. Staffell and S. Pfenninger, 'Using bias-corrected reanalysis to simulate current and future wind power output', *Energy*, vol. 114, pp. 1224–1239, Nov. 2016, doi: 10.1016/j.energy.2016.08.068.

[47] G. Achenza, 'Sviluppo di un simulatore probabilistico dell'irradianza solare per la previsione fotovoltaica', Politecnico di Torino, 2025.

[48] 'CMP3 spectrally flat Class C pyranometer - Kipp & Zonen'. Accessed: Mar. 06, 2026. [Online]. Available: https://www.kippzonen.com/Product/11/CMP3-Pyranometer

[49] 'Best Practices Handbook for the Collection and Use of Solar Resource Data for Solar Energy Applications: Third Edition', ResearchGate. Accessed: Mar. 06, 2026. [Online]. Available: https://www.researchgate.net/publication/351006206_Best_Practices_Handbook_for_the_Collection_and_Use_of_Solar_Resource_Data_for_Solar_Energy_Applications_Third_Edition